Formation and Evolution of Hypernova Progenitors in Massive Binary Systems

by

John Alex Becker

Submitted to the Department of Physics
in partial fulfillment of the requirements for the degree of

Doctor of Philosophy

at the

MASSACHUSETTS INSTITUTE OF TECHNOLOGY

June 2004

Author ....
Department of Physics
May 7 2004

Certified by ....
Paul C. Joss
Professor of Physics
Thesis Supervisor

Accepted by ....
Thomas J. Greytak
Associate Department Head for Education

Formation and Evolution of Hypernova Progenitors in Massive Binary Systems

by

John Alex Becker

Submitted to the Department of Physics
on May 7 2004, in partial fulfillment of the
requirements for the degree of
Doctor of Philosophy

Abstract

The massive stellar progenitor of a hypernova explosion and an associated gamma-ray burst must satisfy two primary constraints: (1) the outer layers of the stellar core must possess sufficient angular momentum to form a centrifugally supported torus about the collapsed central object (a Kerr black hole); and, (2) the envelope of the star must not be excessively massive or distended, so that the energetic, ultrarelativistic outflow generated by the central engine in the core of the star does not risk being smothered before it can escape from the star and expand outward to produce a gamma-ray burst. Physical processes which occur during the evolution of an isolated massive star will tend to diminish its initial angular momentum content, rendering it difficult for such a star to become a hypernova progenitor since its core will likely no longer spin rapidly enough to support a torus about its collapsed core. However, a substantial fraction of massive stars are members of binary systems. Tidal locking, mass transfer, or stellar merger in an evolved massive binary system could possibly lead to the transfer of orbital angular momentum to the core of one of the stars (or to the core of a merged star, if a common envelope develops), of sufficient magnitude to produce the core of a successful hypernova progenitor (constraint 1). Further interaction between the stars or their compact remnants could lead to the loss of the hydrogen and possibly helium envelopes of one of the stars (constraint 2).

We have developed a new one-dimensional stellar evolution code that includes the effects of rotation on equilibrium stellar structure, and calculates the transport of angular momentum through the stellar interior due to convection, dynamical and secular shear instabilities, and gravity (buoyancy) waves. We have used this code to calculate a variety of evolutionary sequences involving the transfer of mass from one component of the binary system to the other. We have also calculated an evolutionary sequence ending in the merger of one component of the system with the core of the other, induced by a prior common-envelope phase.

We find that over a wide range of initial binary system parameters, the initially less massive component of the system can accrete a substantial amount of mass and angular momentum from the initially more massive component. The accreted angular momentum is efficiently transported inward from the surface of the accreting star toward its core by a combination of convection and dynamical and secular shear instabilities. If accretion commences while the accretor is still on the main sequence, we find that the inward-progressing wave of angular momentum can penetrate the core of the mass-gaining star, contributing to its store of rotational angular momentum without the need for gravity wave transport of angular momentum across the core-envelope interface. These stars end their evolution (just prior to core carbon ignition) as red supergiants, with cores endowed with sufficient angular momentum to give rise to a hypernova explosion. We also find that a subsequent common-envelope phase with the compact remnant of the primary might result in the ejection of the accretor's red-giant envelope, leaving either a bare helium or carbon-oxygen star. Such a star would be expected to explode in a Type Ib or Ic supernova/hypernova.

Accretors which begin to receive mass later, while they are undergoing early post main sequence evolution, also develop rapidly rotating envelopes, but require the action of gravity wave angular momentum transport in order to share the angular momentum acquired at their surfaces with the bulk of their more compact cores. As a result, these stars reach core collapse with more slowly rotating cores and more massive and tightly bound envelopes. We find that cores which redistribute their angular momenta after carbon ignition to come into solid body rotation (rotational angular velocity Ω = constant) just prior to core collapse have the most favorable rotational profiles for generating hypernova events that emit observable gamma-ray bursts.

We also find that our stellar merger model ends its evolution with a large reservoir of angular momentum in the layers exterior to the carbon oxygen core. With redistribution to $\Omega = \text{constant}$, we expect this core as well to be a viable gamma-ray burst progenitor.

Thesis Supervisor: Paul C. Joss
Title: Professor of Physics

Acknowledgments

First and foremost, I would like to thank my thesis advisor, Paul Joss, for his invaluable support and guidance during the course of this project. Without his many physical insights and, equally importantly, continual encouragement at crucial times, this work would not have been possible. I have benefitted immensely from the many hours we have spent in scientific discussions over the years, on topics ranging from theoretical stellar structure to geophysical fluid dynamics.

I would also like to thank the members of my thesis committee, Saul Rappaport and Alan Guth, for their encouragement and invaluable help in making this work possible. I would especially like to thank Philipp Podsiadlowski for the many occasions on which he has very generously provided scientific advice during the course of this work. His own work has been a continual source of inspiration for me.

Without the unwavering support and patience of Keith Johnson through the years, this work could not have been completed. The scientific and publishing collaborations I have pursued with him, on aspects of neuroimaging, have been an unending source of scientific and intellectual inspiration.

I would also like to express my deepest thanks to my mother and father, who have supported me unwaveringly in all my activities, from my earliest days to the present. They instilled in me a love of pursuits both musical and scientific, for which I will be forever grateful.

I would especially like to thank Janann Ali for her constant support, patience and companionship. I have been able to count on her unhesitatingly during times both thick and thin (and her fantastic cheesecakes helped alot, too). Thanks, also, to the racquetball gang: Jim Panico, Bruce Terry, Mohammed Meho, and the volleyball crew: Ellen, Jan, Jochen, Tanya, and Brian. And I must close with belated thanks to members of the Caltech fantastic-four: Will, Tom, and Steve.

Contents

List of Figures

List of Tables

Chapter 1

Introduction

1.1 Gamma-ray bursts in the universe

Gamma-ray bursts were discovered serendipitously in the late 1960's, by a satellite system originally developed to monitor compliance with the Nuclear Test Ban Treaty of 1963. Four Vela satellites, placed at roughly equal intervals along a circular orbit about Earth, were designed to continuously monitor the sky for the high-energy gamma-ray signature of a clandestine nuclear explosion.[1] Flashes of high energy photons were indeed observed; however, it quickly became clear to the Vela system's operators that the bursts of gamma-rays their satellites were detecting did not originate in terrestrially-initiated nuclear explosions.

The Vela satellite findings were announced to the astronomical community in 1973 (Klebesadel et al. 1973), to be followed shortly thereafter by similar and confirmatory data from the Soviet Konus satellite system (Mazets et al. 1974). Sixteen "gamma-ray bursts" (GRBs) were reported in the former paper, all detected from July 1969 to July 1972. The observed bursts ranged in duration from 0.1 to $\sim 30\,\mathrm{s}$, and consisted of photons with energies of $0.2 - 1.5\,\mathrm{MeV}$, with several of the longer bursts displaying rapid and complex time variability (Fig. 1-1 displays a typical burst light curve from one of the Vela satellites). The directional data for the bursts (derived from arrival time delays between satellites) ruled out the Earth and Sun as sources, and no correlations were noted between bursts and optical supernovae observed during the same

---

[1] With an orbital radius placing them roughly a quarter of the way to the Moon, even the remnants of detonations behind this large body were in principle detectable by the Vela system.

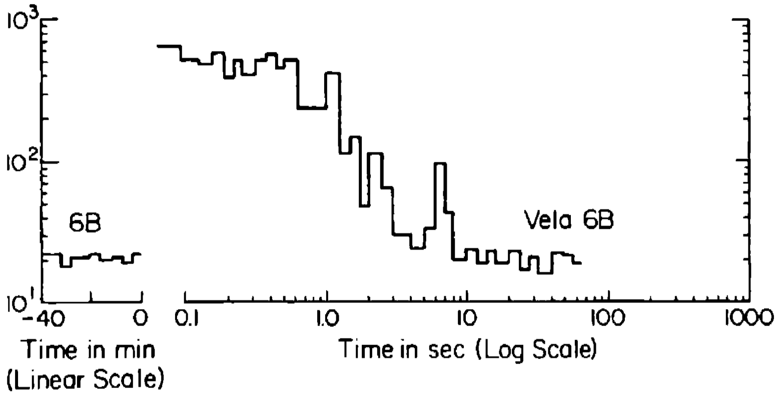

Figure 1-1: Count rate as a funtion of time for a gamma-ray burst of August 20, 1970 as recorded by one of three Vela satellites which detected this particular event (adapted from Klebesadel et al. 1973).

interval of time.

The Vela satellite data were only sufficient to place the bursts at a distance greater than ten satellite orbital diameters from Earth. This lack of observational constraints on the distance to the bursts, coupled with the intrinsically intriguing nature of the phenomenon, inspired some rather extreme flights of fancy on the part of theorists. Ruderman's contemporary summary, presented at the Texas conference on Relativistic Astrophysics in December 1974 (Ruderman 1975), cites several theories current in the literature of the time. Proposed burst mechanisms ranged from supernova shocks and neutron star formation, to stellar flares (from nondegenerate stars as well as from white dwarfs and neutron stars), accretion onto compact objects, and more exotically, antimatter accretion, relativistic dust, and white holes.[2] The theoretical landscape was still rather cluttered some 14 years later, as reviewed by Liang (1989).

Theoretical progress was slow during this period, not as the result of the imaginative shortcomings of theorists, but rather due to a lack of observational data, particularly data from less energetic wavebands. Data gathering was rendered particularly difficult by the short (typically less than 100 s) duration of the bursts, and the consequent lack of accurate coordinates for use in followup observations. Theoretical models for the bursts differed in their assumptions regarding the bursters' distances

---

[2] It has been noted that early in the development of the subject the number of theories exceeded the total number of bursts observed up to that point (Nemiroff 1994).

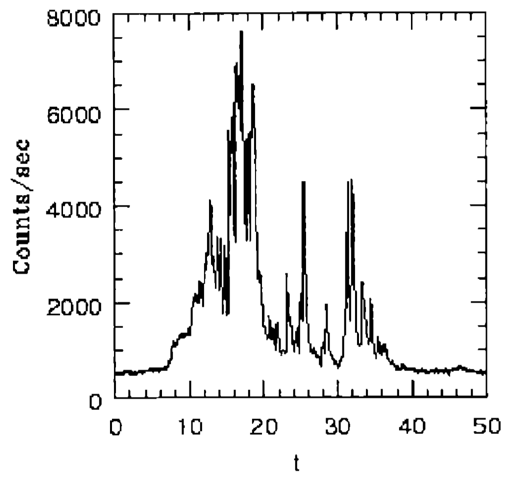

Figure 1-2: A typical gamma-ray burst count rate versus time curve as measured by the BATSE satellite, from Fishman & Meegan (1995).

from Earth. Galactic models assumed the bursters were located within the Galactic disc (at hundreds of parsecs to several kiloparsecs), in the Galactic halo (tens of kiloparsecs), or, at the smallest distance scales, near or even within the Solar system. At the other extreme were the cosmological models, which proposed that the bursts were located in other galaxies at gigaparsec distances.

A breakthrough of the observational impasse occurred in 1991 with the launch of the Compton Gamma Ray Observatory (CGRO) and its all-sky survey instrument, the Burst and Transient Experiment (BATSE) (Fishman & Meegan 1995). BATSE recorded over 2700 bursts, dramatically demonstrating that they were isotropically distributed across the sky (see Fig. 1-3). In the BATSE data no preferential clustering was evident near the Galactic center or Galactic disk, which would have been expected for a Galactic population of bursters. In conjunction with another trend evident in the observations, the distribution of burst number versus intensity (a measure of the homogeneity of burst distribution in Euclidean space, the flatness of which ruled out sources within the Galaxy), this result propelled the cosmological scenarios for gamma-ray bursts into frontrunner status.

Nonetheless, debates still ensued, with perhaps the most notable taking place

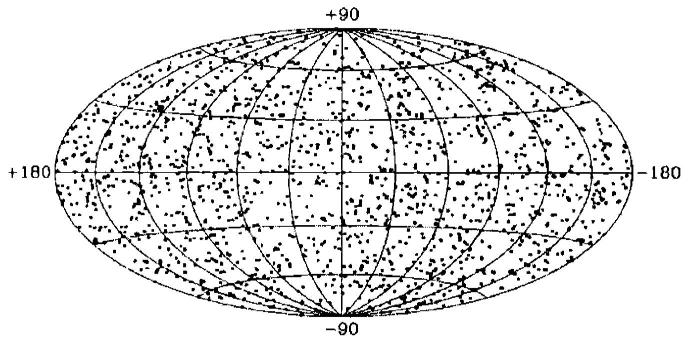

Figure 1-3: Distribution of gamma-ray bursts in the sky as derived from the BATSE catalogue (Paciesas et al. 1999).

in 1995 between D. Lamb and B. Paczyński (Nemiroff 1995; Lamb 1995; Paczyński 1995), staged to commemorate the 75th anniversary of the famous Shapley-Curtis debate on the extragalactic distance scale. Paczynski's position in this debate, that GRBs occur at cosmological distances, was subsequently demonstrated in dramatic fashion by observations conducted in 1997 by the Italian/Dutch Beppo-SAX satellite. Beppo-SAX successfully pinpointed several bursts precisely enough to allow, for the first time, the subsequent detection of their theoretically predicted afterglows in lower energy wavebands. High resolution X-ray images of the afterglow of GRB 970228 were obtained by Beppo-SAX in February of that year. In the following May the burst GRB 970528 was detected, the optical afterglow of which displayed absorption features characterized by $z = 0.835$, suggesting that it resided in a galaxy with the same redshift (Metzger et al. 1997). A subset of GRBs had at last been definitively placed at cosmological distances, a distance scale which has subsequently been repeatedly confirmed by further observations of burster host-galaxy redshifts.

The GRB population is bimodally distributed in burst duration (Kouveliotou et al. 1993), with approximately one-third of bursts (the so-called short bursts) having durations $t_\gamma < 2\,\mathrm{s}$ (where t_γ is the time interval over which the gamma-ray flux is significantly above zero; see Fig. 1-2), and the remaining two-thirds of bursts having $t_\gamma > 2\,\mathrm{s}$ (see figure Fig. 1-4). The latter constitute the population of "long, complex" bursts (complex referring to the variations on time scales from milliseconds to tens of seconds seen in the light curves of these bursts), a population for which many

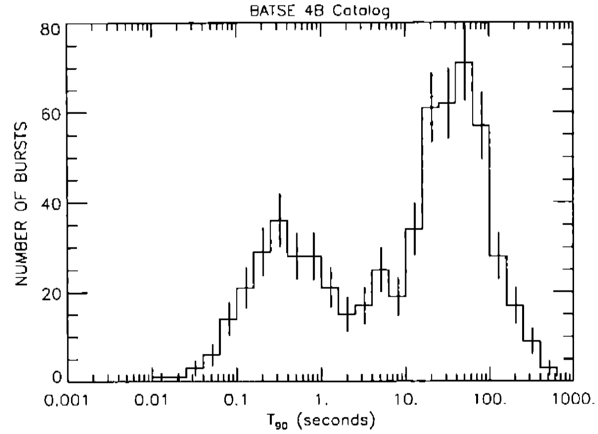

Figure 1-4: Distribution of burst durations from the BATSE catalogue of GRBs, taken from the BATSE home page.

afterglows have now been detected and host-galaxy redshifts determined. In this work we are only concerned with long, complex gamma-ray bursts, their central engines and possible progenitors. This is the population which has been definitively shown to occur at cosmological distances. We do not further consider short bursts, about which relatively little is known due to the lack of any detected afterglows to date.

Since their initial detection in 1997, many more burst afterglows have been located and studied in the X-ray, optical and radio wavebands. A particularly noteworthy event was the burst GRB 990123, the first for which both a prompt optical flash and a radio flare were observed (Akerlof et al. 1999; Kulkarni et al. 1999b). Based on its fluence and its redshift-determined distance ($z = 1.600$), GRB 990123 released a prodigious amount of energy, $\sim 3.4 \times 10^{54}(\Omega_j/4\pi)\,\mathrm{erg}$ (where Ω_j is the solid angle of the emission).[3] Theoretical models are hard-pressed to generate energies of this magnitude in a time interval so short.[4] The most efficient mechanisms known, those invoking magnetohydrodynamic interactions between a dense rotating torus and a rapidly spinning black hole to extract the immense rotational energy of the hole,[5] are barely sufficient.

---

[3] This is $\sim 1.9 M_\odot c^2$ (assuming isotropic emission), emitted on a time scale of seconds; the prompt optical flash associated with this burst had a maximum V-band magnitude of 8.9, equivalent to a peak luminosity $\sim 3.3 \times 10^{16} L_\odot$ (Kulkarni et al. 1999a).

[4] The photon luminosity of a typical burst is enormous, many orders of magnitude above the Eddington limit of a stellar mass object.

[5] For instance, the Blandford-Znajek mechanism; see the next section.

Observational data again came to the rescue. From the continued study of GRB afterglow spectra it soon became apparent that achromatic breaks in their power law decline could best be interpreted as due to a jetted or collimated emission geometry (for the particular case of GRB 990123 see Kulkarni et al. 1999a). Given a jet collimated into an opening angle θ_j, when the bulk Lorentz factor Γ of the material comprising the jet falls below θ_j^{-1}, a break in the spectrum is expected (Rhoads 1997). The break occurs when the relativistic beaming angle of the emission $1/\Gamma$ widens (as Γ decreases) to encompass and exceed the jet collimation angle θ_j. From this moment forward, from the observer's standpoint the "edges" of the beam come into view, and the outflow ceases to appear isotropic.

The reduced solid angle $\Omega_j \ll 4\pi$ implied by the achromatic breaks alleviates the energy crisis faced by GRB 990123 and other bursts; in fact, Frail et al. (2001) and others have shown that the observed anti-correlation of jet collimation angle θ_j with burst energy[6] implies a beaming-corrected standard burst energy of $\sim 10^{51}$ erg. This range of energies is comparable to the kinetic energies generated by supernova explosions, and is highly suggestive of a possible association between bursters and a subclass of supernovae.

These energetic constraints, in conjunction with the jetted structure of the relativistic outflow implied by observed achromatic breaks in the afterglow spectra, have important implications for theoretical models of GRBs. We discuss the current theoretical understanding of long GRBs in the following section.

1.2 Aspects of the physics of gamma-ray bursts

Current theoretical study of GRBs is primarily focused on two distinct aspects of the phenomenon: the origin and operation of the burster "central engine," which is responsible for generating the energetic and ultrarelativistic outflows that give rise to the burst over the appropriate time scales, and the physics of the generation of burst afterglows. Regarding the latter, the numerous afterglows which have been identified and measured since 1997 have facilitated the development of a now firmly-established theoretical model of their physics, the fireball shock scenario (see, e.g., the review by

---

[6] I.e. smaller θ_j are associated with larger isotropic burst energies.

Mészáros 2002, and references therein).

Attaining a comparable theoretical understanding of the central engines of gamma-ray bursters has proved more difficult, but advances on this front have also been steady over the past decade. Evidence of the association of bursters with star forming regions of their host galaxies (Paczyński 1998; Bloom et al. 1998a), the detection of the signature of a Type Ib or Ic hypernova[7] in the optical afterglows of several bursts, and, most suggestively, the spatial coincidence of the hypernova SN 1998bw with the burst GRB 980425, all implicate a supernova-like phenomenon as the underlying mechanism driving at least this subset of bursts.

1.2.1 Central engines and progenitors

A number of gamma-ray burst progenitor systems have been proposed in the literature. The majority involve a compact stellar remnant – a white dwarf, neutron star or BH – interacting either with another such remnant, or alternatively a normal (nondegenerate) star.

An early and popular cosmological model for the progenitors of GRBs at cosmological distances involves the coalescence of two neutron stars which spiral together as gravitational radiation extracts their orbital energy and angular momentum (Narayan et al. 1992; Paczýnski 1986). The resultant disk of debris, formed from the shredded remains of the two neutron stars and too massive to form a neutron star itself, redistributes its angular momentum via viscous processes and collapses into a rotating BH in a matter of milliseconds. The debris that remains has too much angular momentum to be immediately captured by the BH and instead forms a nuclear-matter-density torus surrounding it.

Other possible compact progenitor systems include neutron stars tidally disrupted by, and merging with, black holes (Lattimer & Schramm 1974; Janka et al. 1999); white dwarfs merging with black holes; and black holes spiraling into, and coalescing with, the cores of helium stars (Fryer & Woosley 1998; Zhang & Fryer 2001).

Compact binary systems have fallen out of favor as possible progenitor systems of long GRBs due to their inability to explain several observations regarding this

---

[7] Following Paczyński (1998) and Mazzali et al. (2003), we define a hypernova as a particularly energetic supernova, characterized by wide spectral lines indicating ejecta of unusually high kinetic energy.

population of bursters. A typical long GRB lasts for tens of seconds, whereas a compact binary system with a dynamical time on the order of milliseconds will tend to generate events on a much shorter time scale. Long GRBs also have a strong spatial association with star forming regions of their host galaxies. However, a binary neutron star system, which is expected to suffer two natal "kicks" over the course of its birth, will likely travel far beyond its birthplace in an actively star forming region before gravitational radiation has enough time to induce coalescence (Bloom et al. 1998b). These observational constraints (association with star forming regions, several correlated hypernovae/GRBs, and a supernova-like energy scale) point instead toward massive stars as the likely progenitors of the population of long gamma-ray bursts.

A black hole and an orbiting, dense disk or torus are two fundamental ingredients of massive star GRB progenitor models, as well as of all the scenarios outlined above. The energy to power a burst can in principle come from two sources in such a system: either the gravitational binding energy of the torus which surrounds the black hole, or the rotational energy of the black hole itself. The torus can provide an energy reservoir of up to 42% of its rest mass energy, assuming the associated black hole is maximally rotating; alternatively, a rotating black hole can provide up to 31% of its rotational energy, or 9% of its rest mass (Lee et al. 2000b), again assuming the hole is initially in a state of maximal rotation ($a = 1$; see below).

In the "collapsar" model of Woosley (1993), for example, the thermal energy produced by viscous dissipation in the accretion torus is carried away by neutrinos, which propagate from their source in the disk to external regions (preferentially along the rotation axis of the core), where they collide and annihilate to form an incipient fireball gas of electron-positron pairs and photons (i.e. $\nu\bar{\nu} \rightarrow e^+e^-$) (see, e.g., MacFadyen & Woosley 1999; Popham et al. 1999).

The dissipation of magnetic fields initially generated by fluid shearing motions in the differentially rotating torus offers an alternative means of tapping the latter's binding energy (Paczyński 1991; Narayan et al. 1992). Extremely strong magnetic fields, of order 10^{15} G, are necessary to transport this energy in the form of a magnetohydrodynamic (MHD) wind or "Poynting flow" on the time scales typical of long GRBs (Usov 1994; Thompson 1994).

The energy available from a rapidly rotating black hole can in principle be much larger than that associated with a centrifugally supported torus. Again, very strong magnetic fields of order 10^{15} G are required to extract this energy. If these fields are anchored in the torus and thread the black hole, some fraction of the latter's rotational energy can be extracted by the Blandford-Znajek (BZ) mechanism (Blandford & Znajek 1977; Lee et al. 2000a,b; van Putten & Ostriker 2001; van Putten 2001). The energy extractable from the black hole increases with increasingly rapid rotation. Parameterizing the rotation of the black hole by the dimensionless parameter $a = J_{BH}c/GM_{\rm BH}{}^2$ (where J_{BH} is the angular momentum of the hole and $M_{\rm BH}$ its mass), its rotational energy is given by $E_{{\rm BH},rot} = f(a)M_{\rm BH}c^2$, where $f(a) = 1 - [\frac{1}{2}[1 + \sqrt{1-a^2}]]^{1/2}$ rises rapidly from zero as a approaches unity. Therefore the black hole must be rotating at nearly its maximal rate in order for a significant amount energy to be derivable from its rotation (Lee et al. 2000b; van Putten 2001). In contrast to mechanisms driven by the gravitational binding energy of an accretion disk, energy extraction by the BZ mechanism does not require that material accrete from the torus into the black hole.

1.3 Massive stars as GRB progenitors

The stars which are the focus of the present work are assumed to have masses $M \gtrsim 10\,M_\odot$. We call a star which exceeds this limit "massive." A massive star will end its life in spectacular fashion, in one of the most energetic events in the known universe, a supernova explosion. The end result of a series of increasingly rapid nuclear burning stages, the iron core of the pre-supernova star is ultimately unable to provide pressure support against the unrelenting pull of gravity, and thus rapidly collapses to a neutron star (for $10 \lesssim M/M_\odot \lesssim 25$) or black hole (for $M/M_\odot \gtrsim 25$).[8] The concomitant release of a large quantity of gravitational binding energy drives off the stellar envelope and the outer layers of the stellar core and creates the display of a supernova explosion. Typical luminous and kinetic energies of supernova ejecta are in the range of $\sim 10^{51}$ erg.

The core of a rapidly rotating star of mass $M \gtrsim 25\,M_\odot$ might meet a somewhat

---

[8] See Heger et al. (2003) for a further discussion of the compact remnants expected from single stars in these mass ranges.

different fate than that described in the previous paragraph. If the core is endowed with sufficient angular momentum, the material near the axis of rotation will promptly collapse to form a central Kerr black hole during the supernova event, while material in the equatorial plane will initially be prevented from falling into the newly formed hole by a centrifugal barrier, and will instead coalesce into a massive, neutron-star density rotating torus surrounding the hole. The black hole/torus system so formed can generate the energetic outflows which ultimately result in a GRB by one of the mechanisms described in the previous section.

These theoretical considerations, however, beg the question of how the core of the progenitor star acquires and/or retains the angular momentum necessary to prevent its immediate and complete collapse.

1.3.1 Single stars and core angular momentum loss

At least two factors can work to decrease the angular momentum content of the core of a single star as it evolves:

- Even if a star begins its main sequence evolution in a state of rapid rotation, the continual loss of matter (and the angular momentum that it bears) from its surface by the action of a stellar wind will slow the rotation of its envelope, inducing a state of differential rotation between envelope and core;
- As the star evolves, its core contracts, the core's moment of inertia decreases, and, in the absence of sources or sinks of angular momentum, the core spins up, exacerbating the shear between it and the envelope of the star.

The growing differential rotation between the core and envelope of the star due to the action of these mechanisms will eventually induce turbulence in this region and thus angular momentum transport (see Chapter 3), which will act to reduce the level of differential rotation by transporting angular momentum down the gradient in angular velocity (i.e. from regions of high angular velocity to regions with lower angular velocity). The core of a single star will thus tend to continually lose angular momentum. These losses, integrated over the lengthy core hydrogen and helium burning evolutionary phases of the star, can be substantial. More efficient, or additional, transport mechanisms (such as the action of magnetic fields) will only exacerbate the core angular momentum losses a single star will suffer during the course of its evolution.

In their single star models for the progenitors of collapsars, Heger & Woosley (2003) find that models which incorporate only hydrodynamic turbulence-induced momentum transport retain a marginally sufficient amount of angular momentum in their cores to form a Kerr black hole and associated torus. When magnetic field-mediated angular momentum transport is included in their calculations, however, the cores of their progenitors lose too much angular momentum and will no longer support an accretion disk.

1.3.2 Binary stars as progenitors of GRBs

In contrast to single stars, a star in a binary system can, in principle, tap the reservoir of angular momentum associated with the orbital motion of the system in order to maintain or increase its core rotation. The amount of angular momentum available in this reservoir can be characterized by the mean "orbital" specific angular momentum,

$$j = \frac{J}{M_1 + M_2} = M_1 M_2 \left[\frac{Ga}{(M_1 + M_2)^3} \right]^{1/2} = 1.70 \times 10^{20}\ \mathrm{cm}^2\,\mathrm{s}^{-1},$$

assuming two 25 $M_\odot$ stars in orbit at a separation $a = 1000 R_\odot$. This reservoir becomes accessible to a member of a binary system when it interacts with its companion, either through the tidal locking of the stars, the exchange of matter between the stars, or the merger of the two stars during a common envelope phase.

Transfer of matter and associated angular momentum from a companion, for instance, can commence during or after the main sequence phase of the accreting star, depending on the parameters of the orbit and the relative masses of the components. The accretor in a late main sequence or post main sequence accretion episode will have less time to lose its acquired angular momentum than a single star (by roughly the main sequence lifetime of the star). More importantly, the injection of angular momentum at the surface of the star will lead to an angular momentum distribution at its core-envelope boundary which is the inverse of the distribution which develops in a single star: A state of differential rotation will arise in which the angular velocity of the envelope will be larger than that of the core. The hydrodynamic or magnetohydrodynamic instabilities which develop will act in this case to transport angular momentum into the core of the star, rather than depleting its angular momentum content as in the case of single stars. Therefore, we expect that, under the proper circumstances, a component of a massive binary system might possess a high core angular momentum content at the time of its core collapse – a crucial ingredient of a successful GRB progenitor.

At least half of all stars are in fact members of binary systems (see, e.g., Abt & Levy 1976, 1978; Duquennoy & Mayor 1991); it is at least as likely that a massive star about to explode in a supernova had a companion during some portion of its evolution than that it evolved in complete isolation.

Interestingly, the first close, naked eye supernova in over 300 years, SN 1987A, has shown strong indications of the binary nature of its progenitor (Podsiadlowski, Joss, & Hsu 1992; Podsiadlowski 1992); indeed, the axisymmetric triple ring system about the SN remnant discovered by the Hubble Space Telescope appears to provide additional support for this point of view (at a minimum, the blue supergiant progenitor of SN 1987 had to have been rapidly rotating, and might have been spun up by a merger with its companion). Intriguingly, the “mystery spot” observed near 1987A approximately one month after the SN (Nisenson et al. 1987; Rees 1987) and its companion spot, discovered by a reanalysis of the original data (Nisenson & Papaliolios 1999), lie on a straight line that passes through the center of the supernova and which is inclined at only $\sim 10^\circ$ from the axis of symmetry of the nebular rings. The original mystery spot had an apparent tangential velocity of $0.46c$ relative to SN 1987A, while the second spot has a superluminal apparent velocity of $1.24c$. Could these two spots be the hallmark of relativitic jets generated by the rotating core collapse which also gave rise to SN 1987A (Cen 1999)?

1.4 Plan of this work

We propose to investigate in this work both the possibility that massive stars which evolve in binary star systems constitute a class of long gamma-ray burst progenitor, and the specific physical mechanisms by which this progenitor class is rendered viable. Chapter 2 describes the stellar evolution code that we developed in order to compute the stellar evolutionary sequences presented herein. Chapter 3 examines the various hydrodynamic instabilities expected to be important in a differentially rotating star, the characteristics of the ensuing turbulence, and the implications for angular momentum transport. Chapter 4 presents a series of evolutionary sequences of possible GRB progenitors, in which the secondary component of the system accretes mass and angular momentum from its companion. In Chapter 5, a common-envelope scenario is investigated, which results in the slow merger of the inspiralling secondary with the core of the primary, and the latter's rapid rotational acceleration. We discuss the results of the preceding two chapters in Chapter 6, paying particular attention to the elements which a putative GRB progenitor must possess to be viable. Finally, in Chapter 7 we close with a summary discussion of the contents of this dissertation.

Chapter 2

Stellar structure with rotation

The computation of stellar structure in one effective dimension has been vigorously pursued over the past half century, aided by the exponential increase in computing power over this period of time. One only has to compare the tedious calculations performed in the 1950's on large, mechanical desktop "calculators" (see, e.g., Schwarzschild 1958) to some of the most recent computational work on stellar evolution (e.g., Maeder & Meynet 2000; Woosley et al. 2002), to appreciate the advances in our understanding facilitated by the growth of computer technology.

When a star is allowed to rotate, the theoretical determination of its structure and temporal evolution becomes a more complicated task. Rotation, especially rapid and/or differential, can alter the equilibrium structure of a star in significant ways (Tassoul 1978, 2000). Differential rotation of the (gaseous) fluid comprising a star gives rise to hydrodynamic instabilities which are not present in nonrotating stars. These new instabilities will affect the time evolution of the stellar angular momentum distribution (Maeder & Meynet 2000). In order to model such processes, two extensions to the usual one-dimensional (1D) numerical models of stellar evolution are required: First, the mechanical effects of rotation must be incorporated into the calculation of the equilibrium structure of stars in an evolutionary sequence, and second, the time stepping calculations which relate two equilibrium models in such a sequence must be extended to include the redistribution of angular momentum and the mixing of nuclear species due to hydrodynamic instabilities.

In the present chapter we describe our implementation of these extensions in a standard Henyey-type stellar evolution code. In § 2.2 we briefly review previous work on rotating stellar structure. § 2.3 describes our approach to determining the equilibrium structure of differentially rotating star. We utilize a variant of a numerical method originally proposed by Kippenhahn & Thomas (1970), which has similarly been implemented by other workers calculating models of rotating stars (Endal & Sofia 1976; Maeder 1997; Heger et al. 2000). We first describe the method under a restrictive form of rotation (angular velocity[1] constant on cylinders concentric with the rotation axis), which makes possible the derivation of exact solutions for the structure of rotating stars which obey such rotation laws. We then relax this restriction and introduce a more general rotational configuration, so-called "shellular" rotation (angular velocity constant on equipotential surfaces), a configuration which most workers in the field assume holds true in real stars in most circumstances. Exact 1D solutions are no longer possible for stars in a state of shellular rotation. Finally, we discuss an approximate solution technique for Poisson's equation which is also widely used and which we have also implemented in our code.

In § 2.4 we describe a new numerical technique which we have developed to solve the system of coupled, non-linear diffusion equations which describes the transport of angular momentum and mixing of nuclear species in the interiors of our stellar models. (We discuss the physical aspects of the instabilities we have included in our calculations in Chapter 3.) In § 2.5 we describe our implementation of stellar wind mass losses and their enhancement by the effects of rotation. Finally in § 2.6 we outline the basic steps in the numerical calculation of one of our evolutionary sequences.

2.1 Definitions

In the following we use both cylindrical and spherical polar coordinate systems, defined relative to the center of the star and the polar axis which passes through this point and about which the star rotates. The spherical polar coordinates r, θ, and ϕ have their usual meanings. The cylindrical coordinate ϖ is the perpendicular distance from the rotation axis, which can be written in terms of the spherical coordinates as

---

[1] Angular frequency and angular velocity are used interchangeably in the present work.

$\varpi = r \sin\theta$, while z is the distance along the rotation axis from the origin and ϕ is the azimuthal angle. The star is assumed to rotate axisymmetrically, such that the angular velocity of the mass element with coordinates ϖ, z (coordinates of the meridional plane) is given by $\Omega(\varpi, z)$.

The "total" potential is defined to be the sum of the gravitational and effective centrifugal potential: $\Psi = \Psi_g + \Psi_c$, where Ψ_g is a solution of Poisson's equation, $\nabla^2\Psi_g = 4\pi G\rho$, and $\nabla\Psi_c = -\Omega^2\varpi\hat{\varpi}$ is the centrifugal force per unit mass (where $\hat{\varpi}$ is the unit vector in the direction perpendicular to the axis of rotation). When $\Omega = \Omega(\varpi)$ is a function only of the distance to the rotation axis, the star is in a state of cylindrical rotation and the total potential is conservative (see § 2.3.1).

2.2 Review of previous work

The equilibrium structure of rotating stars has been the focus of a significant amount of theoretical attention over the past hundred years. Chandrasekhar (1933) studied the structure of slowly and uniformly rotating stars with polytropic equations of state using a first order perturbative technique; Roberts (1963) investigated the structure of rapidly rotating polytropes by utilizing a variational technique, while James (1964) determined the structure of such stars by directly integrating Poisson's equation and the equation of hydrostatic equilibrium using a series expansions of the density and gravitational potential.

The numerical approaches to the problem which followed this early work typically assumed that the star was in a state of cylindrical rotation (Ω a function of ϖ only), which allowed the rotationally modified equations of stellar structure to retain an effectively 1D form (see § 2.3.1). Roxburgh et al. (1965); Faulkner et al. (1968) and later, Sackmann & Anand (1970), assuming solid-body rotation (a special case of cylindrical rotation), divided their models into three zone and applied different approximation techniques in each zone to simplify the computations.

More general solution techniques were introduced by several groups. These allowed the calculation of stellar models in rapid and differential rotation (again assuming rotation on cylinders), and subject to a more general equation of state. All of these methods split the calculation into "equilibrium" and "potential" steps, which had then to be iterated to self-consistency. Ostriker & Mark (1968) introduced the so-called "self-consistent field" (SCF) method for the calculation of the structure of rapidly and differentially rotating white dwarfs. Their initial work assumed a polytropic equation of state, which allowed them to algebraically solve for the equilibrium stellar structure given the total potential (which was computed by expansion in Legendre polynomials). This work was subsequently generalized to apply to massive main sequence stars by Jackson (1970b), who calculated the equilibrium structure of his models using a full-blown Henyey iteration technique. The so-called J^2 technique of Papaloizou & Whelan (1973) solved the effective 1D equations of stellar structure by an equilibrium-potential iteration assuming a cylindrical rotation law, and was essentially equivalent to the SCF method. Kippenhahn & Thomas (1970) recast the equations of rotating stellar structure into a form very similar to the non-rotating equations by introducing the generalized Lagrangian independent variable m_Ψ, the mass enclosed by equipotential surface Ψ.

Using the formalism introduced by Kippenhahn & Thomas (1970), Endal & Sofia (1976) developed a general numerical technique for calculating the structure of differentially rotating stars which is still in wide use today (see, e.g., Pinsonneault et al. 1989; Maeder 1997; Heger et al. 2000). In this work they extended earlier results by incorporating a more detailed (yet still approximate), calculation of the gravitational potential for a rotationally distorted star. They used their stellar evolution code to calculate a number of evolutionary sequences with a simplified treatment of angular momentum redistribution. In Endal & Sofia (1978), the same workers introduced a greatly extended treatment of the hydrodynamic instabilities expected to occur in differentially rotating stars, and the angular momentum redistribution which accompanies the turbulence induced by such instabilities.

It is the basic formulation of Endal & Sofia (1976, 1978) that we follow in the present work.

2.3 Iterative calculation of rotating stellar models

Ideally, the equilibrium structure and total potential (gravitational plus centrifugal) of a rotating stellar model would be computed simultaneously, avoiding the complexity and the tendency to instability of an iterative approach. Such calculations would be very complex in their own right, however, and would require the development ab initio of a new computer code (this approach has been followed in the series of papers Clement 1978, 1979, 1994).

Instead, we choose to follow the formulation of Kippenhahn & Thomas (1970) and split the calculation into two halves, an equilibrium step and a potential step (see below), which are then iterated to self-consistency. This enables us to utilize, for the equilibrium half of our iterations, an advanced 1D stellar structure code which has been continuously updated since its introduction in the late 1960's (Henyey et al. 1959; Kippenhahn et al. 1967; Podsiadlowski 1989).[2] We have modified this code by including correction factors in the basic equations of stellar structure to account for the effects of the centrifugal force (§ 2.3.1). Given a total potential, it produces a corresponding equilibrium density distribution as well as the related physical quantities which specify the mechanical and thermal structure of the model.

The calculation consists of two steps:

- *Equilibrium* step: the structure of the star in hydrostatic equilibrium is determined subject to an externally imposed total (gravitational plus centrifugal) potential;

- *Potential* step: the total potential is calculated from the distribution of mass and angular momentum for a star in hydrostatic equilibrium.

The iteration between these two steps proceeds as follows: The output of the equilibrium calculation, which consists of the mass and angular momentum distributions of a rotating star in hydrostatic equilibrium, is fed into the potential step where the corresponding total potential is calculated for it. The resulting potential is then used as input to the next equilibrium step, in which a new, better-conforming equilibrium structure is determined. If the starting structure is not too far away from its true equilibrium, these iterations tend to converge. Unfortunately, no mathematical theorem

---

[2] Reaction rates utilized in this code were taken from the Caltech compilations of Caughlan & Fowler (1988). High temperature opacity tables are taken from the Los Alamos Astrophysical Opacity Library of Huebner et al. (1977), while for $T < 10000\,K$ the opacity tables calculated by Alexander (1975) are used. Additional carbon and oxygen tables are taken from the Cox-Stewart compilation of opacity tables, Cox & Stewart (1970). Convective overshoot and semiconvection are treated as in Iben (1986). See Podsiadlowski (1989) for a more detailed description of the code.

is currently known which guarantees this convergence for a given set of conditions.

This potential-equilibrium iteration process is continued until the fractional change of each structure variable, $\Delta \log V$, where V is one of (P, T, R, L) is less than a specified small value (which in our calculations is taken to be 10^{-3}), over one iteration. In practice we find that convergence is much easier to obtain when the iteration is started with a model which is already fairly close to convergence. In an evolutionary calculation the previous model of the sequence provides a natural starting model for the iterations of the next time step.

2.3.1 Equilibrium structure

A general computational treatment of the structure of a rotating star must be carried out in at least two dimensions, and ideally three, to allow for completely unconstrained distributions of angular momentum. If the hydrodynamics of fluid instabilities such as convection and the various barotropic and baroclinic instabilities are of interest, the computational requirements become even more extreme. Such a code would have to implement implicit numerical techniques, in order that the vastly differing hydrodynamic, thermal and nuclear time scales which coexist in a rotating star would not cause fatal numerical instabilities. Unfortunately, calculations such as these are still significantly beyond our present computational capacities, despite the exponential increases in computer power and memory capacity which has occured in the past half century. Nonetheless, some preliminary work has been done on two-dimensional stellar models with rotation over the past decade (Deupree 1990, 1995, 1998, 2001). There is also currently an effort under way at the Lawrence Livermore National Laboratory to develop a completely general 3D stellar evolution code (Bazán et al. 2003).

If suitable constraints are applied to the distribution of angular momentum in the interior of the star, and the star is assumed to be axisymmetric about its axis of rotation, then it becomes possible to modify the 1D calculations of traditional, spherically symmetric stellar structure to apply to the more general, rotating case. In particular, if we assume that the stellar rotational configuration is such that its angular velocity $\Omega(\varpi)$ is a function only of the distance from the rotation axis ϖ, then by the Poincare-Wavre theorem (Tassoul 1978), a generalized or total conservative potential Ψ exists (see § 2.1), the gradient of which gives at any point in the star the total force (gravitational plus centrifugal) per unit mass felt by a mass element at that point.

The resulting stellar models are called "pseudo-barotropes" (Tassoul 1978), since, like a real barotropic fluid, the restriction on Ω requires implicitly that the pressure be a function only of the density: $P = P(\rho)$, regardless of the actual equation of state. Solid body rotation is an example of an angular momentum distribution which has an associated total potential. Differential rotation is not excluded, however, since any distribution with $\Omega = \Omega(\varpi)$ will also result in a conservative total potential.

The total potential Ψ provides a natural spatial coordinate for a non-spherical rotating star. The requirement of hydrostatic equilibrium (neglecting circulations),

$$\nabla P = -\rho \, \nabla \Psi \tag{2.1}$$

implies that the pressure P is a function only of Ψ, since their gradients are parallel. In that case, $\rho = -dP/d\Psi$, and density too is constant on surfaces of constant Ψ. The temperature T (given by the equation of state $P = P(T, \rho, X_i)$ where X_i are the composition variables) will also be constant on equipotentials, as long as the composition does not vary on these surfaces.

Using these results, we recast the traditional 1D equations of stellar structure, replacing spherical level surfaces by the (in general, nonspherical) level surfaces of the total potential Ψ (this section follows similar treatments of the problem in Papaloizou & Whelan 1973; Kippenhahn & Thomas 1970; Endal & Sofia 1976). Then all dependent variables become functions of Ψ rather than the radius r or enclosed mass m. In order to retain the form of the spherical stellar structure equations, we express the equations in terms of m_Ψ – the mass enclosed by the equipotential surface Ψ, and introduce the radius-like coordinate r_Ψ, defined such that the volume enclosed by the equipotential Ψ is $V_\Psi = 4\pi r_\Psi^3/3$. The volume element is then given by $dV_\Psi = 4\pi r_\Psi^2 dr_\Psi$, from which the conservation equations of mass and energy follow at once:

$$dm_\Psi = \rho \, dV_\Psi = 4\pi r_\Psi^2 \rho \, dr_\Psi \ , \qquad \text{or} \qquad \frac{dr_\Psi}{dm_\Psi} = \frac{1}{4\pi r_\Psi^2 \rho} \ , \tag{2.2}$$

and

$$dL_\Psi = \rho\varepsilon\, dV_\Psi = \varepsilon\, dm_\Psi \quad \text{or} \quad \frac{dL_\Psi}{dm_\Psi} = \varepsilon \ , \tag{2.3}$$

where $\varepsilon = \varepsilon_{\rm n} + \varepsilon_{\rm g}$, the specific energy generation rate, is the sum of the nuclear rate $\varepsilon_{\rm n}$ and "gravitational" rate $\varepsilon_{\rm g} = T ds/dt$ (see, e.g. Kippenhahn & Weigert 1990).

For the remaining two equations we need to relate differential changes dm_Ψ to $d\Psi$:

$$dm_\Psi = \rho\, dV_\Psi = \rho \int_{S_\Psi} dn\, dS = \rho \int_{S_\Psi} \frac{dn}{d\Psi} d\Psi\, dS \ ,$$

$$\frac{dm_\Psi}{d\Psi} = \rho \int_{S_\Psi} \frac{dS}{|\nabla\Psi|} \ . \tag{2.4}$$

Here the integral is over the equipotential surface S_Ψ, and $dn\, dS$ is an infinitesimal volume element, where dn is an offset normal to S_Ψ. $\rho = \rho(\Psi)$ is constant on equipotential surfaces and so can be taken out from under the integral sign in these expressions. Defining the dimensionless parameter ξ_P by

$$\xi_P \int_{S_\Psi} \frac{dS}{|\nabla\Psi|} = \frac{4\pi r_\Psi^2}{G m_\Psi / r_\Psi^2} \tag{2.5}$$

Eq. (2.4) becomes

$$\frac{d\Psi}{dm_\Psi} = \frac{G m_\Psi}{4\pi\rho r_\Psi^4} \xi_P$$

and the equation of hydrostatic equilibrium takes the form

$$\frac{dP}{dm_\Psi} = -\frac{G m_\Psi}{4\pi r_\Psi^4} \xi_P \ . \tag{2.6}$$

The flux of energy by radiative transport is given by

$$\mathbf{F}_R = -\frac{4}{3} ac \frac{T^3}{\kappa\rho} \nabla T = -\frac{4}{3} ac \frac{T^3}{\kappa\rho} \frac{dT}{d\Psi} \nabla\Psi \ . \tag{2.7}$$

According to von Zeipel's theorem, stellar rotation gives rise to thermal imbalances in radiative regions which are compensated by meridional circulations. The net flux of these currents through an equipotential surface is zero when the star is in a steady state (see, e.g. Jackson 1970a), so they do not appear in the equation of radiative transport. The luminosity emerging from the equipotential surface S_Ψ is thus

$$L_\Psi = \int_{S_\Psi} \mathbf{F}_R \cdot d\mathbf{S} = -\frac{4}{3} ac \frac{T^3}{\kappa\rho} \frac{dT}{d\Psi} \int_{S_\Psi} \nabla\Psi \cdot d\mathbf{S} \ .$$

Rewriting $dT/d\Psi$ in terms of ξ_P and dT/dm_Ψ using Eq. (2.5), and defining a second dimensionless parameter ξ_T by

$$\frac{Gm_\Psi}{r_\Psi^2} 4\pi r_\Psi^2 = \xi_T \int_{S_\Psi} \nabla\Psi \cdot d\mathbf{S} \ , \tag{2.8}$$

the equation of radiative energy transport becomes

$$\frac{dT}{dm_\Psi} = -\frac{3}{64\pi^2} \frac{\kappa}{ac} \frac{L_\Psi}{T^3 r_\Psi^4} \xi_P \xi_T \ . \tag{2.9}$$

We assume that convection in our models is unaffected by rotation (for a discussion of convection in rotating fluids see, e.g., Randers 1942; Cowling 1951; Chandrasekhar 1961). We therefore assume that the temperature gradient is the usual adiabatic one in regions which are convectively unstable by the Schwartzschild criterion (Cox & Giuli 1968). The equation of energy transport then takes its usual form for convective regions with efficient convective heat transport:

$$\frac{dP}{dT} = \frac{P}{T} \nabla_{\rm ad} \ .$$

The dimensionless parameters ξ_P and ξ_T and the radius-like variable r_Ψ defined above are derived from the geometry of the equipotential surfaces and the variation of $|\nabla\Psi|$ over these surfaces. If the star is not rotating, it follows from the definitions Eq. (2.5) and Eq. (2.8) that $\xi_P = \xi_T = 1$. In a rotating star, the non-zero centrifugal force causes the equipotential surfaces to bulge at the equator and flatten at the poles. The divergence of ξ_P from unity and the mean radius r_Ψ reflect this effect in the equations of stellar structure. Rotation also results in non-constant radiative flux over equipotential surfaces. The flux is, in fact, proportional to the local gravitational acceleration at each point of the surface (see Eq. (2.7)), an effect incorporated in the parameter ξ_T.

2.3.2 Total potential

Solving Poisson's equation

The output of the equilibrium step is a density distribution $\rho(\Psi)$ and angular momentum distribution $j(\Psi)$, defined on a set of equipotentials of Ψ, one for each mass shell of the stellar model. From these distributions an updated total potential $\Psi_1 = \Psi_{g,1} + \Psi_{c,1}$ is determined. $\Psi_{g,1}$ is a solution of Poisson's equation for the rotationally distorted density distribution of the star. For the special case of rotation on cylinders, the centrifugal contribution to the updated total potential is given by

$$\Psi_{c,1} = \int^{\varpi} d\varpi \, \frac{j(\varpi)^2}{\varpi^3} \, ,$$

assuming that j is constant on cylinders: $j = \varpi^2\Omega(\varpi)$. In the shellular rotation approximation, $\Psi_{c,1}$ is instead given by $\frac{1}{2}\varpi^2\Omega^2$.

The equilibrium mass distribution $\rho(\Psi)$ is defined on on the equipotential surfaces generated by the previous iteration of the potential step. The corresponding gravitational potential $\Psi_g(r,\theta)$ is completely specified by its value in the meridional plane due to the axisymmetry assumed in the model. We have implemented two numerical methods for calculating the gravitational potential:

- Clement's cell-based method (Clement 1974), in which Poisson's equation is solved in finite-differenced form on a two-dimensional polar grid in the meridional plane;

- the simpler and computationally more efficient method of Endal & Sofia (1976), which expands the potential in a series of tesseral harmonic functions (see, e.g. Kopal 1959), and is better suited to models which are in shellular rotation (see below).

The "exact" solution method utilizing a finite-differenced form of Poisson's equation is in practice only suitable for calculating stellar models which are chemically homogeneous, such as zero-age main sequence stars or white dwarfs (one of the original applications of the SCF method). In inhomogeneous stars, the complications which arise from the non-constancy of T on equipotential surfaces in principle requires models of at least two dimensions. The exact solution method also has the disadvantage of requiring considerable processing time to generate a solution, making evolutionary runs of more than a few tens of models impossible due to computer resource constraints.

For the calculations reported in the present work we have used the the second, approximate solution method for Poisson's equation. This technique is sufficiently accurate for our purposes, especially since we also assume a shellular rotation law holds in our models; hence we are not, in fact, using a truly conservative total potential. Nonetheless, the plausibility of the shellular rotation configuration has been argued by Zahn (1992), who point out that such a distribution of angular velocity would naturally arise given the lack of a stabilizing density gradient on equipotential surfaces (which are also surfaces of constant ρ); see, however, Kippenhahn & Thomas (1981). Indeed, as Meynet & Maeder (1997) have shown, the 1D approach to computing rotating stellar structure described in this chapter remains a good approximation in the case of shellular rotation. It has been widely adopted in subsequent work on rotating stellar structure up to the present day (see, e.g. Krishnamurthi et al. 1997; Heger et al. 2000).

Therefore, we have extended our stellar evolution code to include specific angular momentum $j(m_\Psi)$ as an additional structure variable which, like the others, is a function of the enclosed mass m_Ψ. As mentioned above, we also assume that our models follow a shellular rotation law: $\Omega = \Omega(m_\Psi)$.

Equipotential geometry factors ξ_P and ξ_T

The equilibrium step of our iterations requires a pair of geometry factors, ξ_P and ξ_T, for each mass shell of the model. Given the potential $\Psi(r, \theta)$ we construct a set of equipotential surfaces which spans the interior of the model, with each equipotential surface specified by a function $r_\Psi(\theta)$. Defining $a_\Psi = (1/r_\Psi)(dr_\Psi/d\theta)$, the tangent $\hat{t}_\Psi$ and normal $\hat{n}_\Psi$ to this surface are given by

$$\left(1 + a_\Psi^2\right)^{1/2} \hat{t}_\Psi = a_\Psi \hat{r} + \hat{\theta}$$

$$\left(1 + a_\Psi^2\right)^{1/2} \hat{n}_\Psi = \hat{r} - a_\Psi \hat{\theta}$$

and the gradient of Ψ by

$$\nabla\Psi = \left(\frac{\partial\Psi}{\partial r}\right)\left[\hat{r} - a_\Psi\hat{\theta}\right] \tag{2.10}$$

$$|\nabla\Psi| = \left(\frac{\partial\Psi}{\partial r}\right)\left(1 + a_\Psi^2\right)^{1/2}. \tag{2.11}$$

The element of equipotential surface area $\mathbf{dS}_\Psi$ is given by

$$\mathbf{dS}_\Psi = \frac{2\pi r_\Psi^2 d\mu}{\hat{r}\cdot\hat{n}_\Psi}\hat{n}_\Psi = 2\pi\left(1 + a_\Psi^2\right)^{1/2} r_\Psi^2 \hat{n}_\Psi d\mu$$

where $\mu = \cos\theta$. With these definitions we can compute the quantities needed in the equilibrium step: the volume V_Ψ contained within an equipotential surface (giving the mean radius r_Ψ of this surface),

$$V_\Psi = \frac{1}{3}\int_\Psi \mathbf{r}\cdot\mathbf{dS}_\Psi = \frac{4\pi}{3}\int_0^1 r_\Psi^3\, d\mu \tag{2.12}$$

and the two surface integrals which enter into the definitions of ξ_P and ξ_T,

$$\int_{S_\Psi} \nabla\Psi\cdot d\mathbf{S} = 4\pi\int_0^1 \left(\frac{\partial\Psi}{\partial r}\right)\left(1 + a_\Psi^2\right) r_\Psi^2\, d\mu \tag{2.13}$$

and

$$\int_{S_\Psi} \frac{dS}{|\nabla\Psi|} = 4\pi\int_0^1 \frac{\left(1 + a_\Psi^2\right)^{1/2} r_\Psi^2\, d\mu}{\partial\Psi/\partial r} \tag{2.14}$$

In practice, we define an equipotential surface as consisting of the discrete set of coordinate pairs, (r_i, θ_i) for $i = 1 \ldots N$, where $i = 1$ corresponds to the rotation axis ($\theta = 0$), and $i = N$ to the equatorial plane ($\theta = \pi/2$). The angles θ_i are chosen such that the corresponding $\mu_i = \cos\theta_i$ are located at the Lobbato points of the interval $[0, 1]$ (see, e.g. Hildebrand 1956). The integrals in Eqs. (2.12-2.14) over $d\mu$ can then be accurately computed using the corresponding Lobbato N-point quadrature formulae. We approximate the function $r_\Psi(\theta)$ in order to compute a_Ψ by fitting to the set of points (r_i, θ_i) a cubic spline curve, which has the desirable property that its first derivative is continuous throughout its domain of definition.

The geometry factors ξ_P and ξ_T can be considered as functions of the equipotential mean radius r_Ψ. r_Ψ is also a dependent variable of the stellar models. It is calculated along with P, T and L in the equilibrium step as a function of the enclosed mass m_Ψ (the independent variable). Thus, r_Ψ provides a bridge between the potential and equilibrium steps of the iteration.

2.4 Angular momentum transport and mixing

2.4.1 Relevant time scales

Mixing in our models can occur on several, generally quite different time scales. The most vigorous occurs in regions of the star which are subject to hydrodynamic instabilities such as convection or adiabatic (dynamical) shear instability. These instabilities are characterized by the local dynamical time scale of the model (which is proportional to N^{-1}, the inverse of the local buoyancy frequency [see § 3.1.3]). Mixing can also occur on the longer thermal or Kelvin-Helmholtz time scale of the star, $\tau_{\rm KH} \gg \tau_{\rm dyn}$, due to, for example, the breakdown of adiabaticity in an otherwise dynamically stable stratified shear flow. On the other hand, the evolutionary sequences calculated in the present work are characterized by three time scales: the time scale of nuclear processes in the core $\tau_{\rm n}$, the accretion time scale $\tau_{\rm acc} = \Delta M/\dot{M}$ (where ΔM is the accreted mass), or $\tau_{\rm KH}$.

2.4.2 Diffusion equations

We model the transport of angular momentum and mixing of chemical species in the star using the coupled set of non-linear diffusion equations

$$\left(\frac{\partial \Omega}{\partial t}\right)_m = \frac{1}{r_g^2}\left(\frac{\partial}{\partial m}\right)_t\left[\left(4\pi\rho r^2\right)^2 r_g^2 \nu \left(\frac{\partial \Omega}{\partial m}\right)_t\right] \tag{2.15}$$

for angular momentum (see Chapter 3), and

$$\left(\frac{\partial X_k}{\partial t}\right)_m = \left(\frac{\partial}{\partial m}\right)_t\left[\left(4\pi\rho r^2\right)^2 D \left(\frac{\partial X_k}{\partial m}\right)_t\right] \tag{2.16}$$

for the mixing of K chemical (i.e., nuclear) species k, where $k = 1, K$. Eq. (2.15) expresses the conservation of angular momentum, under the action of a turbulent viscous force with effective eddy viscosity ν. $\Omega(m,t)$ is the angular frequency of rotation and $r_g(m)$ is the radius of gyration of mass shell m. The remaining K equations express the conservation of each nuclear species k in the diffusion approximation, where X_k is the mass fraction of species k.

These equations are coupled via the functional dependence of the eddy viscosity ν on the mean molecular weight $\mu(X_i)$, and the dependence of the eddy diffusivity D on the angular velocity Ω. The radial variable r is replaced in these equations by the enclosed mass m using the equation of continuity, $dm = 4\pi r^2 \rho dr$.[3]

2.4.3 Boundary conditions

At the core, we assume reflective boundary conditions apply at all times,

$$\left(\frac{\partial \Omega}{\partial m}\right)\bigg|_{\text{core}} = \left(\frac{\partial X_k}{\partial m}\right)\bigg|_{\text{core}} = 0\,. \tag{2.17}$$

The boundary conditions appropriate to the surface of the star depend on the current stage of evolution of the model. When the star is not accreting mass, we apply a reflective boundary condition at the surface as well as at the core:

$$\left(\frac{\partial \Omega}{\partial m}\right)\bigg|_{\text{surf}} = \left(\frac{\partial X_k}{\partial m}\right)\bigg|_{\text{surf}} = 0\,. \tag{2.18}$$

The reflective boundary conditions for Ω ensures that the total angular momentum of the model is conserved during non-accretion phases of evolution. The surface layer during these evolutionary phases is assumed to be held to sub-critical (sub-Keplerian) rotation velocities by the action of a rotationally enhanced stellar wind. As the angular velocity, $\Omega_{\text{surf}} = \Omega(M)$ (where M is the total mass of the star), of the surface approaches the critical angular velocity in the equatorial plane, $\Omega_{\text{k,eq}}$,[4] the wind mass loss rate increases without bound (see § 2.5). The super-critical surface layer is stripped from the star by the action of the wind, and the layers below allowed to relax to a new state of equilibrium. This process naturally maintains the surface

---

[3] We drop the subscript Ψ in the present discussion for clarity; however, the variables m, r etc. are defined relative to equipotentials of the total potential Ψ, as discussed in § 2.3.1.

[4] ${\Omega_{\text{k,eq}}}^2 = GM/R_{\text{eq}}^3$ where M is the mass of the star and R_{eq} its radius in the equatorial plane

angular velocity $\Omega_{\rm surf}$ at sub-critical levels.

We divide the accretion event itself into two phases: in the first phase, $\Omega_{\rm surf} < \Omega_{\rm k,eq}$ and reflective boundary conditions are applied at the surface. As mass is accreted, $\Omega_{\rm surf}$ increases, eventually approaching the critical angular velocity $\Omega_{\rm k,eq}$. The first accretion phase terminates when $\Omega_{\rm surf}$ reaches $f\Omega_{\rm k,eq}$, where $f < 1$ is a dimensionless parameter. We chose $f = 0.9$ to avoid numerical convergence problems, which we find arise in the rotation/structure iterations during the accretion process when f is taken too close to unity.

When critical rotation is reached at the surface of the model the second accretion phase begins, in which the reflective boundary condition on Ω at the surface is replaced by one fixing its value at $f\Omega_{\rm k,eq}$ (which itself varies with time as the accretion proceeds): explicitly, this condition takes the form $\Omega(M) = f\Omega_{\rm k,eq}$. In practice, this condition results in the loss of angular momentum through the surface of the star. Angular momentum is transported down the gradient in Ω, which is decreasing outward in the outermost layers of the envelope during most of this phase. We assume that this excess angular momentum is carried away from the surface of the star by the accretion disk, which is simultaneously feeding the star more mass.[5] $\Omega_{\rm surf}$ remains fixed at this value as long as the accretion of mass and associated angular momentum onto the star maintains the angular velocity of its surface zone at the critical value. In practice, this is the case for the remainder of the second accretion phase (see Chapter 4).

2.4.4 Relaxation solution of mixing equations

Two-point boundary value problems

We have developed an algorithm to solve the system Eqs. (2.15-2.16) and associated boundary conditions, which takes as its motivation the numerical technique originally introduced by Henyey et al. (1959) to solve the equations of stellar structure.[6] In their usual formulation, the four equations of stellar structure (see § 2.3.1) are

---

[5] Some fraction of the angular momentum feed back into the disk from the star will ultimately be returned to the orbit of the system through tidal interactions at the edge of the disk.

[6] See Kippenhahn et al. (1967) for a detailed explication of the so-called Henyey method as it is implemented in modern stellar evolution codes.

supplemented by four boundary conditions, two of which are specified at the surface of the star, and the other two at its center. Simple numerical integration schemes such as Runge-Kutta, which assume all boundary conditions apply at one point (typically the starting point of the step-wise integration), must be extended in order to handle such systems, which are distinguished by having boundary conditions which are spatially divided across the domain of integration.

One set of techniques for solving systems of partial differential with split boundary conditions are the so-called "shooting" methods (see e.g. Press et al. 1992). In a typical shooting calculation the integration is started at both boundaries simultaneously (or, in simpler schemes, at only one of the boundaries), and continued to an intermediate meeting point (or possibly the other boundary). The solutions are compared at this point: if they differ (i.e. the solution not yet sucessfully obtained) adjustments are made to the initial conditions at both boundaries and the system of equations is integrated again. This process is continued until the adjusted boundary conditions yield a sufficiently good match at the intermediate meeting point.

Another method applicable to split boundary condition problems is solution by "relaxation." In this case, the original differential equations and their associated boundary conditions are replaced by a set of finite-difference equations. A trial solution of these latter equations (a solution which, early in the solution process, might only approximately satisfy the difference equations) is then iteratively improved at all points of the domain simultaneously; this iterative solution process is a multidimensional generalization of the usual, one dimensional Newton-Raphson iteration.

The Henyey method as applied to the equations of stellar structure is a prototypical example of the relaxation solution of a system of differential equation with split boundary conditions. We have chosen to solve the system of mixing equations Eqs. (2.15-2.16) by an analogous relaxation technique, described in more detail in the following section.

2.4.5 Finite-difference equations

There are a number of possible sets of finite-difference equations corresponding to the system Eqs. (2.15-2.16) (see Press et al. 1992, for a general discussion). The simplest are those of *explicit* form, in which quatities to be determined at the forward time point $t + \Delta t$ are explicitly expressed in terms of known quantities at time point t. The simplicitly comes at a cost, however: to avoid numerical instability, the time step used for a system of explicit difference equations is limited to the Courant time of the model.[7]. The turbulent diffusion coefficients ν and D in our models are largest in regions undergoing mixing by processes which operate on a dynamical time scale, such as convection or turbulence caused by adiabatic shear instability (see § 2.4.1). The small time steps needed to follow the evolution of such dynamically unstable regions in an explicit finite-differencing scheme are unacceptable in a calculation running over the much-longer time intervals typifying stellar evolution.

We therefore chose to use an *implicit* finite-difference form of the mixing equations. Implicit difference equations have the desirable property of absolute stability regardless of time step, even for time steps which exceed the smallest time scales of the system under study (Smith 1985). Their drawback is the additional complexity of solving the resultin system of equations for the implicitly defined dependent variables. In our case, the difference equations in their implicit form are nonlinear, requiring an iterative method for their solution.

We label the N mass shells of an equilibrium stellar model by index i, $i = 1 \ldots N$, where $i = 1$ is the outermost shell (surface of the star) and $i = N$ is the center of the core ($r = m = 0$). The finite-differenced form of the system 2.15-2.16 links triplets of mass shells $(i-1, i, i+1)$ from time point t to $t + \Delta t$. They take the form:

$$\frac{\Omega_i - \Omega_i^\star}{\Delta t} - P_{i+\frac{1}{2}}(\Omega_{i+1} - \Omega_i) + P_{i-\frac{1}{2}}(\Omega_{i-1} - \Omega_i) = 0 \tag{2.19}$$

$$\frac{X_{k,i} - X_{k,i}^\star}{\Delta t} - Q_{i+\frac{1}{2}}(X_{k,i+1} - X_{k,i}) + Q_{i-\frac{1}{2}}(X_{k,i-1} - X_{k,i}) = 0 \tag{2.20}$$

for $i = 2 \ldots N-1$ and $k = 1 \ldots K$. These equations are solved for the dependent variables Ω_i and $X_{k,i}$ (the angular velocity and species abundances for mass shell i at the forward time $t + \Delta t$) in terms of the known quantities, $\Omega_i^\star$, $X_{k,i}^\star$ at time t. The coefficients $P_{i-\frac{1}{2}}$, $Q_{i+\frac{1}{2}}$, etc. are functions of the dependent variables at the forward time $t + \Delta t$, since they depend explicitly on the eddy viscosity ν and eddy diffusivity

---

[7] This time is proportional to the minimum mass shell crossing time, $\Delta t_c \approx (\Delta r)^2/D$ in the model.

D, respectively, which are themselves functions of Ω and X_k:

$$P_{i-\frac{1}{2}} = P_{i-\frac{1}{2}}[\nu(\Omega_i, \Omega_{i-1}, X_{k,i}, X_{k,i-1}), D, \ldots]$$

$$P_{i+\frac{1}{2}} = P_{i+\frac{1}{2}}[\nu(\Omega_i, \Omega_{i+1}, X_{k,i}, X_{k,i+1}), D, \ldots]$$

and similarly for Q, with the turbulent viscosity ν replaced by diffusivity D.

For a model with N mass zones, there are $N-2$ such systems of $K+1$ equations each (one equation for angular momentum transport, and K for nuclear species diffusion), involving a total of $N(K+1)$ dependent variables: Ω_i, $X_{k,i}$, $k = 1 \ldots K$ associated with each shell i, $i = 1 \ldots N$. The $2(K+1)$ missing equations are provided by the boundary conditions, which provide $K+1$ equations at the core and $K+1$ at the outer edge of the star. The diffusion equations, Eqs. (2.15-2.16), are second-order in space, which is manifested in their finite-difference counterparts Eqs. (2.19-2.20) by the linkage of three mass shells $(i-1, i, i+1)$, $i = 2 \ldots N-1$ in each equation. In contrast, the first-order equations of stellar structure yield finite-difference equations which link pairs of mass shells $(i, i+1)$.

The order of our system can be reduced from two to one by introducing supplementary functions and doubling the number of differential equations. The usual Henyey method could then be applied to the equivalent first order system. While the two systems are formally mathematically equivalent, their finite-difference representations are not, with consequences for the numerical solutions obtained. Twice as many Taylor-expansion truncations are necessary in the finite-difference representation of the first order system as compared to that derived directly from the second order equations. The consequently increased truncation-induced numerical error can destabilize an iterative solution technique (Collatz 1960, chap. III). Eggleton (1972) took the first order approach when he developed an implicit numerical method for calculating the diffusion of chemical species in his stellar models. He found that substantial care was required in the formulation of suitable finite-difference equations, otherwise the relaxation iterations were not convergent.

To avoid such numerical difficulties, we chose to solve the system directly in its original, second order form, in the hope that eliminating the supplementary functions which arise in a split to first order would stabilize the resulting iterations. We have found that our system of equations, and the numerical technique we developed for their solution, are indeed stable and well-behaved.

2.4.6 Relaxation iterations: general structure

The relaxation solution of Eqs. (2.15-2.16) with appropriate boundary conditions (see § 2.4.3) consists of solving by Newton-Raphson iteration the corresponding finite-difference equations Eqs. (2.19-2.20) (along with the associated finite-differenced boundary conditions).[8] In the present section we describe the numerical details of our solution technique, applied for simplicity to a system limited to only two nuclear species.

The finite-difference equations which we wish to solve for the transport of angular momentum and mixing of nuclear species take the form

$$\begin{aligned} M_i(\Omega_{i-1}, X_{i-1}, Y_{i-1}, \Omega_i, X_i, Y_i, \Omega_{i+1}, X_{i+1}, Y_{i+1}) &= 0 \qquad (2.21)\\ A_i(\Omega_{i-1}, X_{i-1}, Y_{i-1}, \Omega_i, X_i, Y_i, \Omega_{i+1}, X_{i+1}, Y_{i+1}) &= 0 \qquad (2.22)\\ B_i(\Omega_{i-1}, X_{i-1}, Y_{i-1}, \Omega_i, X_i, Y_i, \Omega_{i+1}, X_{i+1}, Y_{i+1}) &= 0 \qquad (2.23) \end{aligned}$$

at grid point i, where X_i and Y_i are the mass fractions of the two nuclear species. Eq. (2.21) is the finite-difference equation for angular momentum transport, while Eq. (2.22) and Eq. (2.23) are the corresponding equations for the mixing of the nuclear species X and Y, respectively.

During the course of the Newton-Raphson iterations, these variables will have values $\Omega_{i-1,0}$, $X_{i-1,0}, \ldots$ which do not yet satisfy Eqs. (2.21-2.23). The iteration consists in determining the corrections $\delta\Omega_{i-1}$, $\delta X_{i-1}, \ldots$ such that the updated values $\Omega_{i-1,1} = \Omega_{i-1,0} + \delta\Omega_{i-1}, \ldots$ are closer to a solution of the equations. Expanding

---

[8] As noted above, these equations are, in general, nonlinear in the dependent variables.

Eq. (2.21) and retaining only terms linear in the corrections yields

$$\begin{aligned} M_{i,0} &+ \left.\frac{\partial M_i}{\partial \Omega_{i-1}}\right|_0 \delta\Omega_{i-1} + \left.\frac{\partial M_i}{\partial X_{i-1}}\right|_0 \delta X_{i-1} + \left.\frac{\partial M_i}{\partial Y_{i-1}}\right|_0 \delta Y_{i-1} \qquad (2.24)\\ &+ \left.\frac{\partial M_i}{\partial \Omega_{i}}\right|_0 \delta\Omega_{i} + \left.\frac{\partial M_i}{\partial X_{i}}\right|_0 \delta X_{i} + \left.\frac{\partial M_i}{\partial Y_{i}}\right|_0 \delta Y_{i}\\ &+ \left.\frac{\partial M_i}{\partial \Omega_{i+1}}\right|_0 \delta\Omega_{i+1} + \left.\frac{\partial M_i}{\partial X_{i+1}}\right|_0 \delta X_{i+1} + \left.\frac{\partial M_i}{\partial Y_{i+1}}\right|_0 \delta Y_{i+1} = 0\,, \end{aligned} \qquad (2.25)$$

and similarly for the abundance mixing equations

$$A_{i,0} + \left.\frac{\partial A_i}{\partial \Omega_{i-1}}\right|_0 \delta\Omega_{i-1} + \left.\frac{\partial A_i}{\partial X_{i-1}}\right|_0 \delta X_{i-1} + \cdots = 0 \qquad (2.26)$$

$$B_{i,0} + \left.\frac{\partial B_i}{\partial \Omega_{i-1}}\right|_0 \delta\Omega_{i-1} + \left.\frac{\partial B_i}{\partial X_{i-1}}\right|_0 \delta X_{i-1} + \cdots = 0 \qquad (2.27)$$

$$(2.28)$$

$M_{i,0}$, $A_{i,0}$ and $B_{i,0}$ are a measure of the residual error remaining in the current solution:

$$M_{i,0} = M_i(\Omega_{i-1,0}, X_{i-1,0}, \Omega_{i,0}, X_i, Y_{i,0}, \Omega_{i+1,0}, X_{i+1,0}, Y_{i+1,0})$$

and similarly for $A_{i,0}$ and $B_{i,0}$. The residuals are expected to approach zero quadratically for converging Newton-Raphson iterations.

If our simplified model has $N = 5$ grid points, there will be 3 equations of the form Eqs. (2.24-2.27) for each grid point $i = 2, 3, 4$, plus 3 equations expressing the boundary condition at the points $i = 1$ and $i = 5$, for a total of 15 equations. This system of equations must be solved for the 15 corrections $(\delta\Omega_i, \delta X_i, \delta Y_i)$, $i = 1 \ldots 5$ which are used to update the dependent variables for the next iteration, $\Omega_{i,1} = \Omega_{i,0} + f\delta\Omega_i$, $X_{i,1} = X_{i,0} + f\delta X_i$, etc.[9] The matrix representation of this system of equations has a special block-banded structure, illustrated schematically in Fig. 2-

---

[9] In the calculations reported in this dissertation we have typically taken f less than one. This tends to damp any oscillations between iterations, at the cost of a greater number of iterations required to obtain a converged solution.

1; Fig. 2-2 shows two blocks of this matrix in greater detail, corresponding to the grid points $i-1$ and i. In a full evolutionary calculation, this matrix is typically of dimension $\sim 5000 \times 5000$, and it must be inverted roughly 30 times per time step of the evolutionary sequence. Generic numerical solution techniques which do not take advantage of the special structure of this matrix are not computationally viable for a matrix of this size. The solution method which we developed to exploit this structure is described in more detail in Appendix A.

2.4.7 Mixing calculation overview

The maximum of the fractional corrections $\delta\Omega_{i-1}/\Omega_{i-1}$, $\delta X_{i-1}/X_{i-1}$, etc. for a given iteration is used as a gauge of the convergence of the process. We accept the current solution when this measure falls below a pre-determined bound (10^{-3} in the calculations reported in the present work).

The mixing calculation is carried out through a time interval Δt which separates pairs of equilibrium stellar models in the evolutionary sequence. The initial mixing time step is set to $\Delta t/10$, and allowed to vary depending on the quality of convergence of the iterations. If the iterations do not converge, the time step is reduced to $\Delta t/2$ and iterations restarted. This process is repeated until convergence is achieved, or the timestep is reduced to less than the dynamical time scale. In general, the solutions behave as one would expect based on the relative time scales: regions which are mixed on a dynamical time scale "instantaneously" readjust (relative to the longer evolutionary timescales τ_{KH} or τ_{n} of the star) to a marginally stable condition given by the Richardson criterion (see § 3.1.3); regions which are convectively unstable instantaneously adjust to uniform angular velocity and composition. Regions which are only secularly unstable mix on the longer Kelvin-Helmholtz time scale, which might not bring them into marginal stability if the evolutionary time scale is shorter than the mixing time scale (during accretion, for example). See Chapter 4 for further details.

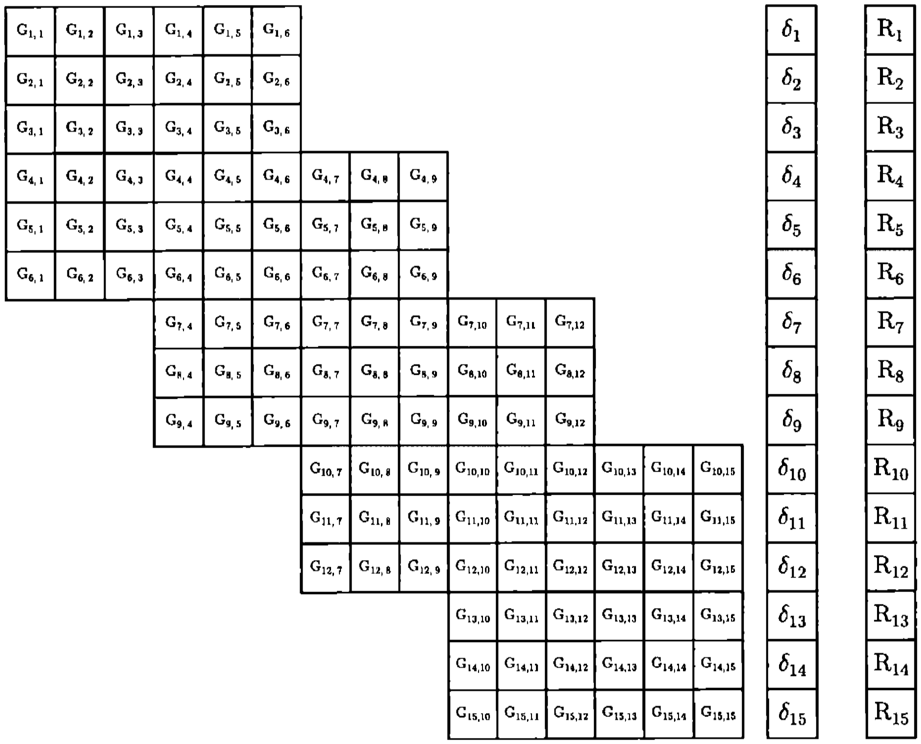

$$
\begin{array}{|ccccccccccccccc|}
G_{1,1} & G_{1,2} & G_{1,3} & G_{1,4} & G_{1,5} & G_{1,6} & & & & & & & & & \\
G_{2,1} & G_{2,2} & G_{2,3} & G_{2,4} & G_{2,5} & G_{2,6} & & & & & & & & & \\
G_{3,1} & G_{3,2} & G_{3,3} & G_{3,4} & G_{3,5} & G_{3,6} & & & & & & & & & \\
G_{4,1} & G_{4,2} & G_{4,3} & G_{4,4} & G_{4,5} & G_{4,6} & G_{4,7} & G_{4,8} & G_{4,9} & & & & & & \\
G_{5,1} & G_{5,2} & G_{5,3} & G_{5,4} & G_{5,5} & G_{5,6} & G_{5,7} & G_{5,8} & G_{5,9} & & & & & & \\
G_{6,1} & G_{6,2} & G_{6,3} & G_{6,4} & G_{6,5} & G_{6,6} & G_{6,7} & G_{6,8} & G_{6,9} & & & & & & \\
 & & & G_{7,4} & G_{7,5} & G_{7,6} & G_{7,7} & G_{7,8} & G_{7,9} & G_{7,10} & G_{7,11} & G_{7,12} & & & \\
 & & & G_{8,4} & G_{8,5} & G_{8,6} & G_{8,7} & G_{8,8} & G_{8,9} & G_{8,10} & G_{8,11} & G_{8,12} & & & \\
 & & & G_{9,4} & G_{9,5} & G_{9,6} & G_{9,7} & G_{9,8} & G_{9,9} & G_{9,10} & G_{9,11} & G_{9,12} & & & \\
 & & & & & & G_{10,7} & G_{10,8} & G_{10,9} & G_{10,10} & G_{10,11} & G_{10,12} & G_{10,13} & G_{10,14} & G_{10,15} \\
 & & & & & & G_{11,7} & G_{11,8} & G_{11,9} & G_{11,10} & G_{11,11} & G_{11,12} & G_{11,13} & G_{11,14} & G_{11,15} \\
 & & & & & & G_{12,7} & G_{12,8} & G_{12,9} & G_{12,10} & G_{12,11} & G_{12,12} & G_{12,13} & G_{12,14} & G_{12,15} \\
 & & & & & & & & & G_{13,10} & G_{13,11} & G_{13,12} & G_{13,13} & G_{13,14} & G_{13,15} \\
 & & & & & & & & & G_{14,10} & G_{14,11} & G_{14,12} & G_{14,13} & G_{14,14} & G_{14,15} \\
 & & & & & & & & & G_{15,10} & G_{15,11} & G_{15,12} & G_{15,13} & G_{15,14} & G_{15,15}
\end{array}
\quad
\begin{array}{|c|}
\delta_1 \\ \delta_2 \\ \delta_3 \\ \delta_4 \\ \delta_5 \\ \delta_6 \\ \delta_7 \\ \delta_8 \\ \delta_9 \\ \delta_{10} \\ \delta_{11} \\ \delta_{12} \\ \delta_{13} \\ \delta_{14} \\ \delta_{15}
\end{array}
\quad
\begin{array}{|c|}
R_1 \\ R_2 \\ R_3 \\ R_4 \\ R_5 \\ R_6 \\ R_7 \\ R_8 \\ R_9 \\ R_{10} \\ R_{11} \\ R_{12} \\ R_{13} \\ R_{14} \\ R_{15}
\end{array}
$$

Figure 2-1: The structure of the matrix equation to be solved as part of the Newton-Raphson iterative solution of the finite-difference system, Eqs. (2.19-2.20), for the case of $N = 5$ grid points and 3 quantities subject to mixing (angular momentum and two nuclear species). The matrix elements $G_{i,j}$ are labelled by row and column indices i and j, respectively, and correspond to the coefficients in the linear expansions, Eqs. (2.24-2.27) (see also Fig. 2-2). The 3×6 blocks at the top-left and bottom-right of the matrix encode the boundary conditions at the surface and core of the model, respectively. All matrix elements not otherwise specifically labelled are zero. The column vector to the immediate right of the coefficient matrix contains the corrections to be determined in the current iteration. The rightmost column vector contains the current residuals of the finite-difference equations.

$$
\begin{array}{|c|c|c|c|c|c|c|c|c|c|c|c|}
\hline
\frac{\partial M_{i-1}}{\partial \Omega_{i-2}} & \frac{\partial M_{i-1}}{\partial X_{i-2}} & \frac{\partial M_{i-1}}{\partial Y_{i-2}} & \frac{\partial M_{i-1}}{\partial \Omega_{i-1}} & \frac{\partial M_{i-1}}{\partial X_{i-1}} & \frac{\partial M_{i-1}}{\partial Y_{i-1}} & \frac{\partial M_{i-1}}{\partial \Omega_{i}} & \frac{\partial M_{i-1}}{\partial X_{i}} & \frac{\partial M_{i-1}}{\partial Y_{i}} & & & \\
\hline
\frac{\partial A_{i-1}}{\partial \Omega_{i-2}} & \frac{\partial A_{i-1}}{\partial X_{i-2}} & \frac{\partial A_{i-1}}{\partial Y_{i-2}} & \frac{\partial A_{i-1}}{\partial \Omega_{i-1}} & \frac{\partial A_{i-1}}{\partial X_{i-1}} & \frac{\partial A_{i-1}}{\partial Y_{i-1}} & \frac{\partial A_{i-1}}{\partial \Omega_{i}} & \frac{\partial A_{i-1}}{\partial X_{i}} & \frac{\partial A_{i-1}}{\partial Y_{i}} & & & \\
\hline
\frac{\partial B_{i-1}}{\partial \Omega_{i-2}} & \frac{\partial B_{i-1}}{\partial X_{i-2}} & \frac{\partial B_{i-1}}{\partial Y_{i-2}} & \frac{\partial B_{i-1}}{\partial \Omega_{i-1}} & \frac{\partial B_{i-1}}{\partial X_{i-1}} & \frac{\partial B_{i-1}}{\partial Y_{i-1}} & \frac{\partial B_{i-1}}{\partial \Omega_{i}} & \frac{\partial B_{i-1}}{\partial X_{i}} & \frac{\partial B_{i-1}}{\partial Y_{i}} & & & \\
\hline
& & & \frac{\partial M_{i}}{\partial \Omega_{i-1}} & \frac{\partial M_{i}}{\partial X_{i-1}} & \frac{\partial M_{i}}{\partial Y_{i-1}} & \frac{\partial M_{i}}{\partial \Omega_{i}} & \frac{\partial M_{i}}{\partial X_{i}} & \frac{\partial M_{i}}{\partial Y_{i}} & \frac{\partial M_{i}}{\partial \Omega_{i+1}} & \frac{\partial M_{i}}{\partial X_{i+1}} & \frac{\partial M_{i}}{\partial Y_{i+1}} \\
\hline
& & & \frac{\partial A_{i}}{\partial \Omega_{i-1}} & \frac{\partial A_{i}}{\partial X_{i-1}} & \frac{\partial A_{i}}{\partial Y_{i-1}} & \frac{\partial A_{i}}{\partial \Omega_{i}} & \frac{\partial A_{i}}{\partial X_{i}} & \frac{\partial A_{i}}{\partial Y_{i}} & \frac{\partial A_{i}}{\partial \Omega_{i+1}} & \frac{\partial A_{i}}{\partial X_{i+1}} & \frac{\partial A_{i}}{\partial Y_{i+1}} \\
\hline
& & & \frac{\partial B_{i}}{\partial \Omega_{i-1}} & \frac{\partial B_{i}}{\partial X_{i-1}} & \frac{\partial B_{i}}{\partial Y_{i-1}} & \frac{\partial B_{i}}{\partial \Omega_{i}} & \frac{\partial B_{i}}{\partial X_{i}} & \frac{\partial B_{i}}{\partial Y_{i}} & \frac{\partial B_{i}}{\partial \Omega_{i+1}} & \frac{\partial B_{i}}{\partial X_{i+1}} & \frac{\partial B_{i}}{\partial Y_{i+1}} \\
\hline
\end{array}
\quad
\begin{array}{|c|}
\hline
\delta\Omega_{i-2} \\ \hline \delta X_{i-2} \\ \hline \delta Y_{i-2} \\ \hline \delta\Omega_{i-1} \\ \hline \delta X_{i-1} \\ \hline \delta Y_{i-1} \\ \hline \delta\Omega_{i} \\ \hline \delta X_{i} \\ \hline \delta Y_{i} \\ \hline \delta\Omega_{i+1} \\ \hline \delta X_{i+1} \\ \hline \delta Y_{i+1} \\ \hline
\end{array}
\quad
\begin{array}{|c|}
\hline
-M_{i-1,0} \\ \hline -A_{i-1,0} \\ \hline -B_{i-1,0} \\ \hline -M_{i,0} \\ \hline -A_{i,0} \\ \hline -B_{i,0} \\ \hline
\end{array}
$$

Figure 2-2: A detailed section of the array shown in Fig. 2-1, illustrating the contents of each matrix element. The two blocks shown correspond to grid points $i-1$ and i; they link all the grid points in the range $i-2$ to $i+1$.

2.5 Rotationally enhanced stellar winds

Following Langer (1998), the critical luminosity and corresponding critical factor are defined by

$$
\begin{aligned}
L_{crit} &= \frac{4\pi c G M}{\kappa}, \\
\Gamma &= \frac{L}{L_{crit}} = \frac{\kappa L}{4\pi c G M},
\end{aligned}
$$

respectively. The gravitational acceleration at the stellar surface, reduced by the radiation pressure gradient, can then be written in the form of an effective acceleration

$$
\frac{GM}{R^2} - \frac{\kappa L}{4\pi c R^2} = (1-\Gamma)\frac{GM}{R^2} .
$$

A rotating layer reaches its critical velocity when the centrifugal force per unit mass just balances the effective acceleration,

$$
v_{crit}^2 = (1-\Gamma)\frac{GM}{R^2} .
$$

Langer (1998) defines a parameter Ω_{w} which characterizes how close the surface layer is to critical rotation

$$\Omega_{\mathrm{w}}{}^2 = \left(\frac{v}{v_{crit}}\right)^2 = \frac{v^2}{(1-\Gamma)GM/R} \, .$$

Based on the results of Friend & Abbott (1986), we introduce a factor which characterizes the rotational enhancement of the base rate of mass loss via stellar winds, $\dot{M}(\Omega = 0)$:

$$\dot{M}(\Omega) = \left(\frac{1}{1-\Omega}\right)^{\xi} \dot{M}(\Omega = 0) \, .$$

A fit to the data of Friend & Abbott (1986) gives $\xi \approx 0.43$.

In our calculations the above mass-loss enhancement is applied to the basic wind mass loss rate given by Nieuwenhuijzen & de Jager (1990):

$$-\dot{M}(\Omega = 0) = 9.6310^{-15}(L/L_{\odot})^{1.42}(M/M_{\odot})^{0.16}(R/R_{\odot})^{0.81} M_{\odot} \mathrm{y} r^{-1} \, ,$$

which expresses the rate as a function of the mass of the stellar model and its position in the HR diagram.

2.6 Outline of the evolutionary calculation

A time step in the sequence of models forming an evolutionary sequence consists of the following substeps:

(1) Extrapolate previous two models forward to form first estimate of current model

(2) Adjust computational mesh to fit extrapolated model

(3) Determine outer boundary condition triangle

(4) Perform Henyey relaxation iterations to yield a converged model in hydrostatic equilibrium, assuming a fixed potential structure parameterized by ξ_P, ξ_T from the previous potential step

(5) Compare new equilibrium model with previous; if the differences of structure variables $\log P$, $\log T$, $\log R$, and $\log L$ between the last two converged model

all fall below a predetermined limit (in the present models 0.001), declare the equilibrium/potential iterations converged and proceed to step (8)

(6) Compute the total potential (see § 2.1) for the current equilibrium structure and the corresponding equipotential surface geometry factors ξ_P, ξ_T, which characterize the potential for the next equilibrium step

(7) Go to step (4) to compute an updated equilibrium structure

(8) Check consistency of outer boundary condition with internal structure; if inconsistent (model envelope parameters do not fall within current triangle) recompute surface boundary conditions and return to step (4) to begin a new set of equilibrium/potential iterations

(9) Once the converged internal structure is consistent with the surface boundary condition, determine the magnitude of the next timestep Δt based on rates of change of various model parameters

(10) Determine rotational outer boundary condition by comparing current outer layer velocity to its critical velocity $v_{\rm crit}$

(11) Accrete mass and associated angular momentum through time step Δt

(12) Update nuclear abundances by solving the nuclear reaction network through time step Δt

(13) Perform angular momentum transport and nuclear species mixing through time step Δt

(14) Compare velocities in the outer layers of the model with the critical velocities in these layers; layers with velocities exceeding critical are assumed to be spun off and are removed from the model

(15) Continue evolutionary sequence with next time step (i.e. return to step (1))

Chapter 3

Angular momentum transport

In the present chapter we survey some aspects of the physics of fluid instabilities in differentially rotating stars. In § 3.1 we review the hydrodynamic instabilities which are of primary importance for the transport of angular momentum in our models. § 3.2 briefly examines some of the instabilities that we neglect in the present work. Physical mechanisms for the generation of gravity waves on the core-envelope interface of a rotating star are considered in § 3.3 and § 3.4. This interface is similar in many respects to geophysical wind-wave systems, and so the terrestrial problem of the wind generation of water waves is briefly reviewed in this section, and extensions to the astrophysical case are considered.

3.1 Hydrodynamic instabilities

3.1.1 Brünt-Väisälä frequency

The buoyancy or Brünt-Väisälä frequency, N, is given by

$$N^2 = \frac{g}{\rho}\left(\frac{d\rho_e}{d\varpi} - \frac{d\rho}{d\varpi}\right) \tag{3.1}$$

where ρ is the ambient medium density, ρ_e the density of the displaced fluid element, g the local gravitational acceleration, and ϖ the coordinate in the direction of stratification (taken to be perpendicular to the rotation axis, since we evaluate stability to shear in the equatorial plane of the model). Expressing the equation of state in the form

$$d\log\rho = \alpha\, d\log P - \delta\, d\log T + \varphi\, d\log\mu$$

and substituting into Eq. (3.1), the two density gradients are seen to share a common term in $d\log P/d\varpi$ (the displaced element is assumed to maintain pressure equilibrium with its surroundings) and only the ambient density gradient contributes a term in $d\log\mu/d\varpi$ since the displaced element is assumed to maintain its composition. Assuming that the element is displaced adiabatically, the expression for N becomes

$$\begin{aligned} N^2 &= g\left[\delta\left(\frac{d\log T}{d\varpi} - \frac{d\log T_e}{d\varpi}\right) - \varphi\frac{d\log\mu}{d\varpi}\right] \\ &= \frac{g}{H_p}\delta\left(\nabla_{\rm ad} - \nabla + \frac{\varphi}{\delta}\nabla_\mu\right) \\ &= N_T^2 + N_\mu^2 \end{aligned}$$

where N_T, N_μ are the thermal and compositional components of the buoyancy frequency,

$$\begin{aligned} N_T^2 &= \frac{g}{H_p}\delta(\nabla_{\rm ad} - \nabla) \\ N_\mu^2 &= \frac{g}{H_p}\varphi\nabla_\mu\,. \end{aligned}$$

$H_{\rm P} = -dr/d\log P$ is the density scale height, $\nabla = (d\log T/d\log P)$ is the temperature gradient of the ambient medium, $\nabla_{\rm ad} = (d\log T/d\log P)_s$ is the adiabatic temperature gradient, and $\nabla_\mu = (d\log\mu/d\log P)$ is the mean molecular weight gradient in the ambient medium.

3.1.2 Convective instability

Convection is the most vigorous dynamical instability that we consider in the context of our models. A zone is taken to be convectively unstable when the thermal part of the Brünt-Väisälä frequency becomes imaginary there; i.e. $N_T^2 < 0$. This reduces to the usual Schwarzschild criterion for convective instability, (Cox & Giuli 1968) $\nabla_{\rm ad} < \nabla$. We assume regions which are convectively unstable are brought into a state of solid body rotation, $\Omega = $ constant, on a dynamical time scale.

3.1.3 Adiabatic shear instability

The stability of a shear flow in a stratified medium is enhanced by a strong buoyant restoring force – characterized by the intrinsic buoyant or Brünt-Väisälä frequency N – and weakened by the more ready availability of kinetic energy from the flow, characterized by the rate of change of the strain component $\dot{\epsilon}_{ij}$ for shear in the j direction across a plane perpendicular to i. The competition between these two factors is embodied in the Richardson number, which is defined as

$$R_{\mathrm{i}} = \frac{N^2}{\left(d\Omega/d\log\varpi\right)^2}$$

where $\varpi = r\sin\theta$ is the distance to the rotation axis. The shearing medium is taken to be stable when $R_{\mathrm{i}} > R_{\mathrm{i,c}} = 1/4$ – the Richardson criterion for the stability of adiabatic shear flow. When this criterion is violated, the kinetic energy contained in the shear flow has reached a level sufficient to overcome the stabilizing influence of the stratification and turbulence is expected to ensue. The resulting turbulent eddy viscosity redistributes momentum on a dynamical time scale, rapidly bringing the affected region into a state of marginal stability ($R_{\mathrm{i}} = 1/4$ throughout the region).

We assume that a radiatively stable zone becomes unstable to adiabatic or dynamical shear when the marginal condition $R_{\mathrm{i}} = R_{\mathrm{i,c}} = 1/4$ is achieved (Chandrasekhar 1961; Zahn 1974; Maeder & Meynet 1996). In practice, we invert this condition for the critical value of the gradient of angular velocity in terms of the Brünt-Väisälä frequency

$$\left(\frac{d\Omega}{d\log\varpi}\right)^2_{\mathrm{c,dyn}} = \frac{1}{R_{\mathrm{i,c}}}\left(N_T^2 + N_\mu^2\right) . \tag{3.2}$$

In a region subject to dynamical shear instability, the turbulent eddy viscosity take the value $\nu = l^2/\tau_{\mathrm{dyn}}$, where the characteristic length scale $l \sim H_p$.

3.1.4 Nonadiabatic shear instability

Nonadiabatic or "secular" shear instability becomes important when the thermal diffusion time scale is shorter than the momentum diffusion time scale of the fluid flow. The Prandtl number $\mathcal{P}_{\mathrm{r}}$ provides a useful characterization of this limit, and is defined as the ratio of the thermal diffusion time scale to the momentum diffusion time scale:

$$\mathcal{P}_{\rm r} = \frac{c_V(\mu_P + \mu_r)}{\chi}$$

where χ is the thermal conductivity, and the viscosities of plasma and of radiation are given by

$$\mu_P = \frac{2\sqrt{m_H (k_B T)^5}}{5e^4 \log \Lambda} \quad \text{and} \quad \mu_r = \frac{4aT^4}{15c\kappa\rho} \, ,$$

respectively, for a pure hydrogen plasma (see Spitzer 1965; Tassoul 1978), Λ takes the form

$$\Lambda = \frac{3}{2e^3}\left(\frac{m_H k_B^3 T^3}{\pi\rho}\right)^{1/2} \, ,$$

where e is the electron charge, c the velocity of light, k_B Boltzmann's constant, and m_H the proton mass. Neglecting magnetic fields, the thermal conductivity is given by Tassoul (1978) as

$$\chi \sim K = \frac{4acT^3}{3\kappa\rho} \, .$$

The stabilizing influence of buoyancy on a perturbed element of a shear flow is reduced when that element can exchange heat with its surroundings. Following the arguments of Endal & Sofia (1978) and Zahn (1974), the effect of the nonadiabaticity of the element is represented by a multiplicative factor applied to the temperature gradient portion of the Richardson criterion

$$\left(\frac{d\Omega}{d\log\varpi}\right)^2_{c,sec;1} = \frac{\mathcal{P}_{\rm r} R_{\rm e,c}/8}{R_{\rm i,c}} N_T^2 \, .$$

Here the critical Reynolds number $R_{\rm e,c} \sim 2500$. For sufficiently fast heat exchange (very small Prandtl number) virtually any shear in the flow becomes unstable. This is not physically realistic, however, since the molecular weight portion of the criterion should be unaffected by thermal effects. Hence, a second criterion must be met

$$\left(\frac{d\Omega}{d\log\varpi}\right)^2_{c,sec;2} = \frac{1}{R_{\rm i,c}} N_\mu^2 \, .$$

Only when the gradient in Ω is sufficient to exceed both these limits is the flow taken to be secularly unstable.

This instability grows with a characteristic time scale $\tau_{\rm ss} \sim R_{\rm e,c}/|d\Omega/d\log\varpi|$, and the turbulent elements have a characteristic length scale $l_{\rm ss}^2 \sim \nu R_{\rm e,c}/|d\Omega/d\log\varpi|$. The velocity required to compute the associated eddy viscosity is given by

$$v_{\rm ss} = l_{\rm ss}/\tau_{\rm ss} = \left[\frac{\nu(d\Omega/d\log\varpi)}{R_{\rm e,c}}\right]^{1/2} .$$

The eddy diffusivity is given by $D \sim v_{\rm ss} l/3$, where l is taken to be the pressure scale height.

3.1.5 Viscous energy dissipation

The rate at which energy is dissipated by turbulence characterized by kinematic viscosity ν is given by

$$\varepsilon_{\rm d\mathit{iss}} = \frac{\nu}{2}\left(\frac{d\Omega}{d\log\varpi}\right)^2 .$$

This specific energy generation rate is computed for each model during the mixing phase and is added as an additional source of heat to the gravitational energy source term ε_g during the next equilibrium structure calculation. The equation expressing conservation of energy thus becomes

$$\frac{\partial L}{\partial m} = \varepsilon_n + \varepsilon_g + \varepsilon_{\rm d\mathit{iss}} .$$

3.2 Other instabilities affecting stellar interiors

Other instabilities which are commonly considered in the context of stellar evolution include the baroclinic instabilities and Eddington-Sweet currents (also known as meridional circulation). These instabilities are discussed further, below.

Due to their relatively long time scales (thermal and longer, except for adiabatic baroclinic, which our models are stable against), these instabilities are most effective at redistributing angular momentum and mixing nuclear species while the star is on the main sequence. They are all effectively choked off by the increasingly strong molecular weight gradients which develop as the star proceeds into its post main sequence evolution. Subsequent evolutionary phases occur on more rapid time scales, providing less time for these slower instabilities to act. Since the models considered in the present work are assumed to be non-rotating during most, if not all, of their time on the main sequence, shear instabilities, which act on a dynamical or thermal time scale, are expected to dominate.

3.2.1 Solberg-Hoiland criterion

In a baroclinic star with rotation a profile of the form $\Omega(\varpi, z)$, surfaces of constant entropy and constant pressure do not coincide, making this instability possible. Such a rotation law is dynamically stable if (i) entropy never decreases outward; and (ii) $j = \Omega\varpi^2$ increases from the poles to the equator on isentropic surfaces. Since the stars considered in the present work are assumed to be in a state of shellular rotation, and are also assumed to acquire their angular momentum at their surfaces (so that j increases outward), they are stable against the dynamical Solberg-Hoiland instability (see, e.g., Endal & Sofia 1978; Tassoul 1978).

3.2.2 Goldreich-Shubert-Fricke instability

This thermal time scale instability sets in if either $d(\Omega\varpi^2)/d\varpi < 0$ or $d\Omega/dz \neq 0$. Since angular momentum is injected at the surface of our stars, the first part of this criterion is satisfied. In chemically homogeneous regions of our models, we expect the secular instability that arises according to these criteria will be overwhelmed by shear instabilities.

3.2.3 Eddington-Sweet currents

These currents will be supressed by the gradients in mean molecular weight which develop during the main sequence evolution of the supernova progenitor. Weiss et al. (1988) have considered the possible role of Eddington-Sweet currents in the origin of abundance anomalies in SN 1987A. They concluded that, if the outer layers of the progenitor rotated very rapidly, such currents could have contributed to the nitrogen anomaly. Despite this caveat, it is unlikely that Eddington-Sweet currents will play an important role in the evolution of our stars, especially as their inhomogeneities increase as they leave the main sequence.

3.3 Surface gravity wave generation at the core-envelope interface

The accretion models presented in the present work all have rapidly rotating envelopes as a result of the large amount of angular momentum they acquire along with mass from their companions. The non-rotating cores of these models are separated from their rotating envelopes by a density gradient of varying strength, depending on the age of the star. This stratification at the core-envelope boundary slowly increases as the star evolves through the main sequence, becoming much more pronounced once the star begins burning hydrogen in a shell (see Chapter 4). The accreted angular momentum is rapidly redistributed in the envelope by a combination of shear instability induced turbulence and convection, mechanisms which are efficient there due to the lack of significantly inhibiting density stratifications. Once the wave of angular momentum reaches the edge of the core, however, further transport inward is hindered by the steep density/molecular weight gradient which characterizes this region of the star. The large buoyancy frequency at this interface stabilizes turbulence there for all but the most extreme levels of shear.

As shown in Chapter 4, stars which accrete mass and angular momentum while still on the main sequence (late main sequence accretion scenario) can achieve enough shear at the core-envelope interface to surmount the still-moderate stratification there. The resulting turbulence is effective in transporting angular momentum into the cores of these stars.

This, however, is not the case for stars which accrete their angular momentum after a hydrogen burning shell has ignited at the interface (early post main sequence scenario). The shell burns outward in mass, consuming hydrogen from the envelope, leaving heavier helium ashes in its wake, and steepening the density gradient as a result. Shortly after shell burning commences, μ, the mean molecular weight, and hence the density both become discontinuous, developing a step at the core-envelope interface due to the continued operation of the outward burning shell. The shear between envelope and core in this case is not large enough to overcome the resulting stratification. The star at this stage consists of a dense non-rotating core surrounded by a less dense and rapidly rotating envelope, with a compositional discontinuity separating the two.

The resulting configuration is suggestive of another situation involving the relative motion of two fluids of differing densities, separated by a compositional discontinuity: wind blowing over water in a terrestrial context. The rotating stellar envelope comprises the wind in this case, and the core is analogous to the stationary water over which it blows, the two media being separated by a surface across which the molecular weight changes discontinuously. A star is gaseous throughout compared to the air-water case (in which the state of matter changes from liquid to gas across the interface), and thus there is no surface tension contributing to the restoring force which acts on the surface of the stellar core. Otherwise, the essential physics of the two cases is similar. Hence, the geophysical fluid dynamics of the air-water interface, its stability when in a state of shear, and particularly, the transport of energy and momentum across it, may shed some light on the stellar case of interest to us here.

We therefore examine in the present section the stability of a fluid interface in the presence of shear. These results were originally motivated by the study of air-water interfaces, but are equally applicable to the core-envelope interfaces of massive, differentially rotating stars.

3.3.1 Stability of shear across a fluid interface

It is well known to even a casual observer of an ocean, a lake, or the Charles river for that matter, that on a windy day a sufficiently strong gust of air blowing over the water surface can rapidly give rise to waves of various amplitudes and wavelengths. That is, during the course of their interactions, both energy and momentum are transmitted from the wind to surface water waves.

The wind generation of water waves is a particular case of the general problem of the stability of fluid interfaces in the presence of shear, the prototype being the classical Kelvin-Helmholtz instability. We briefly review the Kelvin-Helmholtz instability for a simple two fluid system with discontinuous density and shear velocity distributions in § 3.3.2. In § 3.3.3 we consider another fluid interface instability, resonant or critical layer instability, which provides an explanation of water-wave generation by winds in the terrestrial context, and which is likely to be more important in the stellar context than Kelvin-Helmholtz type instabilities for transporting angular momentum across the core boundary.

3.3.2 Kelvin-Helmholtz instability

Consider a system in which a fluid of density ρ_1, moving with uniform velocity U_1 (i.e. $U = U(y) = U_1$ where y is the coordinate perpendicular to the interface) overlies a second fluid of density $\rho_2 > \rho_1$ and uniform velocity U_2. The velocities are assumed to be parallel and directed along the interface between the two fluids. Linearizing the equations of motion and assuming that all perturbative quantities have the dependence $e^{ik(x-ct)}$ yields the dispersion relation for waves on the interface,

$$c = \frac{\rho_1 U_1 + \rho_2 U_2}{\rho_1 + \rho_2} \pm \left[\frac{g}{k} \frac{\rho_2 - \rho_1}{\rho_1 + \rho_2} + \frac{kT_1}{\rho_1 + \rho_2} - \frac{\rho_1 \rho_2}{(\rho_1 + \rho_2)^2} (U_1 - U_2)^2 \right]^{1/2} \tag{3.3}$$

where T_1 is the surface tension at the water-air interface, g is the local acceleration of gravity, and $k = 2\pi/\lambda$ is the wavenumber of the interfacial wave.[1] The phase speed c acquires an imaginary component and consequently the growth rate of the wave becomes positive for wavenumbers k such that

$$\frac{g}{k} + \frac{kT_1}{\rho_2 - \rho_1} < \frac{\rho_1 \rho_2}{\rho_2^2 - \rho_1^2} (U_1 - U_2)^2 \tag{3.4}$$

For the particular case of a very light fluid over a heavier one (such as air over water) $\rho_1 \ll \rho_2$ and we can rewrite the instability condition Eq. (3.4) in the more physically illuminating form

$$(\rho_2 g + T_1 k^2) \eta_0(x,t) < \rho_1 k (U_1 - U_2)^2 \eta_0(x,t) \,. \tag{3.5}$$

The left hand side of Eq. (3.5) gives the restoring force per unit area due to the combined action of gravity and surface tension for a surface displacement $\eta_0(x,t)$ (x is the coordinate along the interface in the direction of the winds), while the right hand side expresses the aerodynamic presure (or suction in this case) $P_a = \rho_a k U^2 \eta_0$. Instability occurs when the suction overcomes the stabilizing influence of the gravity and surface tension (the latter becoming increasingly important for increasing wavenum-

---

[1] Note that $g/k = c_0^2$, the phase speed of deep water waves with wavenumber k.

ber or smaller wavelength). The development of a Kelvin-Helmholtz instability can analogously be seen by considering the flow lines of the fluid around the perturbed interface: along the crests the flow lines are compressed, the flow is faster, and hence the pressure is reduced according to Bernoulli's theorem. The converse is true above the troughs of the waveform, where the flow slows and hence the pressure is increased. The interface becomes unstable when the restoring force is finally overcome by these pressure perturbations.

The instability condition Eq. (3.4) with $T_1 = 0$ implies that, for a given shear strength $|U_2 - U_1|$ only waves with wavenumber k large enough ($k > k_{min}$), or equivalently wavelength small enough, will be unstable. Note also another hallmark of the pure Kelvin-Helmholtz instability: the destabilizing pressure fluctuations are in perfect antiphase with the surface elevation of the wave (low pressure over crests and high over troughs). In this respect the action of the pressure fluctuations is analogous to forcing a swing by pushing it at the ends of its motion. The forcing in this case case in quadrature with the surface velocity, hence no momentum is transferred from the wind to the water in this case. As we will see, these properties are in contrast to the second variety of fluid interface instabilities considered herein, critical or resonant layer instability.

3.3.3 Critical layer instability

Eq. (3.4) predicts a minimum shear velocity $|U_2 - U_1|$ for instability of the air-water interface of 660 cm s^{-1}, which corresponds to waves of wavelength 1.73 cm. Terrestrial observations, however, indicate that waves are actually generated on the water at much lower wind speeds than this, a fact that gave rise in the late 1950's to work which generalized and extended the class of fluid interface instabilities. The theory developed by Miles (Miles 1957, 1959a,b) and Howard (Howard 1961) introduced the concept of a "critical layer" which is located in the shear flow above the interface and which resonantly interacts with the interfacial wave below, transferring energy and momentum from the air flow to the surface wave. The form of the vertical wind profile is crucial for the existence of the instability: Miles assumed the profile took a form derived from turbulent boundary layer theory

$$U(y) = U_0 + U_1 \log\left(1 + \frac{x}{\delta}\right) \tag{3.6}$$

for $y > 0$ and where U_0 is the velocity jump across the interface (associated with the Kelvin-Helmholtz mode of instability) and δ is a scale length of the shear flow.[2] A wave propagating along the interface with wavenumber k and phase speed $c^2 = g/k$ (appropriate for a "deep water wave" on the surface of the ocean) will have an associated critical layer in the shear flow at the level $y = y_{\mathrm{cr}}$ such that the speed of flow at this level equals the speed of the wave: $U(y_{\mathrm{cr}}) = c$. When such a layer exists (depending on the range of speeds represented in the shear flow) a resonant interaction between the surface wave and the critical layer will ensue only if $U''(y_{\mathrm{cr}}) < 0$ (see Lighthill 1962, for further details). Note that this condition is always satisfied for the shear profile Eq. (3.6).

Relative to the critical layer, fluid particles in the shear circulate in a pattern which results in a secondary pressure pertubation acting on the surface in-phase with its rate of sinking, $-\partial\eta_0(x,t)/\partial t$, or equivalently $\pi/2$ out of phase with the surface elevation (i.e., maximum pressure forces occur at nodes of the displacement of the surface wave). See Fig. 3-1 for a schematic representation of this motion. This form of forcing, since it is in-phase with the velocity of the surface, transfers energy and momentum from the critical layer to the surface wave. In terms of the analogy presented in the previous section, it is akin to driving the motion of a swing by pushing it at the point of maximum velocity rather than maximum displacement, as in the case of the pure Kelvin-Helmholtz instability.

It is important to note that, in contrast to the Kelvin-Helmholtz instability, a surface wave of phase speed c will find a critical layer with which to resonate as long as the shear flow contains a level with matching speed c. The idealized shear profile Eq. (3.6), with $U_0 = 0$ contains levels with flow speeds from 0 to ∞, so a wave of any wavenumber is amplified by a shear flow of this form. In contrast, there are no waves subject to pure Kelvin-Helmholtz instability for such a profile, since there is no discontinuity in velocity across the interface ($U_0 = 0$). More generally, for a profile

---

[2] Note that, in contrast to the Kelvin-Helmholtz instability considered in § 3.3.2, the flow in this case is *not* constant with altitude above the interface.

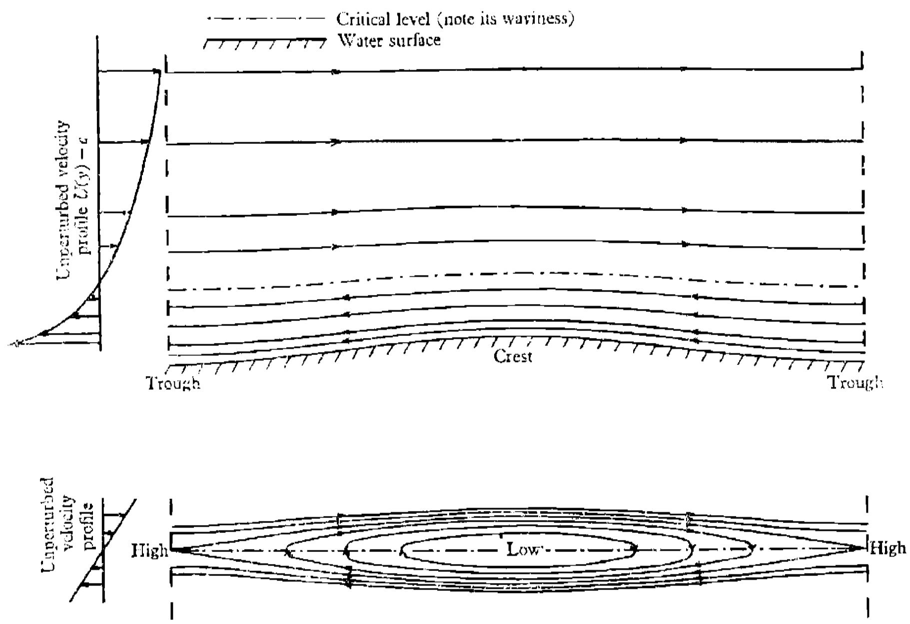

Figure 3-1: Top: Sheared airflow relative to a travelling surface wave. The motion of the surface wave creates undulations in the shear flow above it which diminish in magnitude with height. The critical layer is indicated by the dash-dotted line. Bottom: Streamlines about the critical layer, created by the action of a sinusoidally varying pressure gradient in the shear flow (from Lighthill 1962).

with $U_0 > 0$ and a finite upper cutoff there is a range of wavenumbers $k_1 < k < k_2$ which are stable, while waves with $k > k_2$ are Kelvin-Helmholtz unstable, and those with $k < k_1$ have critical layers (Alexakis et al. 2002).[3]

3.3.4 Application to the core-envelope interface

The instability conditions above all follow from linearized equations of motion. As an instability develops and the perturbation quantities increase in magnitude, the omitted nonlinear terms quickly become important, requiring that the further development of the instability be followed in the nonlinear regime. Effects such as wave breaking, wave-wave interactions, etc. become possible, and can result in the exten-

---

[3] These authors have extended the original wave generation theory of Miles et al. to cases of general astrophysical interest, motivated by the problem mixing at the surface of an accreting carbon-oxygen white dwarf (Rosner et al. 1997). Their work combines both the Kelvin-Helmholtz and critical layer instabilities, and derives growth rates over an extended parameter space (the range of density ratios, several shear profiles, compressible/incompressible flow, and surface tension).

sive redistribution of energy and momentum in the affected flows. Such mechanisms and their effects are subjects of extensive study in the geophysical literature.

The interfacial (surface) gravity waves considered in the previous sections will readily couple via such nonlinear interactions to internal gravity waves, which, in turn, will propagate in the radiatively stable, stratified portion of the underlying core (see the following section). These internally propagating waves will induce the transport of momentum from the surface gravity waves to which they are coupled, into the core, where the waves will eventually dissipate and the momentum will be deposited. Alternatively, mechanisms for the direct generation of internal gravity waves are considered in the following section. Regardless of their mode of generation, however, we expect that such internally propagating waves play an important role in the transport of angular momentum into the cores of our accretion models.

3.4 Internal gravity wave generation at the core-envelope interface

An intriguing alternative mechanism for transporting angular momentum across the core-envelope boundary is via Reynolds stresses associated with propagating internal[4] gravity waves (IGWs). IGWs are a ubiquitous phenomenon in gravitationally stratified fluids such as the Earth's atmosphere and oceans; they can induce the transport of significant amounts of momentum between regions where they are excited and regions where they eventually dissipate. In a geophysical context, important atmospheric sources of IGWs include wind flow over surface topography, or alternatively, over the plumes arising from convectively unstable regions. The fluxes of momentum induced by IGWs generated by such mechanisms in the terrestrial atmosphere are responsible, for example, for the so-called "quasi-biennial oscillations," which occur in tropical stratospheric shear zones.

Angular momentum transport induced by IGWs generated at the interface between the convective and radiative regions of the Sun has recently been invoked as

---

[4] Internal gravity waves are buoyancy waves which propagate through stably stratified regions; this should be contrasted with the case of surface gravity waves (such as the water waves considered above), which only propagate along the interface between two regions of differing densities.

a possible mechanism for the spindown of the solar core (Zahn et al. 1997; Kumar et al. 1999). Helioseismological measurements indicate that the core of the Sun is in a state of roughly solid body rotation at an angular velocity intermediate between the angular velocities of the surrounding convection zone's equatorial and polar regions. Kumar et al. (1999) argue that IGWs generated by the solar convection zone can transport enough angular momentum to spin down, on a time scale of roughly 10^7 years, the originally more rapidly rotating solar core, bringing it into approximate corotation with the convective envelope (which itself is continually being spun down by angular momentum loss to the solar wind). This model for the spin-down of the Sun's core assumes the IGWs are generated and propagate isotropically into the radiative interior; hence they carry no net angular momentum. If they remain trapped in the "waveguide" formed by the region of positive Brünt-Väisälä frequency (i.e. within the radiative core), in the absence of any other mechanisms of angular momentum transport their overall effect would be to only redistribute the preexisting angular momentum of the core. In fact, the sign of the angular momentum carried by propagating IGWs is such that shear flows are intensified (see, e.g., Ringot 1998).[5] The instabilities that eventually arise in these strong shear flows provide a natural mechanism for the transport of angular momentum out of the affected regions. This is the mechanism at work in the QBO, and has been posited by Kumar et al. (1999) to also be operative in the solar tachocline at the edge of the radiative core.

In contrast to the physical situation outlined in the previous paragraph, IGWs directly generated via shear flow over topography – whether it takes the form of mountain ranges or alternatively, the time-varying corrugations at the border of a convectively unstable zone – will have a spectrum which is anisotropic with respect to the direction of propagation (Fritts et al. 1998). Such a spectrum of waves can induce the transport of a non-zero amount of angular momentum into the region in which they propagate. Assuming that the IGWs are ultimately trapped in the stably stratified core of the star, they will eventually dissipate there, depositing their associated angular momentum and changing the state of the core's spin.

---

[5] Both Zahn et al. (1997) and Kumar et al. (1999) used the incorrect sign for the angular momentum transported by prograde and retrograde IGWs propagating into the solar core, as pointed out by Ringot (1998) and Gough (1997), and thus concluded that the ensuing momentum redistribution would reduce shears rather than intensify them.

3.5 Effective viscosity for IGW transport

The instabilities which give rise to the surface gravity waves discussed in previous sections are expected to become nonlinear within a time of order the inverse of their characteristic growth rates (Alexakis et al. 2002). Over an interval of time comprising many such characteristic growth times, it is expected that a steady-state will become established, much as a strong, steady and continuous wind over the surface of an ocean gives rise to a so-called fully developed sea, with a corresponding spectrum of oceanic surface waves. In such a steady-state situation, the average rate of momentum transfer from wind to wave is parameterized by the drag-coefficient C_D, such that the stress on the ocean surface is given by $\tau = \rho_a C_D W^2$, where ρ_a is the air density and W is its (average) velocity. Analogously, we expect that a steady state wave spectrum will eventually be established on the surface of the core due to its interactions with the rotating envelope. The angular momentum associated with steady state envelope drag will then be further transported into the interior of the core via the action of IGWs, which nonlinearly couple to this spectrum of interfacial waves. Alternatively, IGWs in the stratified portion of the core may be generated directly, by mechanisms similar to those considered in § 3.4.

For the purposes of the present calculation, a constant eddy viscosity ν at the core-envelope interface is determined, such that the angular momentum flux across the interface, integrated over the helium burning lifetime of the star, is sufficient to bring the core into solid body corotation with the inner edge of the envelope. If the core is assumed to have constant mass M_c, moment of inertia I_c and a final angular velocity of $\Omega_{\rm cf}$, then the typical average angular momentum luminosity into the core (angular momentum per unit time entering the core) over the core helium burning phase time $T_{\rm He}$ is given by

$$\langle L_{\rm am}\rangle = 2.3\times10^{36}\left(\frac{I_c}{10^{54.6}\,{\rm g\,cm}^2}\right)\left(\frac{\Omega_{\rm cf}}{10^{-4.7}\,{\rm s}^{-1}}\right)\left(\frac{T_{\rm He}}{3.4\times10^{13}{\rm s}}\right)^{-1}\ {\rm erg}.$$

As the angular velocity gradient decreases, the momentum flux decreases as well (see Eq. (2.15)). Since the details of the angular momentum redistribution are not followed for the core, an effective viscosity corresponding to mixing on a dynamical time scale is defined there, in order to maintain the core in solid body rotation throughout the spin-up phase.

Chapter 4

Accretion scenarios

A pair of massive ($M \gtrsim 10\,M_\odot$) stars in a close binary system can significantly interact in several ways:

- The differential gravitational force acting on each member of the system due to the close proximity of the other gives rise to tides in each, which can circularize the orbit of the stars and synchronize their rates of rotation.

- One member of the system can lose mass from its outermost layers, some fraction of which can be transferred to the other member, in the process of critical lobe overflow (CLOF). The large amount of angular momentum carried by the transferred matter can significantly spin up the accreting star. We will consider this possibility in more detail in the present chapter.[1]

- If the accreting star in a CLOF system is unable to accept the additional material in its outer layers sufficiently rapidly, the overflow can evolve into a "common envelope." The stars continue to orbit within this envelope as dynamical friction (Alexander et al. 1976) saps their orbital energy, shrinking the orbit. Depending on the parameters of the system and other physical processes at present poorly understood, the common envelope may be ejected before the

---

[1] In the following, we use the Roche lobe approximation to the critical potential lobe: The critical lobe is well approximated by the Roche lobe when the outer layers of the stars are synchronously rotating, and the stars are sufficiently centrally condensed that they can be considered idealized point masses for purposes of computing the gravitational potential. Tidal interaction will bring the outermost layers of a massive star into synchronous rotation with its orbit on a sufficiently short time scale for this approximation to hold.

stars meet; if not, the two stellar cores are expected to merge within the envelope, leaving a single, modified star. An example of this scenario will be consider in Chapter 5.

We shall not further consider tidal interactions between the components of our binary systems. Goldreich & Nicholson (1989) have shown that the tidal torque exerted by one member of a close binary system on the other is concentrated near the core-envelope boundary, where it excites a train of internal gravity waves (IGWs; see Chapter 3) which transport the negative angular momentum associated with the despinning process of syncronization to the outer layers of the envelope. Here the IGWs radiatively dissipate, and in the process, bring the outermost portions of the envelope into synchronous rotation with the orbit. The spin-up of a massive, main sequence star due to tidal interaction with a companion thus proceeds from the surface of the star, inward. Meanwhile, the core of the star is continually contracting and becoming increasingly dense as it burns its supply of hydrogen fuel during its main sequence evolution. Based on these considerations, we expect that the core of a massive star will be less affected by tidal interaction with a companion than its envelope; for the better part of its main sequence lifetime, the star would have to be in close proximity to its companion in order for tidal interaction to significantly alter its core angular momentum content.

In this chapter we consider, rather, the possibility of Roche-lobe overflow (RLOF) and mass transfer between stars in wider binary orbits. In particular, we examine the evolution of a massive star in a binary system which acquires a significant amount of mass and rotational angular momentum at its surface via accretion from a close companion.

4.1 Critical lobe overflow in close binary systems

Kippenhahn & Weigert (1967) and Lauterborn (1970) introduced a classification scheme for binary star systems undergoing mass transfer based on the physical state of the mass-losing component at the beginning of the transfer phase. In their nomenclature a case A transfer begins during the core hydrogen burning phase of the mass-losing star (i.e. while it is still on the main sequence), while a case B transfer begins after the star has exhausted hydrogen and has not yet begun burning helium in its core, and a case C transfer, after helium burning has terminated in the core of the star and migrated to a surrounding shell. A main sequence star burning nuclear fuel quiescently in its core increases its radius by a moderate amount, on a nuclear evolutionary time scale. When hydrogen burning ceases in the core and migrates to a surrounding shell, the overall structure of the star adjusts to this new configuration of energy generating regions: the core contracts while the envelope[2] expands dramatically and rapidly, on a thermal time scale (see, e.g., Chapter 1 of Stein 1966, for further discussion). This can result in the star expanding beyond its critical potential lobe, initiating a case B or C mass transfer event. Case A transfers are expected to be less common, since a relatively compact main sequence star will only reach and overflow its critical potential lobe when the binary orbital separation (which is proportional to the star's Roche lobe radius, see Eq. (4.3)) is similarly compact.

Throughout this work we denote the initially more massive component of the binary system as the *primary* and the initially less massive as the *secondary*, with masses M_1 and M_2 respectively. Due to its higher mass and hence more rapid rate of evolution, the primary will be the first member of the system to expand enough to fill its Roche lobe and begin transferring mass; the secondary will be the recipient of some fraction of this material. In this chapter we will be concerned exclusively with the evolution of the secondary as it accretes mass lost by the primary. We will not follow the evolution of the primary, treating it simply as a source of material which enters the Roche lobe of the secondary and is accreted at a constant rate over a predetermined interval of time. Our binary systems start with components closely matched in mass (with the primary not more than $1\,M_\odot$ more massive than the secondary in all cases) so that the mass transfer process remains stable (see below). We only consider mass transfers of more than $5\,M_\odot$. Hence the mass ratio of the components is reversed in all cases, and the primary is expected to end is evolution as the less massive component of the system.

As discussed by Podsiadlowski, Joss, & Hsu (1992) (hereafter PJH), the stability of the mass transfer process depends primarily on the relative masses of the components and the thermal states of their envelopes; specifically, whether they are radiative or

---

[2] The layers of the star exterior to the burning shell.

convective (Paczyński & Sienkiwicz 1972). We follow PJH and assume that case A and early case B/C mass transfers (the latter two in which the primary has a radiative envelope) proceed in a generally stable fashion, while late case B/C transfers are expected to be at least quasi-dynamical, and may entail significant losses of mass and angular momentum from the system. Dynamical mass transfer, under certain conditions discussed by PJH, can result in a common-envelope system. We exclude this possibility from the present chapter, but will consider it further in Chapter 5.

We also assume that the Roche lobe of the secondary is spacious enough for a well formed accretion disk to fit inside (to maximize the angular momentum of the transferred mass), as well as to hold the secondary if it expands as a result of the mass gained in its envelope (see, e.g., Hellings 1983; Kippenhahn & Meyer-Hofmeister 1977). This constraint, plus the relative rarity of case A mass transfer systems in general, leads us to conclude that the secondaries considered in the present chapter are most likely to arise as the result of an early case B or C mass transfer episode.

4.1.1 Orbital reaction to mass transfer

How does the transfer of a large amount of matter from the primary to the secondary component of a binary system affect the orbit? We calculate the change (from just before accretion onset to just after it ceases) of the orbital period and the Roche lobe radius of the secondary, for various rates of systemic mass and orbital angular momentum loss. Following Rappaport, Joss, & Webbink (1982) we introduce two parameters, α and β, to characterize the loss of mass and angular momentum from the binary system. β is the fraction of the mass lost by the primary component which is accreted by the secondary. The fraction $1-\beta$ of mass transferred which is lost by the system is assumed to carry with it specific angular momentum $\alpha a^2\Omega_o$ (definition of α) where a is the semi-major axis of the orbit and Ω_o the orbital angular frequency. If it is assumed that the orbit remains circular throughout the mass transfer episode, and that the rotational angular momentum of the component stars and that of any matter being transferred between them is negligible compared to the orbital angular momentum of the system, then the orbital angular momentum evolves as a function

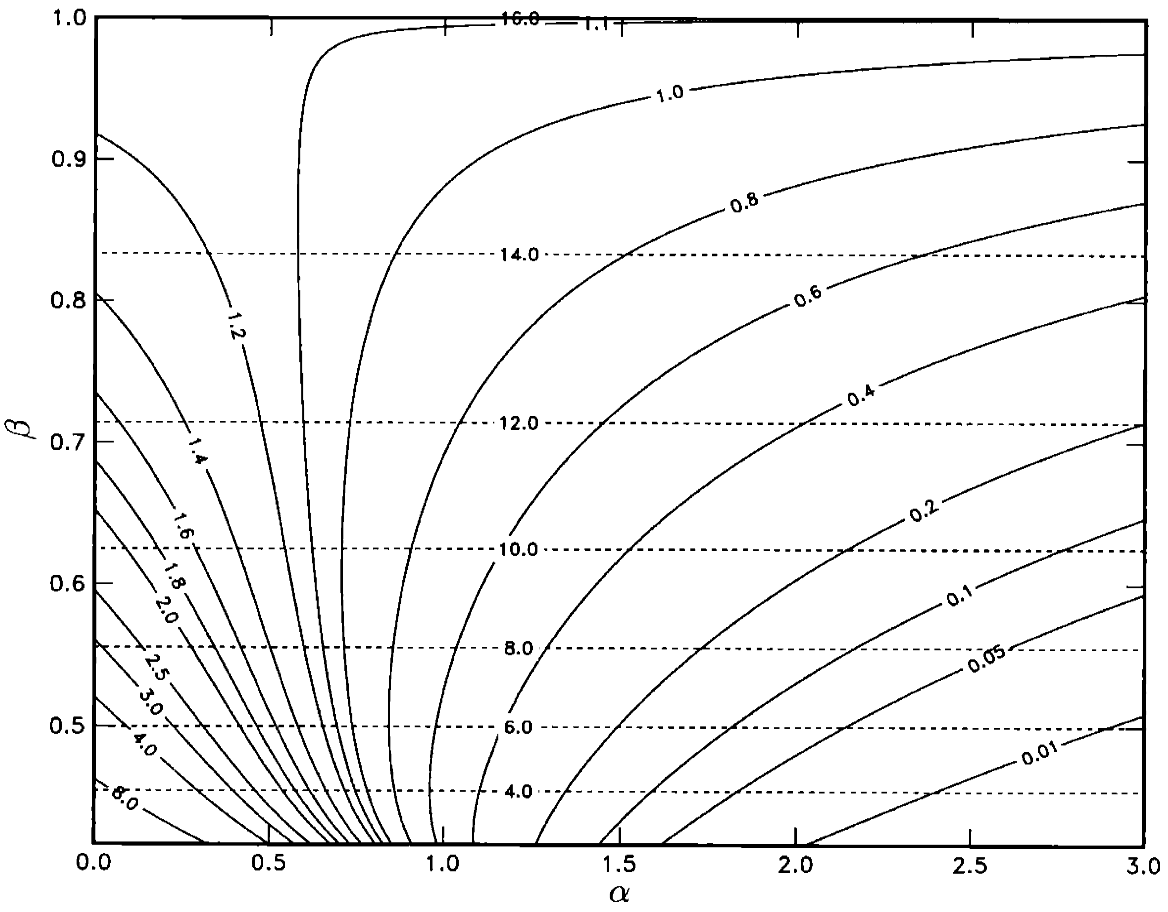

Figure 4-1: Parameter space of mass transfer parameters α and β illustrating the change in Roche lobe radius and mass of the primary (taken to have initial mass $M_{1\mathrm{i}} = 26\,M_{\odot}$) as the result of a RLOF mass transfer episode in which the secondary accretes a total of $10\,M_{\odot}$. Solid contour lines trace levels of constant $R_{\mathrm{L1,f}}/R_{\mathrm{L1,i}}$, where $R_{\mathrm{L1,f}}$ and $R_{\mathrm{L1,i}}$ are the final and initial Roche lobe radii of the primary, respectively. Dashed contours show levels of constant final mass $M_{1\mathrm{f}}$ in solar masses, the final mass of the primary after the mass transfer event. Note that in all cases $\beta(M_{1\mathrm{i}} - M_{1\mathrm{f}}) = 10\,M_{\odot}$ is transferred to the secondary, with the remainder (for $\beta < 1$) assumed lost from the system.

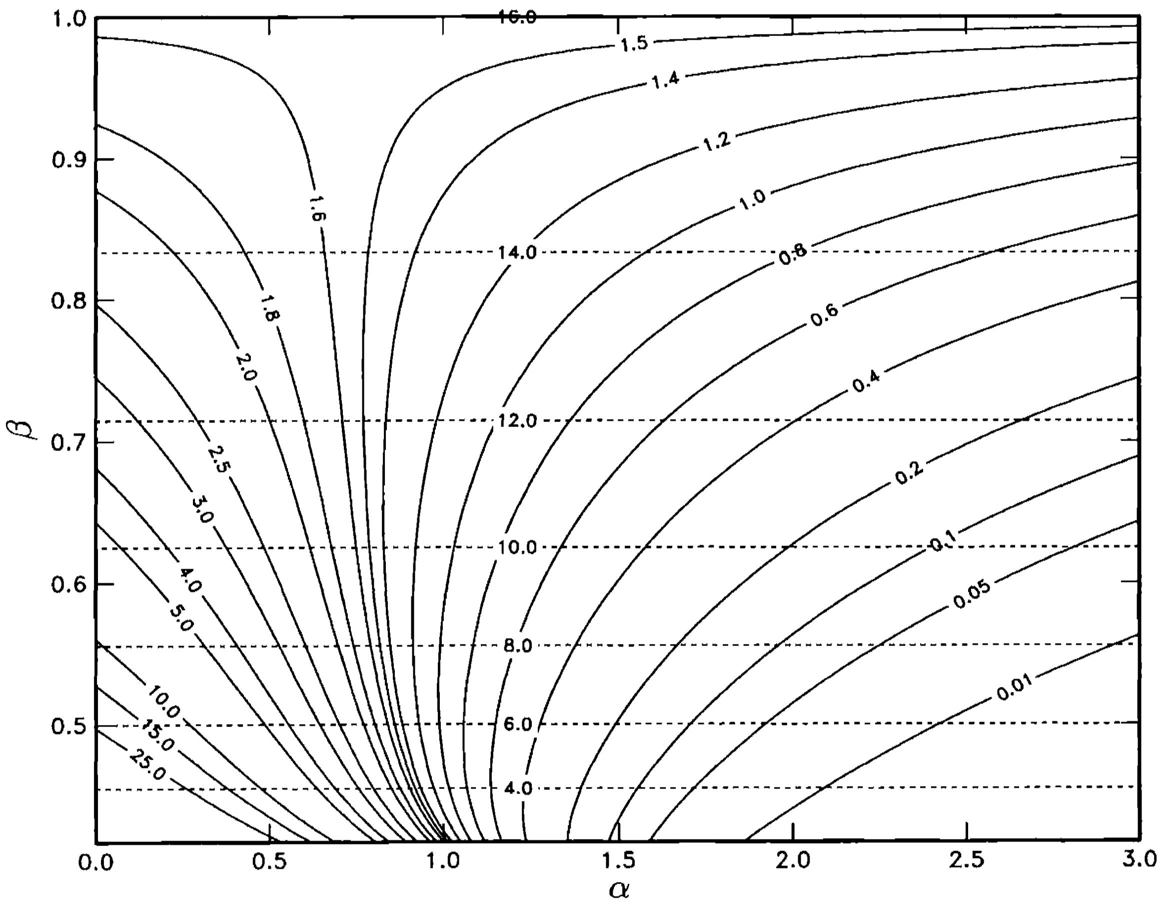

Figure 4-2: Same parameter space as illustrated in Fig. 4-1, with solid contours tracing levels of P_f/P_i, where P_f and P_i are the final and initial orbital periods of the binary, respectively.

of primary mass M_1 according to

$$\frac{dJ}{dM_1} = \alpha(1-\beta)a^2\Omega_o \ . \tag{4.1}$$

The orbital angular momentum J is given in this case by

$$J = \frac{M_1 M_2}{M_1 + M_2} a^2 \Omega_o = M_1 M_2 \sqrt{\frac{Ga}{M_1 + M_2}} \tag{4.2}$$

where the last equality follows from Kepler's second law, $\Omega_o^2 = G(M_1 + M_2)/a^3$.

These equations can be solved for the ratio of final to initial orbital separation a/a_i as a function of M_1 (see PJH, eqn. (5)). We approximate the mean radius of the primary's Roche lobe by

$$\frac{R_{\rm L1}}{a} = \frac{0.49q^{2/3}}{0.6q^{2/3} + \log(1 + q^{1/3})} \ , \tag{4.3}$$

(Eggleton 1983), where $4\pi R_{\rm L1}^3/3$ equals the volume of the Roche lobe and $q = M_1/M_2$.

Fig. 4-1 shows the ratio of final to initial Roche lobe radius and the final primary mass as functions of the parameters α and β. The ratio of orbital periods is shown in Fig. 4-2 for the same parameters. The primary is assumed to have mass $M_{\rm 1i} = 26\, M_\odot$, and the secondary mass $M_{\rm 2i} = 25\, M_\odot$ at the onset of mass transfer, and the secondary is assumed to accrete a total of $10\, M_\odot$ regardless of the value of β (the primary thus loses a total of $(10/\beta)\, M_\odot$ during the transfer event). These values are representative of those which arise in the accretion scenarios considered below. They show that for parameters typical of the conservative or nearly conservative mass transfer expected in stable RLOF ($\alpha \sim 1$ and $\beta \sim 1$), the binary orbit does not suffer a drastic change in size or period. In all cases the primary ends up significantly less massive than the secondary. For $\beta \approx 0.5$ it has lost most of its envelope and remains little more than a bare core.

4.2 Accretion scenarios

The following sections summarize the results of a range of detailed numerical studies of the mass-accreting component of a close binary system which experiences a stable mass transfer phase. We computed the evolutionary sequences described below using the stellar evolution code described in Chapter 2; we included the structural effects of rotation as described in § 2.3.1, and followed the transport of angular momentum and mixing of nuclear species using the procedure of § 2.4 when the instabilities detailed in Chapter 3 are active. We consider two general cases:

- the secondary begins accreting mass late in its main sequence evolution ("Late Main Sequence" or LMS case);
- accretion beginning after the secondary has left the main sequence and begun burning hydrogen in a shell, but before it has traversed the Hertzprung gap ("Early Post Main Sequence" or EPMS case).

These two phases are distinguished for the purposes of angular momentum transport by the strength of the density gradient at the edge of the core. This stratification is still relatively mild while the star remains on the main sequence, but becomes more pronounced during hydrogen shell burning (see Chapter 3). As discussed below, the strength of this gradient significantly influences the transport of angular momentum from the envelope of the star into its core.

In all cases, we also assume that tidal interactions will have synchronized the rotation of both stars with their orbit prior to their arrival on the main sequence (Zahn 1975, 1977). For simplicity, we thus start all models with negligible rotation on the zero age main sequence (ZAMS), and assume that they remain essentially non-rotating until the onset of accretion. The transferred material is assumed in all cases to form an accretion disk around the secondary. Viscosity in the accretion disk carries angular momentum outward, allowing mass to move inward through the disk and toward the equator of the secondary. A mass element that eventually reaches the star's surface is assumed to carry with it specific angular momentum $j_K^2 = GM_2R_{\rm eq,2}$, where $R_{\rm eq,2}$ is the star's equatorial radius. We assume that a falling mass element contributes all its angular momentum to the accreting surface layer, falling lightly onto the surface of the star with negligible vertical (radial) velocity (and therefore inducing no additional pressure term in the equation of hydrostatic equilibrium). We also assume for simplicity that the composition and specific entropy of accreted mass is equal to those of the stellar surface at all times during the mass transfer phase.

Sequence	$M_{\rm initial}$ $(M_\odot)$	$M_{\rm final}$ $(M_\odot)$	$M_{\rm He,c}$ $(M_\odot)$	$M_{\rm env}$ $(M_\odot)$	$R_{\rm final}$ $(R_\odot)$	$\langle j_{16}\rangle_{\rm He,c}$ $({\rm cm^2\,s^{-1}})$
A30p10	26.6	25.2	11.3	13.9	1271	1.39
A40p10	26.6	28.5	11.7	16.8	1616	23.3
A20p10	26.6	15.5	11.2	4.2	1117	0.9
B30p05	26.6	27.4	8.8	18.6	215	0.00
B30p10	26.6	28.3	9.3	19.0	431	0.44
B31p10	26.6	30.0	8.8	21.2	110	0.83
B21p10	26.6	29.1	8.7	20.4	107	0.35
B41p10	26.6	30.1	8.8	21.3	130	0.49
B30p15	26.6	31.9	8.7	23.2	74	0.31

Table 4.1: Parameters for the accretion sequences considered in the present chapter. $M_{\rm initial}$ denotes the initial (ZAMS) mass of the model, $M_{\rm final}$ the final mass at core carbon ignition, $M_{\rm He,c}$ the final mass in the helium core, $M_{\rm env}$ the final mass in the envelope, $R_{\rm final}$ the final radius, and $\langle j_{16}\rangle_{\rm He,c}$ the average specific angular momentum in the He core.

The star is assumed to have ZAMS metallicity $Z = 0.02$. Finally, in order simplify the nuclear processing, and to focus on the angular momentum distribution in the secondary, we have taken the eddy diffusivities D to be zero at all times except in convective zones (i.e. no mixing of nuclear species by processes other than convection).

Table 4.1 summarizes the various accretion scenarios that we computed. The first column contains a sequence identifier which encodes the various parameters characterizing that sequence. Identifiers have the form $CKNpMM$. C is either 'A' or 'B', and denotes the evolutionary stage *of the accretor* when the transfer commences – late main-sequence or early post-main-sequence, respectively. The mass transfer rate is given by $\dot{M} = 10^{-K} M_\odot\,{\rm yr}^{-1}$ (where $K = 2, 3, 4$), $N = 1(0)$ implies that angular momentum transport via non-turbulent processes (gravity-wave mediated) is (is not) operative, and finally, $(NN)\,M_\odot$ is the mass accreted by the secondary during the transfer phase.

4.3 Late main sequence accretion scenarios

We first consider evolutionary sequences in which the primary component of the system begins transferring mass while the secondary is still burning hydrogen in its core, late in its main sequence evolution. In particular, the secondary of sequence $A30p10$ starts its evolution with ZAMS mass $26.2\,M_\odot$ and accretes $10\,M_\odot$ of mass from the primary at a rate of $10^{-3}\,M_\odot\,\mathrm{yr}^{-1}$ (see Table 4.1). The temperature-luminosity evolution of the secondary until the onset of carbon burning in the core is illustrated in the HR diagram of Fig. 4-3. The interior distributions of rotational angular velocity Ω and specific angular momentum j at various points in the evolution are shown in Fig. 4-4, and the moment of inertia I_{enc} and specific entropy s of the model as a function of interior mass are show in Fig. 4-5. Fig. 4-6 summarizes in the form of a "Kippenhahn" diagram the time evolution of the interior structure of the model, including the rotational angular velocity distribution, distribution of convectively unstable zones, zones with significant nuclear burning, and regions of significant mean molecular weight gradient.

In the following sections we discuss the evolution of the secondary of sequence $A30p10$, a LMS accretion case, in greater detail. We consider the secondary's evolution both during and after the accretion event, focusing in particular on the angular momentum acquired by the secondary and how it is tranported from its point of introduction at the surface of the star inward, toward the core. We find that the angular momentum accreted by the secondary of sequence $A30p10$ reaches, penetrates, and spins up the core well before the end of central hydrogen burning. Angular momentum is less successful in penetrating the cores of the EPMS secondaries we computed (see below). This is due primarily to the increasingly stable stratification which develops at the edge of the hydrogen exhausted core as the star ages.[3]

4.3.1 Pre-accretion evolution: $A30p10$

The secondary of sequence $A30p10$ begins its life on the ZAMS with a mass of $26.2\,M_\odot$. In passing through most of its core hydrogen burning phase, it loses $1.2\,M_\odot$ from its envelope to a stellar wind over the course of 5.67 Myr, leaving it with a mass of $25\,M_\odot$ and core hydrogen abundance of $X = 0.04$ at the onset of mass transfer.

---

[3] The degree of stratification in a given zone of the star corresponds to the slope of the specific entropy in the plots presented below; at the onset of hydrogen shell burning, the entropy "step" at the edge of the core visible in these graphs is due primarily to the change in mean molecular weight across this interface.

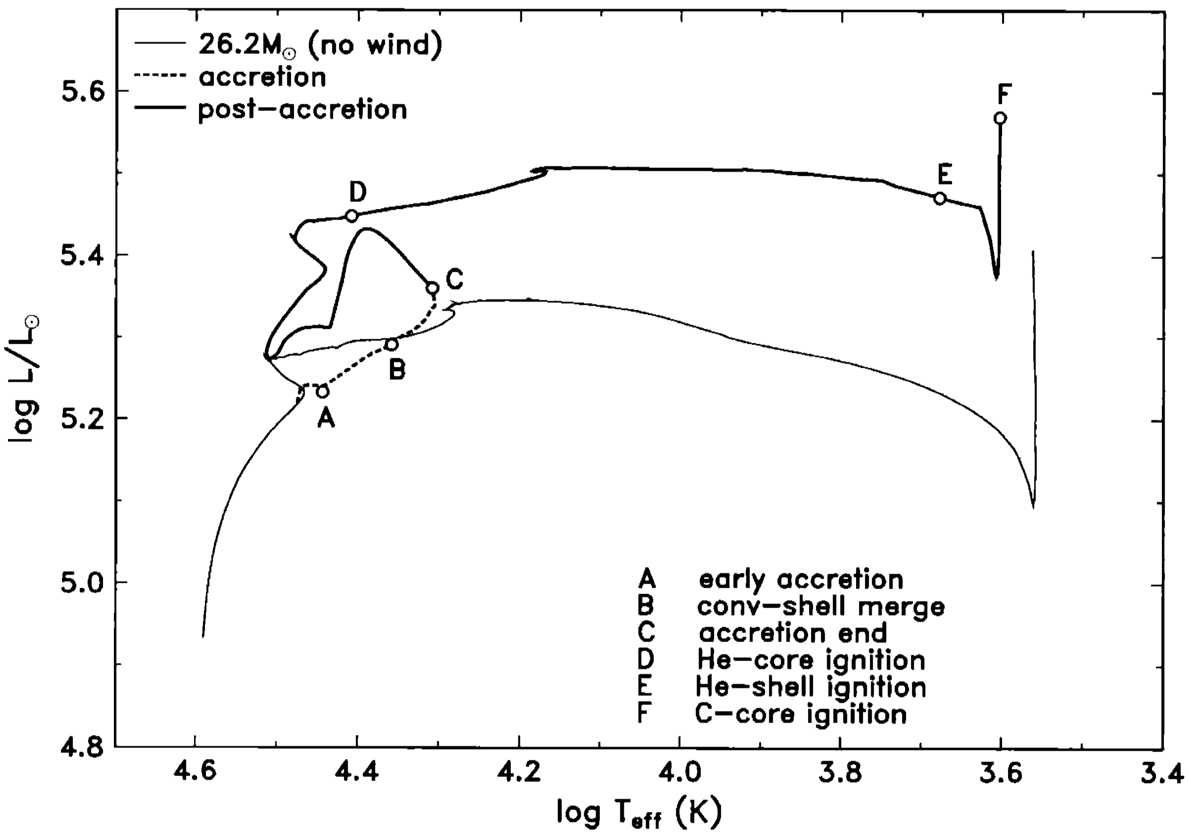

Figure 4-3: HR diagram of the evolutionary sequence *A*30*p*10, an initially nonrotating star with a ZAMS mass 26.2 $M_\odot$, which accretes 10 $M_\odot$ at a rate of 10^{-3} $M_\odot\,\mathrm{yr}^{-1}$ from a close-binary companion near the end of its main-sequence evolution, under the assumption of no angular momentum transport by IGWs. Note that the star has lost $\sim 1.2\,M_\odot$ in a stellar wind during its main-sequence evolution prior to the accretion phase, leading to a stellar mass of 25 and 35 $M_\odot$ just prior to and just following the accretion episode, respectively. The lower, thin solid line shows the post-main-sequence evolution of an isolated, non-rotating 26.2 $M_\odot$ star until core carbon ignition. The dashed and thick solid lines represent evolution during the accretion event (of duration 10^4 years), and following accretion until core carbon ignition (at point F), respectively. Loss due to a rotationally enhanced stellar wind reduces the final stellar mass to $\sim 25\,M_\odot$. Lettered open circles indicate fiducial points in the evolution for which interior variables are plotted in Fig. 4-4 and Fig. 4-5.

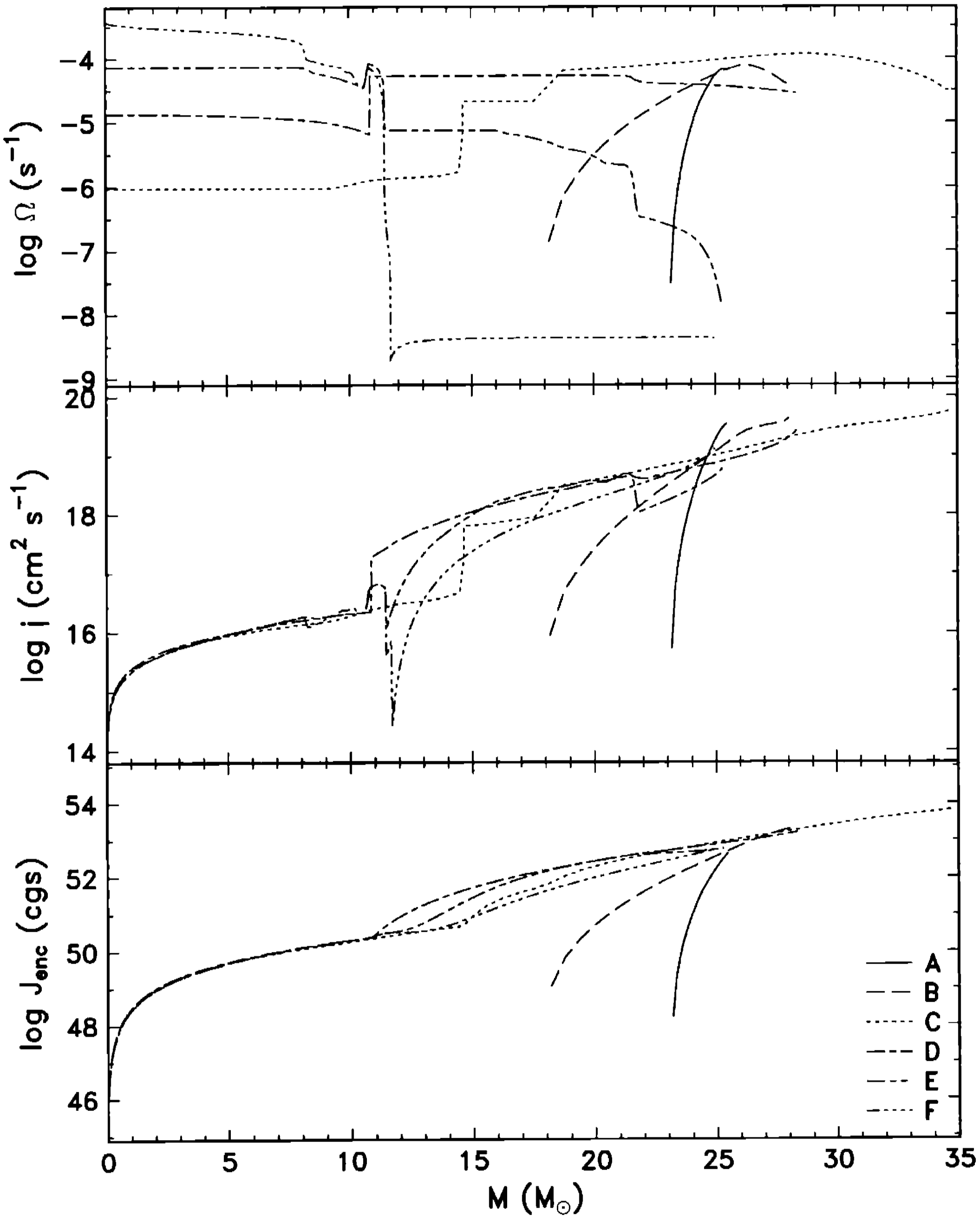

Figure 4-4: Rotational angular velocity Ω, specific angular momentum j, and enclosed angular momentum $J_{\rm enc}$ as functions of enclosed mass for the six time points along the evolutionary track shown in Fig. 4-3, for sequence *A30p10* (late main sequence accretion onset). IGW transport of angular momentum was not included in this calculation and is is not, in fact, necessary for core spin-up, as is evident from curves C - F. Contraction of the core just prior to carbon ignition gives rise to most of the increase in Ω within the core at these late evolutionary stages.

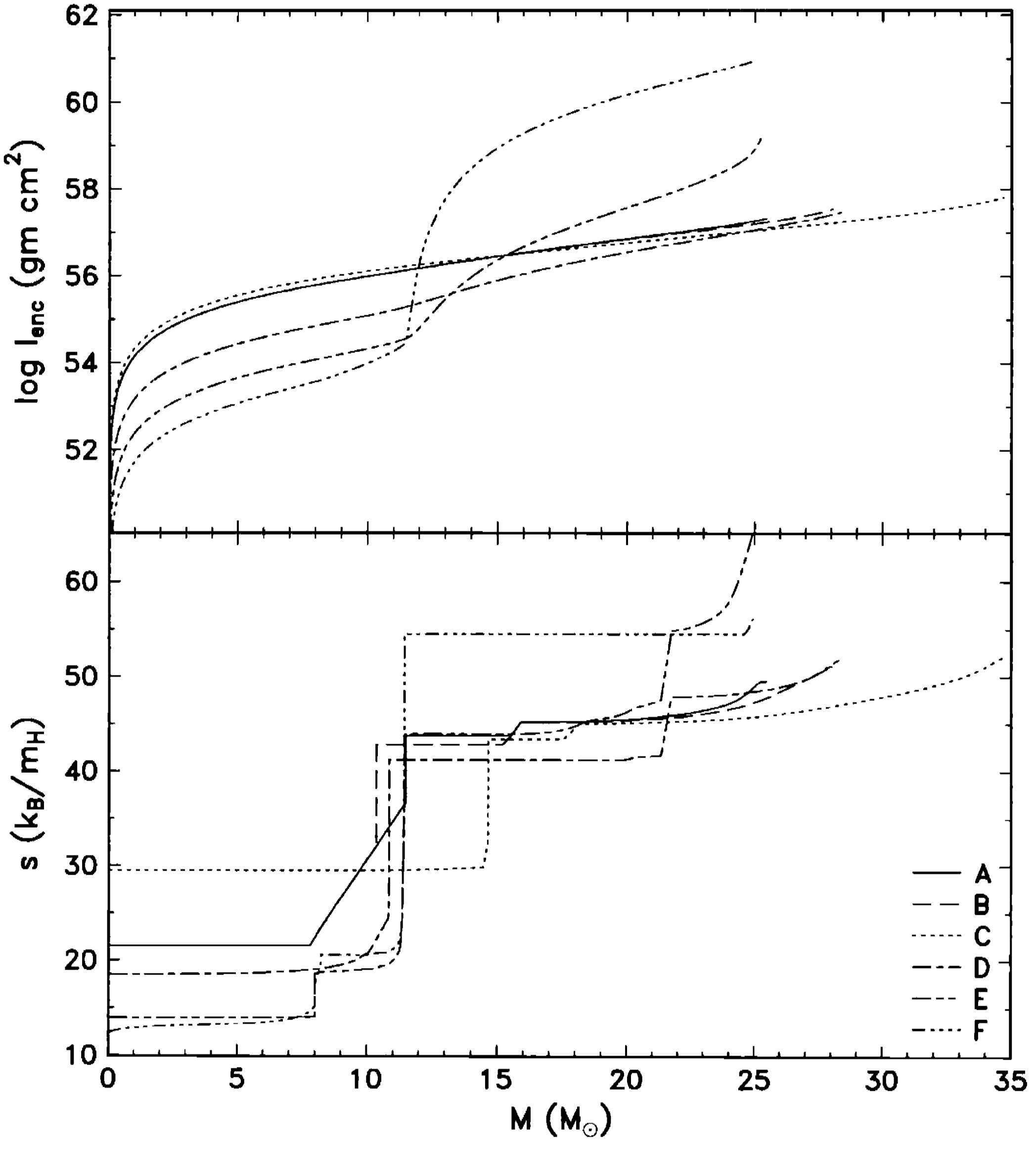

Figure 4-5: Enclosed moment of inertia $I_{\rm enc}$ and specific entropy s as functions of enclosed mass, corresponding to the six time points along the evolutionary track shown in Fig. 4-3, for sequence $A30p10$ (late main sequence accretion onset).

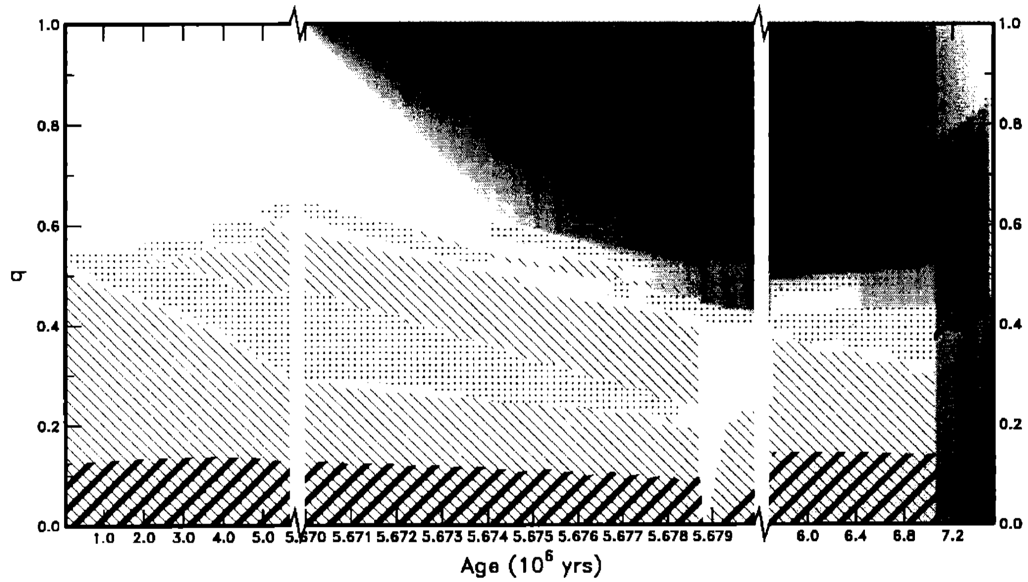

Figure 4-6: "Kippenhahn" diagram for sequence $A30p10$, illustrating the interior evolution of the accreting secondary star. Elapsed time since the ZAMS is shown on the horizontal axis, while the interior structure of the star is shown in the vertical direction, parameterized by the fractional interior mass $q = m/M$. Note that $M = M(t)$, the mass of the star, changes with time due to stellar wind losses and mass accretion. The evolution of the star is divided into three phases, each with a different time scale. The left panel depicts the phase of main sequence hydrogen core-burning, ending at the onset of accretion; the accretion of $10\,M_\odot$ of mass from the primary comprises the center panel (characteristic time scale $\tau_{\rm acc} = M/\dot{M}$), while the remainder of the evolution until the initiation of core carbon burning is shown in the right panel. Shaded gray areas corresponding to various magnitudes of rotational angular velocity Ω. Lightly hatched regions are convectively unstable according to the Schwartzschild criterion, and regions in which the specific nuclear energy generation rate $\varepsilon_{\rm n}$ exceeds $10^4\,{\rm erg\,g^{-1}\,s^{-1}}$ are heavily hatched. Regions with molecular weight gradients $d\log\mu/d\log P > 0.05$ are filled with dots. The variation of the stellar mass with time is most apparent in the "scaling" of the interior structure evident during the accretion phase, after $t \approx 5.570$Myr and interior to $q \approx 0.6$. Just prior to $t \approx 5.571$Myr the core of the star undergoes rejuvenation, which temporarily decreases the rate of hydrogen burning in the core and causes the star to adjust its radius while reaching a new equilibrium. Ω is constant in regions undergoing convective mixing, and regions which are stabilized against shear instability by signficant density gradients (large molecular weight gradients) hinder the inward progress of the accreted angular momentum. In this case, the core is insufficiently shielded by the surrounding density gradient and angular momentum reaches it at $t \approx 5.678$Myr.

4.3.2 Accretion evolution: $A30p10$

Immediately following the onset of accretion, the rotational angular velocity Ω attains a distribution which is marginally unstable to dynamical shear instability (see curve A in the top panel of Fig. 4-4). The rapid differential rotation induced at the surface of the star by the addition of mass carrying large specific angular momentum overwhelms the stabilizing density gradient in the envelope (parameterized by the buoyancy frequency N), and quickly drives down the Richardson number $R_{\rm i}$ of these regions. When $R_{\rm i}$ reaches its critical value of $1/4$, the shear flow becomes turbulent, and the resultant eddy viscosity quickly redistributes angular momentum on a dynamical time scale (Chandrasekhar 1961). The shear flow is maintained in the marginally stable state characterized by $R_{\rm i} = 1/4$ at all points of the unstable region, while angular momentum continues to flow inward, down the gradient in Ω.

The initial stage of the accretion process persists until the accreting surface layer reaches critical rotation and hence loses pressure support, $v_{\rm surf} \sim v_{\rm crit}$.[4] Prior to this point in the evolution, Ω maintains a monotonically decreasing distribution with depth below the star's surface (see curve A in Fig. 4-4). This rotation profile is similar to that derived by Kippenhahn & Thomas (1978) for the distribution of Ω in an accreting white dwarf.[5] At the point A of Fig. 4-3 the secondary has accreted $0.6\,M_\odot$ of material, accelerating its surface to a velocity just below its critical velocity.

During the remainder of the accretion phase, the surface layer continues to rotate at the critical velocity (which is a function of time, due to the changing mass and radius of the star). As mass continues to accrete, it buries the previously deposited layers of material, which settle with their associated angular momentum deeper into the interior of the star. As a result, these layers spin up to larger angular velocities, their change in radius and hence moment of inertia overcoming any diminishment of their original stores of angular momentum by the actions of turbulent transport

---

[4] We constrain $v_{\rm surf}$ to be less than or equal to $0.9 v_{\rm crit}$ at all times, in order that the iterations in our numerical calculations converge; when it reaches this limit the outer boundary condition is changed to fix it at this value (see § 2.4.3).

[5] The two cases differ in how the accreted angular momentum is assumed to redistribute along isobars. Rather than confined to a latitudinal belt at the equator as in Kippenhahn & Thomas (1978), we assume that the accreted mass and angular momentum is redistributed instantaneously (on a dynamical time scale) throughout each mass shell, consistent with our assumption of shellular rotation.

processes (see Fig. 4-7 and Fig. 4-8).

The distribution of Ω in the outmost portion of the envelope at this stage of the evolution decreases outward, and a turnover point (local maximum) develops, linking the outer layers with those interior to them, in which Ω is monotonically *increasing* outward (see curve B in Fig. 4-4). This "no-torque" level, where $d\Omega/dr = 0$, marks a point through which no further angular momentum may pass by viscous tranport. This level persists through the remainder of the accretion phase and into the post-accretion evolution (curve C, Fig. 4-4). Its presence acts to shield the angular momentum content of the layers interior to it from loss through the stellar surface. Meanwhile, angular momentum in layers exterior to the no-torque level is transported down the gradient in Ω to the surface, where it is presumably lost through turbulent viscous coupling to the accretion disk surrounding the secondary.

When $\sim 3.5\,M_\odot$ has been accreted by the secondary in sequence $A30p10$, the inwardly progressing wave of angular momentum impinges upon several regions of more stable stratification, corresponding to gradients in mean molecular weight μ left behind by the retreating hydrogen burning core (see Fig. 4-6). This gradient is steepened at the outer and inner edges of an intermediate convective zone, which homogenizes the composition of the unstable layers. Buildup of angular momentum above the convective region eventually results in enough shear to overcome the stratification at its edge, allowing angular momentum to enter the zone, which is instantaneously brought into solid body rotation by the turbulent convective motions. This creates the step-like configuration in Ω visible, for example, in Fig. 4-4: curves B and C.

At several times during the evolution of model $A30p10$ (as in other models we studied), the inward transport of angular momentum is aided by the presence of a convective zone in a region vacated by the retreating core.[6] In these regions the temperature gradient becomes superadiabatic due to the increased core luminosity required to support the increasingly massive envelope of the star.[7] In the present case, this zone eventually merges inward with the core, increasing the core mass, enriching it in hydrogen, and setting it spinning. This is an example of a so-called "rejuvenation" event in an accreting main sequence star. Hellings (1983) has shown that in many such cases, the accreting star retains no memory of its less massive

---

[6] Convective regions may be most easily identified by flat regions in plot of specific entropy.

[7] The adiabatic gradient is also lessened due to changes in the chemical composition.

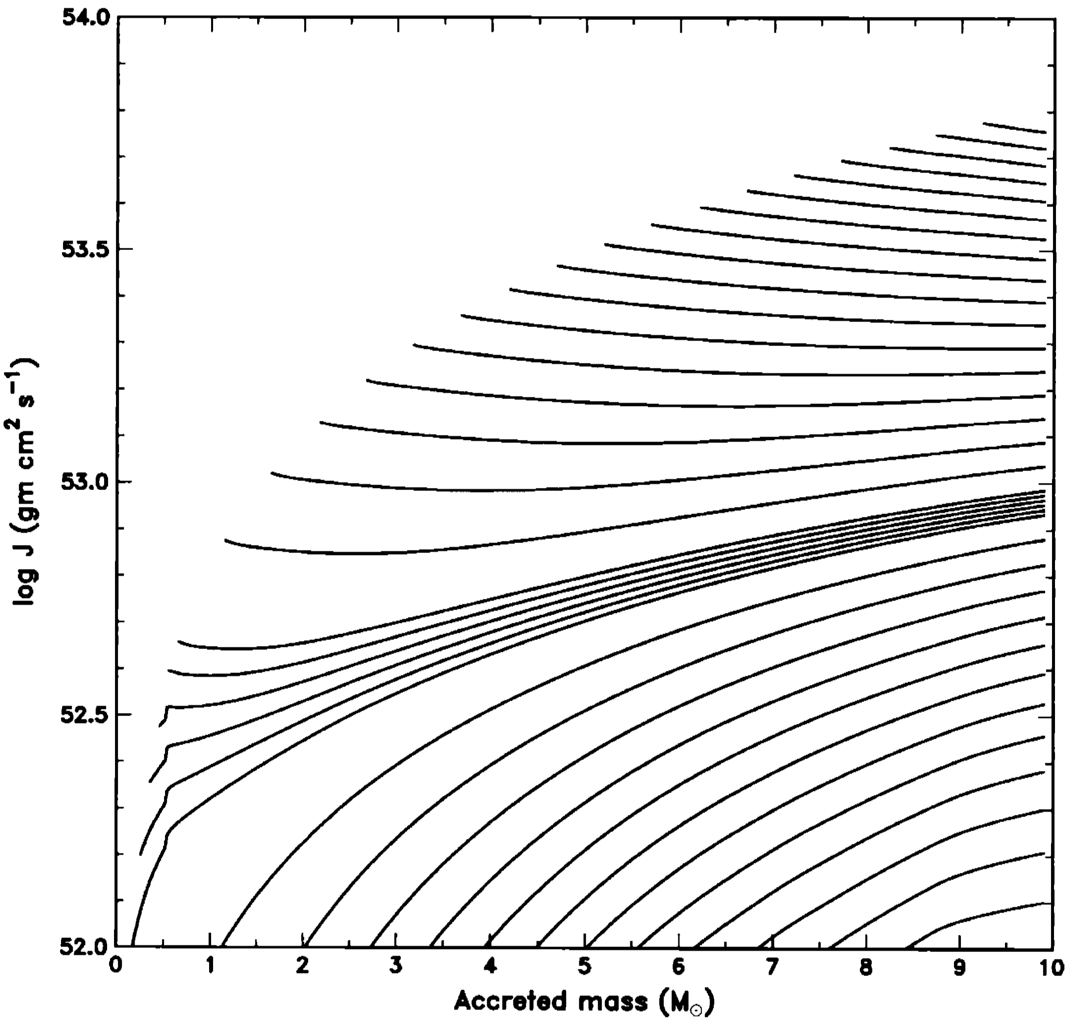

Figure 4-7: The evolution of the angular momentum enclosed by layers of the secondary in sequence *A*30*p*10 over the course of the mass transfer phase. Curves with positive slopes correspond to zones through which net positive angular momentum is being transported inward. Conversely, zones through which net negative angular momentum is flowing have negative slopes.

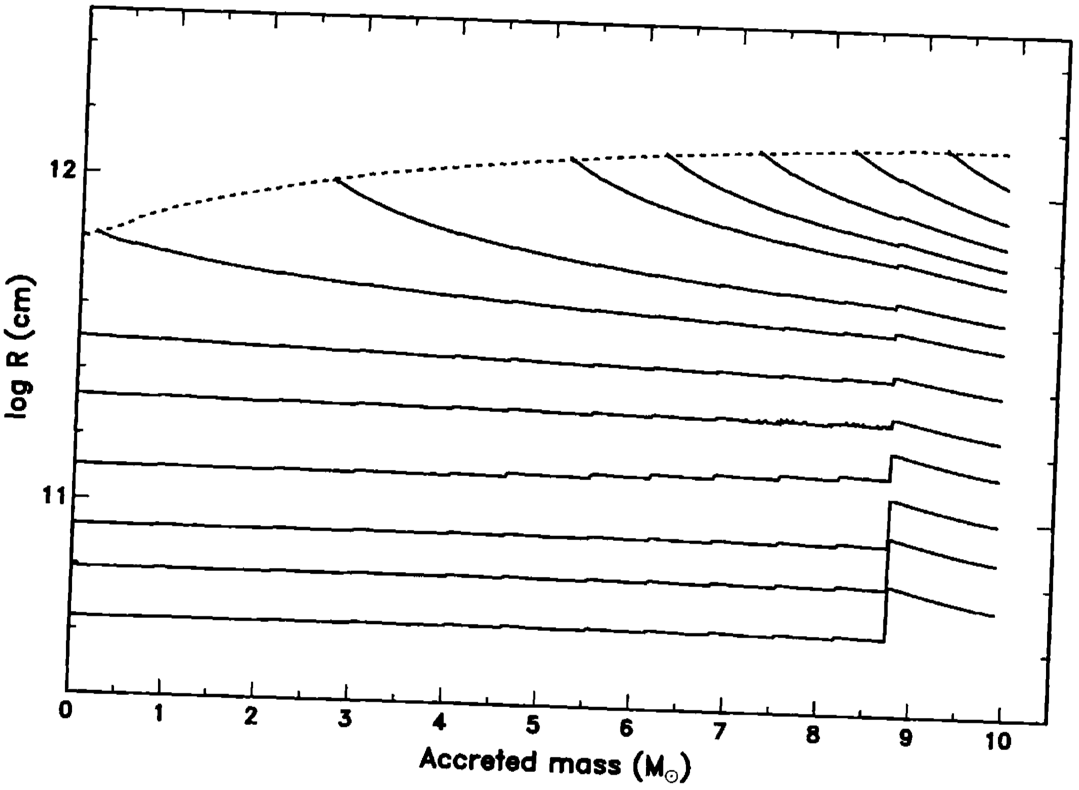

Figure 4-8: The evolution of the radius of layers of the secondary in sequence *A30p10* over the course of the mass transfer phase. The dotted line shows the radius of the star through the entire accretion phase.

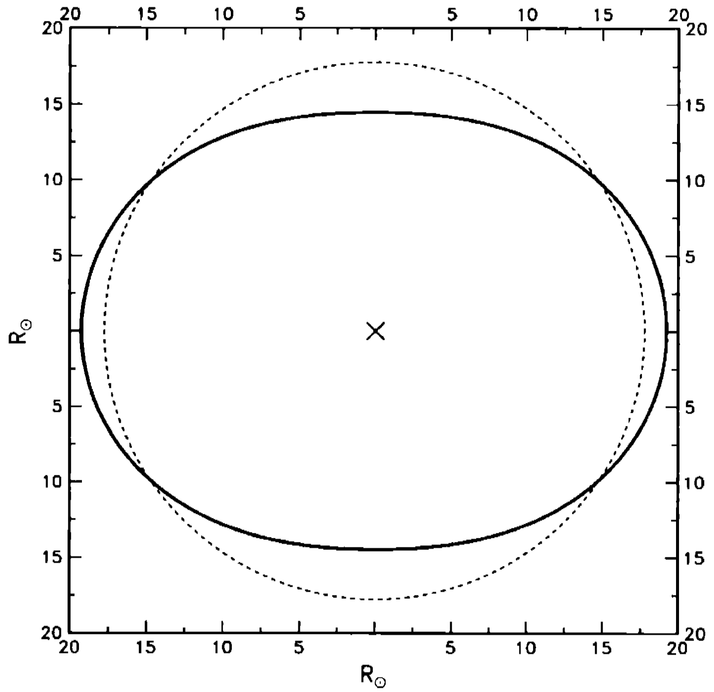

Figure 4-9: Plot of the outmost equipotential surface of the secondary of sequence $A30p10$, after it has accreted $10\,M_\odot$ of material from the primary (end of accretion phase). Shown for comparison is a sphere with volume equal to the volume enclosed by the equipotential surface.

past, becoming chemically and structurally indistinguishable from a main sequence star of its new, higher mass (see also Braun & Langer 1995). In the present case the rejuvenation event occurs while the star is still accreting mass, after a total of $8.7\,M_\odot$ has been transferred.

The envelope of the secondary at the end of the accretion phase is significantly distorted by the rapid rotation induced by the angular momentum it has accreted along with mass from the primary. Fig. 4-9 shows the distorted surface of the secondary at this point in its evolution.

4.3.3 Post-accretion evolution: $A30p10$

During the post-accretion evolution of the secondary of sequence $A30p10$, the no-torque level eventually dissipates, with the angular velocity distribution reconfiguring to become monotonically decreasing outward in the outer layers of the star (curves

D and E in Fig. 4-4). Angular momentum is transported down the gradient and outward to the stellar surface, where it is lost to the rotationally enhanced stellar wind. Owing to the relatively short amount of time over which this portion of the post-main-sequence evolution occurs, the effect of these losses on the final rotational state of the stellar core is negligible.

In the subsequent post-main-sequence evolution, the core and adjacent hydrogen-burning shell are rapidly brought into near solid-body rotation, aided by the establishment of convection in the core once helium burning is ignited. Transport of angular momentum into the core by IGWs is both inefficient and unnecessary in this case. The increase in the magnitude and non-uniformity of the core angular velocity distribution during late stages of evolution (curves D and E in Fig. 4-4) is primarily a result of the contraction of the core prior to the onset of carbon burning.

The rejuvenation of the core which occurs in sequence $A30p10$ is a feature common to all our LMS accretion models. The core-to-envelope mass ratio is increased as a result, which tends to drive the star redward in the HR diagram during its post-main-sequence evolution (see e.g. Braun & Langer 1995). As can be clearly seen in Fig. 4-3, the secondary of sequence $A30p10$ has proceeded well up the Hayashi track by the time carbon ignites in its core, ensuring that it will be a red supergiant when it eventually explodes as a Type-II supernova. The final mass of the secondary is $25.2\,M_{\odot}$, reduced from its maximum of $35\,M_{\odot}$ by the action of the stellar wind.

4.3.4 Angular momentum storage: $A30p10$

The profile of rapid differential rotation generated by accretion in the envelope of the secondary in $A30p10$ is capable of storing a large amount of angular momentum in the star, relative to that stored in an identical star in solid body rotation. This point is illustrated in Fig. 4-10 (early in the accretion phase), and in Fig. 4-11 (end of accretion phase). Rapid differential rotation of the star's outer layers, which constitute a large fraction of the total moment of inertia of the star, allows the star to spin less rapidly elsewhere in its interior, while still maintaining a large reservoir of angular momentum. A structurally identical star containing the same amount of angular momentum but constrained to rotate as a solid body is unable to do so without achieving super-Keplerian angular velocities at its surface after only a modest amount of mass has

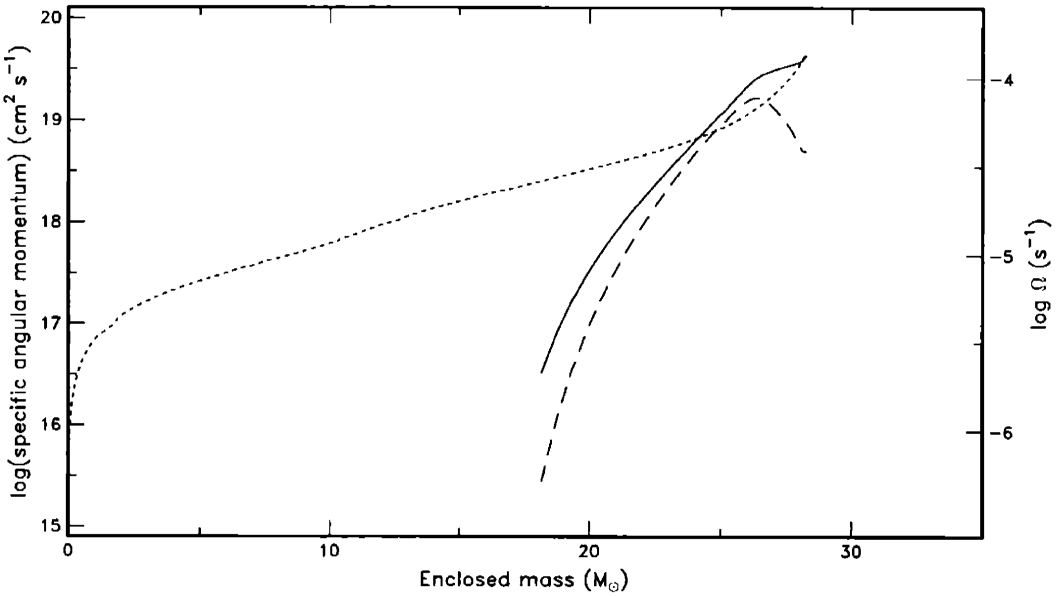

Figure 4-10: Specific angular momentum (j) distribution of the accreting secondary in $A30p10$ after 3.5 $M_\odot$ has been accreted (solid line, left scale), with the corresponding angular velocity distribution (long-dashed line, right scale). The short-dashed line shows the specific angular momentum distribution corresponding to the same model in solid body rotation at a rate which gives it the same total angular momentum (i.e. equal areas under both j curves). Note how the actual distribution of j (solid line) exceeds the solid body distribution (short-dashed line) in the outer layers of the star, where the moment of inertia is largest. The model in solid body rotation must make up the deficit it incures in the outer layers by extending its region of non-zero rotation to to the center of the star. Even this doesn't enable it to rotate at below breakup; the critical angular velocity at the surface is $\log \Omega_{\mathrm{k,eq}} = -4.25\,\mathrm{s}^{-1}$ and the star must rotate with $\log \Omega = -4.22\,\mathrm{s}^{-1}$ to contain the same amount of angular momentum.

been accreted there (Fig. 4-10). The same is true later in the accretion phase, only to a greater extent (Fig. 4-11). Related considerations on the angular momentum budget of an accreting secondary star in solid body rotation are presented in, e.g., Packet (1981).

4.3.5 Sequence $A40p10$

Fig. 4-12 through Fig. 4-15 show the evolution of the secondary of sequence $A40p10$, which accretes mass at $10^{-4}\,M_\odot\,\mathrm{yr}^{-1}$, one tenth the rate of sequence $A30p10$; otherwise the two systems are identical. As can be seen particularly in comparing curve A

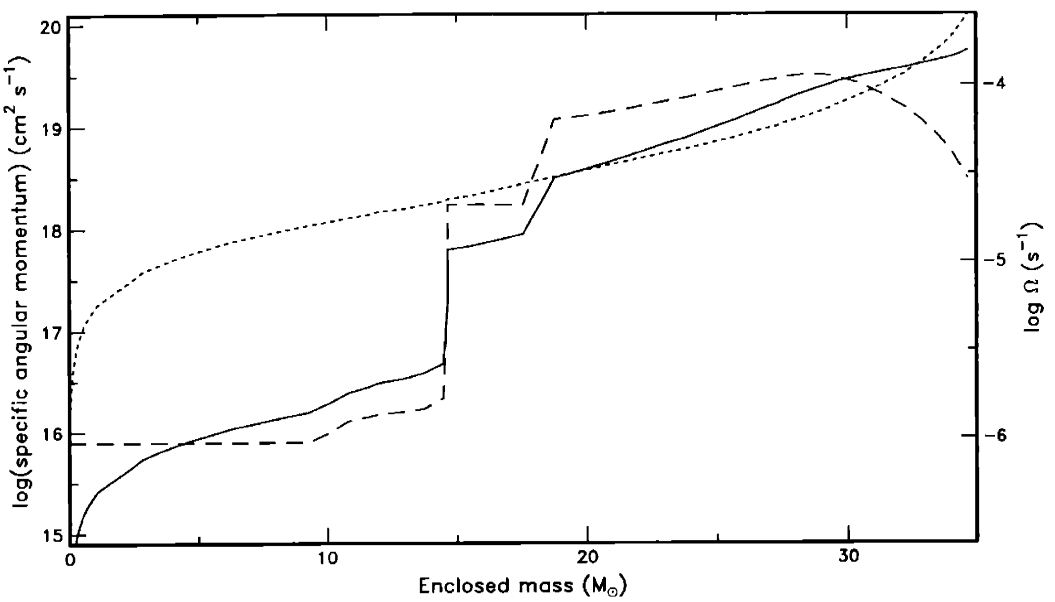

Figure 4-11: Same as Fig. 4-10 but just after mass transfer has ceased after $10\,M_\odot$ has been accreted by the secondary. The critical angular velocity at the surface is $\log \Omega_{\mathrm{k,eq}} = -4.38\,\mathrm{s}^{-1}$, and the star must rotate with $\log \Omega = -4.01\,\mathrm{s}^{-1}$ to contain the same amount of angular momentum.

in the present case with the same curve for sequence *A*30*p*10, the slower accretion rate allows a greater amount of angular momentum to enter the model before the no-slip point develops. A correspondingly increased amount of angular momentum enters the core, and the model retains its larger momentum reservoir until the end of its evolution. At core carbon ignition the core of the star is rotating at $\Omega = 3.2 \times 10^{-3}\,\mathrm{s}^{-1}$, compared to $\Omega = 3.7 \times 10^{-4}\,\mathrm{s}^{-1}$ for sequence *A*30*p*10. The secondary retains more of its hydrogen envelope, $28.5\,M_\odot$, and consequently has a larger final radius than the secondary of sequence *A*30*p*10.

4.3.6 Sequence *A*20*p*10

Fig. 4-16 through Fig. 4-19 show the evolution of the secondary of sequence *A*20*p*10, which accretes mass at $10^{-2}\,M_\odot\,\mathrm{yr}^{-1}$, ten times the rate of sequence *A*30*p*10; otherwise the two systems are identical. The rapid accretion rate in this case drives the secondary farther from thermal equilibrium than the other cases of LMS accretion considered above (see the HR diagram of Fig. 4-16). The short accretion time scale

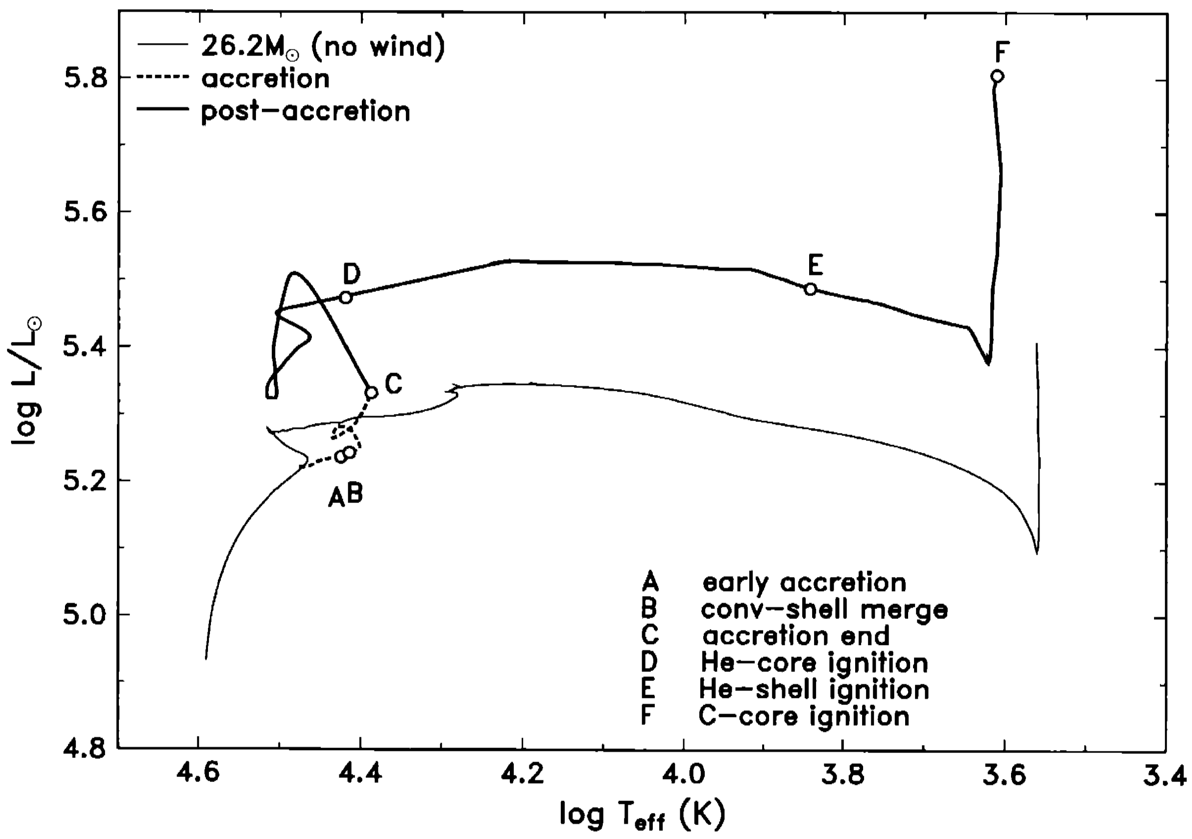

Figure 4-12: HR diagram for sequence *A*40*p*10; the caption of Fig. 4-3 applies.

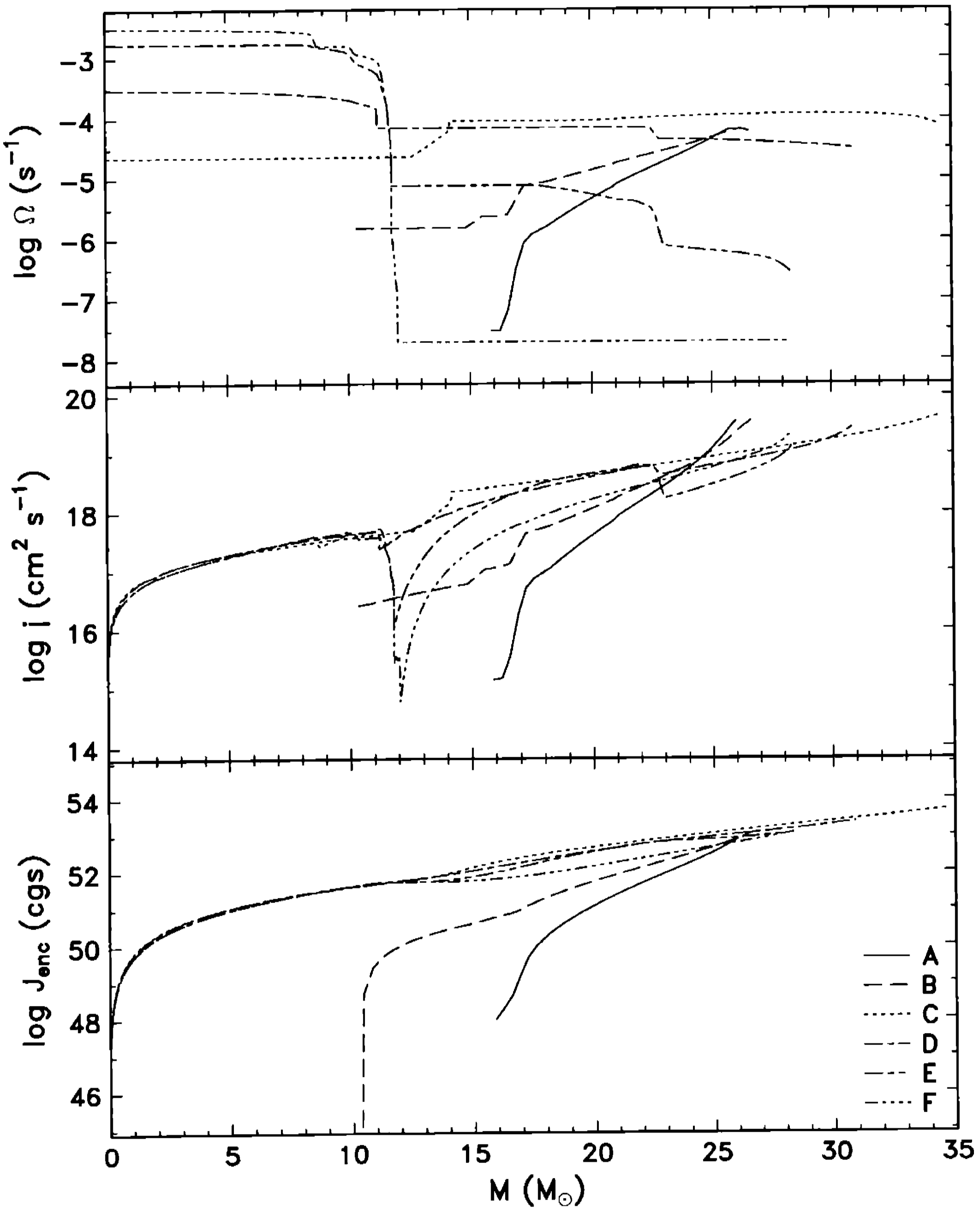

Figure 4-13: Same variables as shown in Fig. 4-4 for sequence A40p10

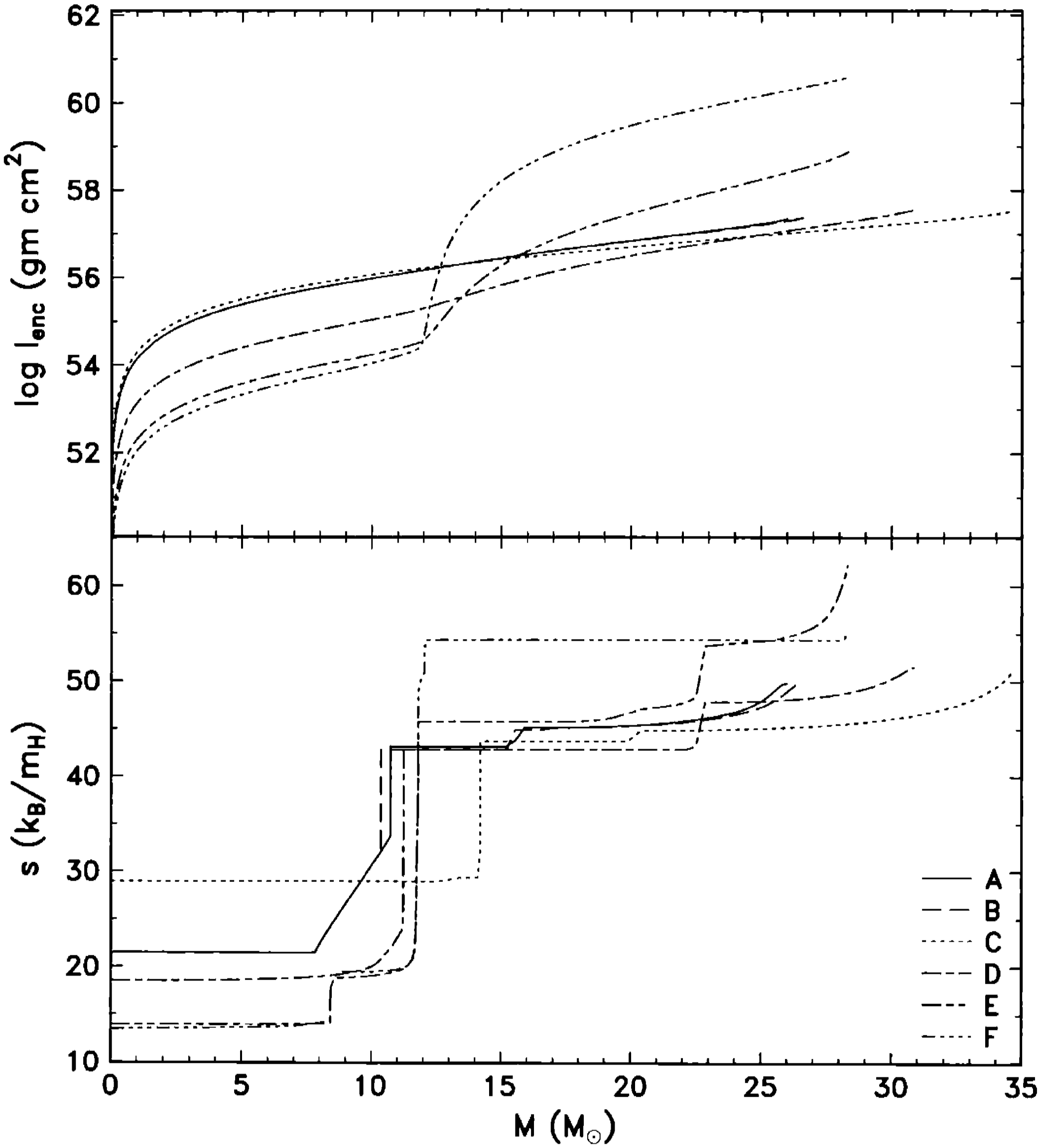

Figure 4-14: Same variables as shown in Fig. 4-5 for sequence A40p10

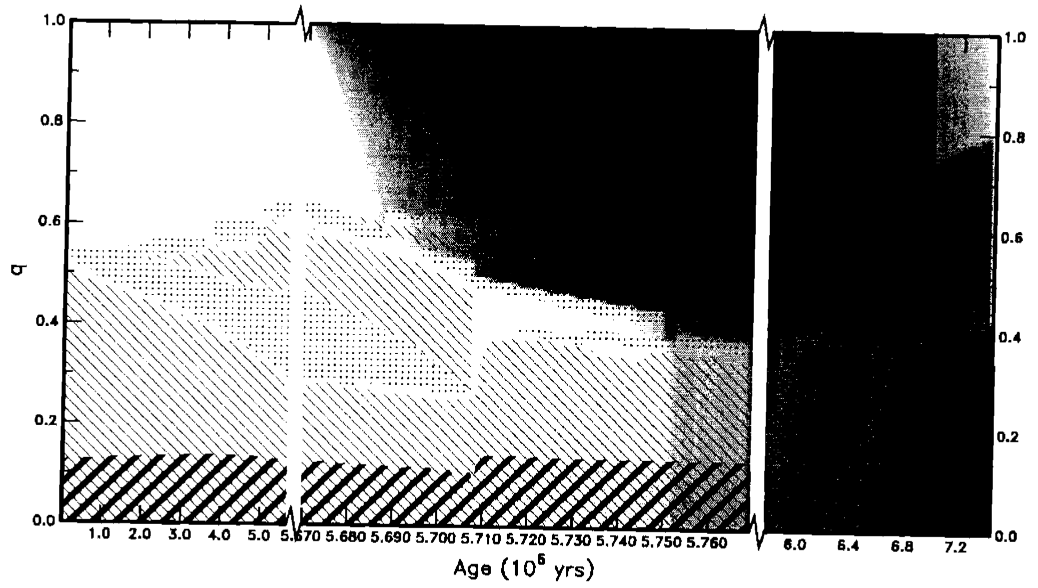

Figure 4-15: Kippenhahn diagram for sequence *A*40*p*10

in this case also results in less total angular momentum entering the secondary before the no-slip zone develops, and a larger fraction of the angular momentum taken up by the star concentrates far from the core (see curve D in the plot of j in Fig. 4-17). After mass transfer ceases and the secondary moves into the red-giant region, its mass loss rate by a rotationally enhanced stellar wind becomes large, due to the outward transport of the large amount of angular momentum stored well outside the core. Mass loss continues until the secondary reaches a mass of $15.5\,M_\odot$. We could not continue the calculation beyond this point due to numerical difficulties related to the large and rapid, mass-loss induced structural changes to the star. At the end point of its evolution the core of the star is rotating at $\Omega = 8.7 \times 10^{-6}\,\mathrm{s}^{-1}$.

4.4 Early post main sequence accretion case

Sequences in which the secondary begins accreting mass after it has left the main sequence are qualitatively different than the late main sequence accretion cases considered in previous sections. This is mainly due to structural changes in and near

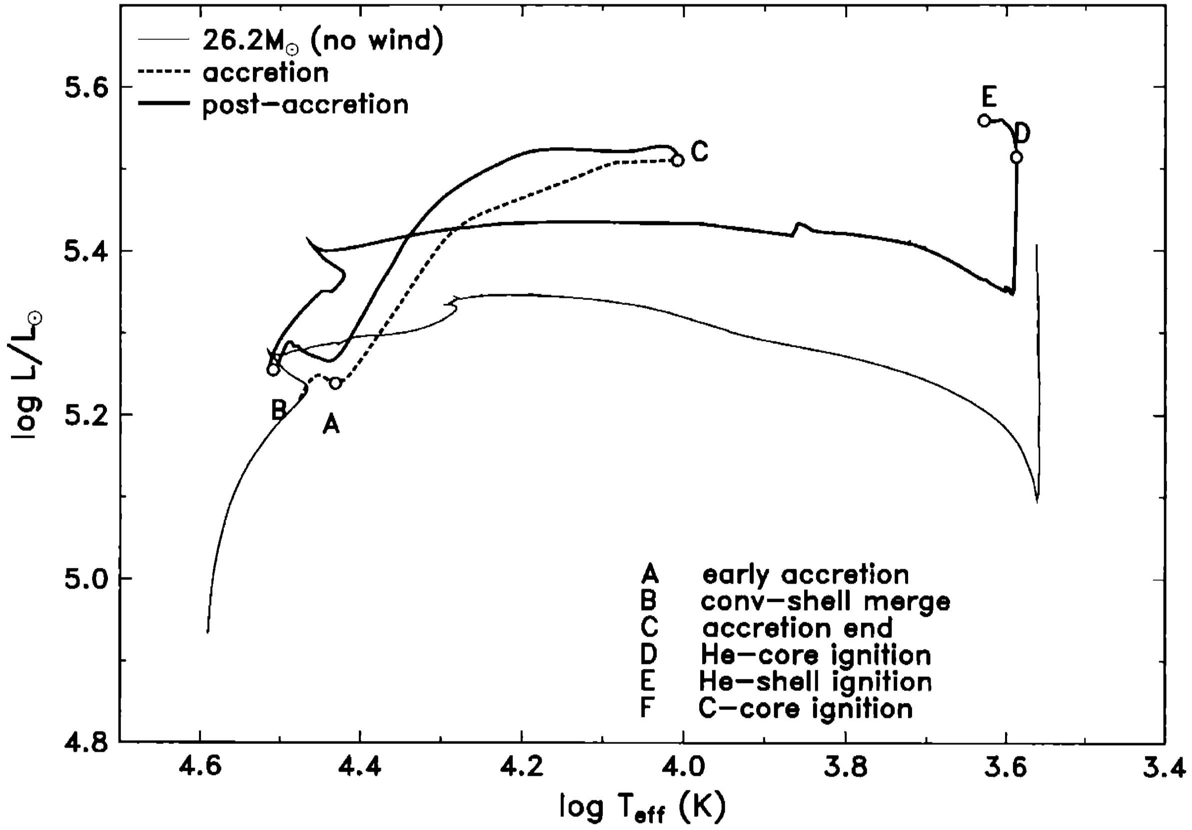

Figure 4-16: HR diagram for sequence *A*20*p*10; the caption of Fig. 4-3 applies.

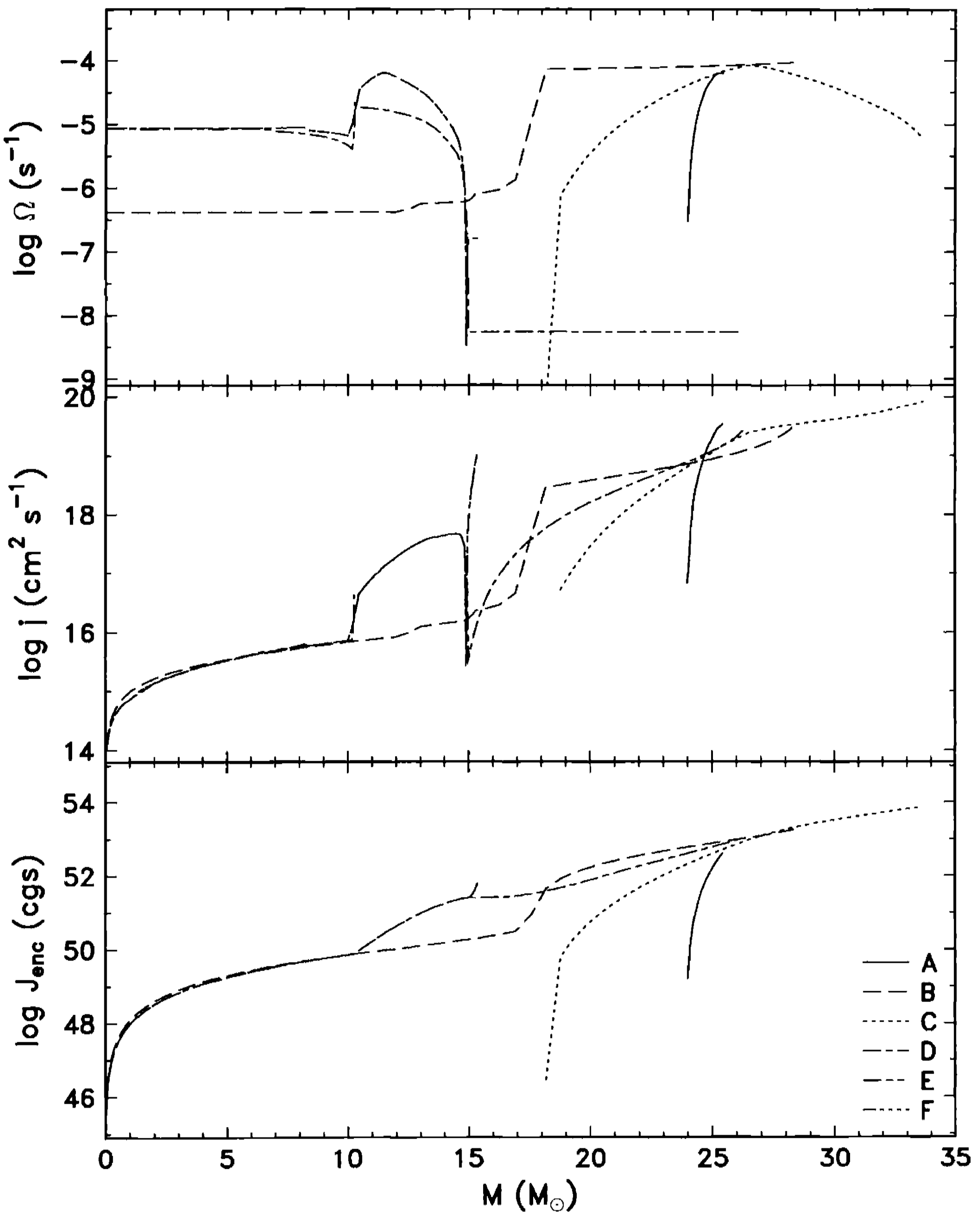

Figure 4-17: Same variables as shown in Fig. 4-4 for sequence $A20p10$

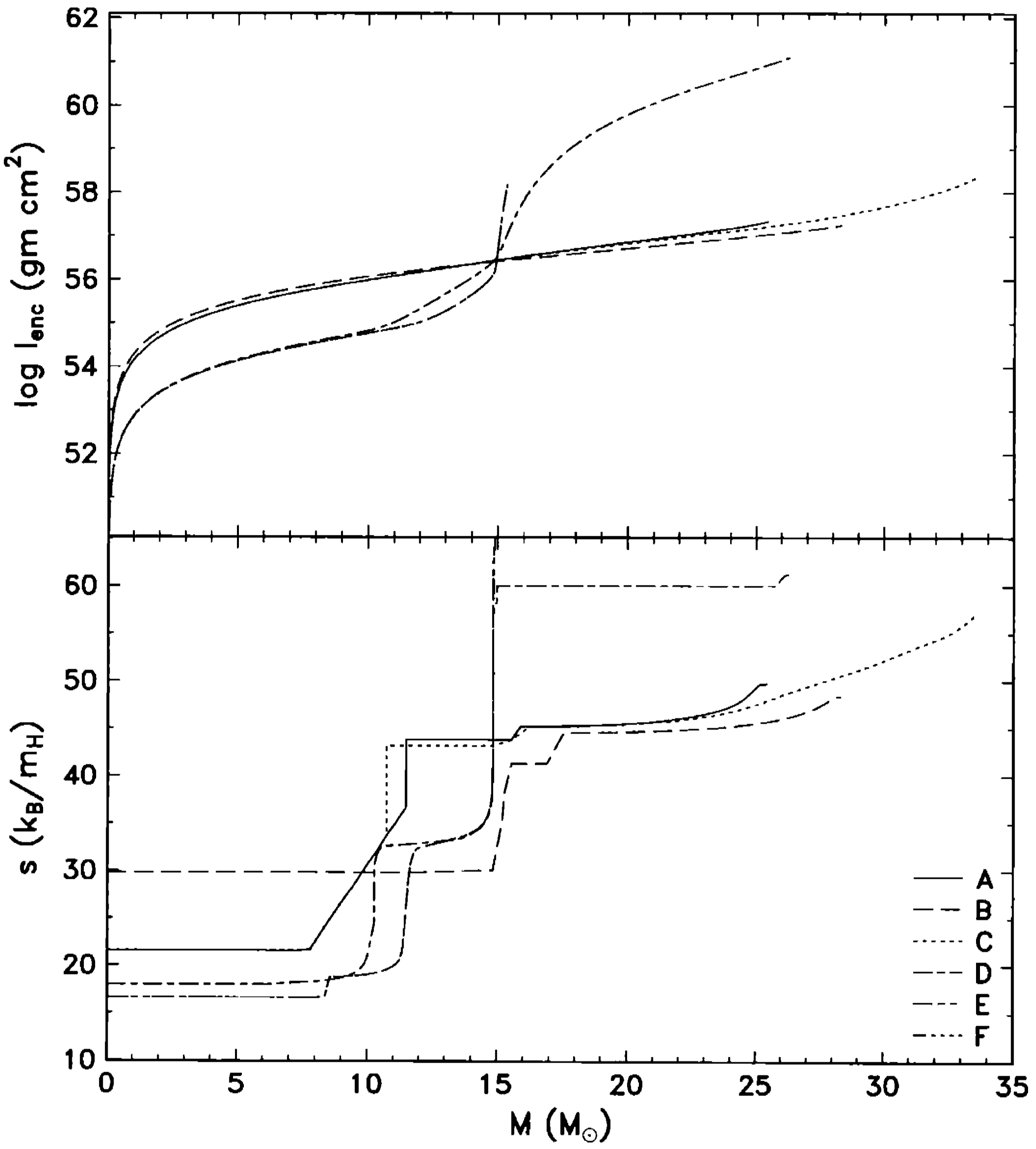

Figure 4-18: Same variables as shown in Fig. 4-5 for sequence A20p10

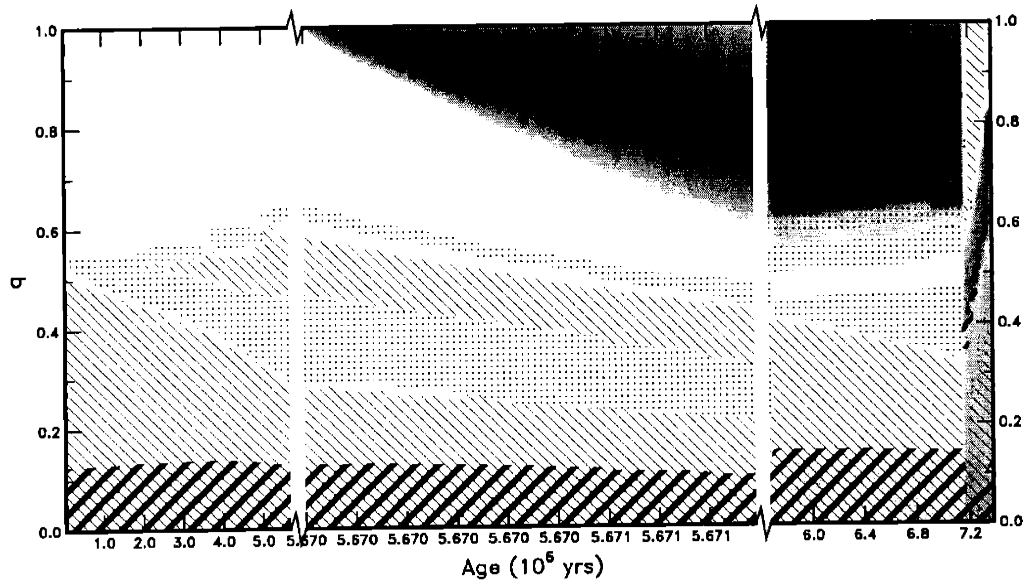

Figure 4-19: Kippenhahn diagram for sequence $A20p10$

the core of the star, which stabilize this region very effectively against the hydrodynamic instabilites which give rise to turbulence. The core responds to the cessation of hydrogen burning by contracting (seen as the leftward excursion by the $26.2\,M_\odot$ no-wind star after it has left the main sequence). The ignition of the hydrogen burning shell (the kink in the path of the $26.2\,M_\odot$ star) further increases the isolation of the core. We find that IGWs are effective in transporting angular momentum across the core-envelope interface during the relatively long core helium burning phase of the secondary (see Chapter 2.4).

4.4.1 Sequence $B31p10$

Fig. 4-20 through Fig. 4-23 illustrate the evolution of model $B31p10$, a $26.2\,M_\odot$ secondary which accretes $10\,M_\odot$ from the primary just after hydrogen burning has ceased in the core and begun in a surrounding shell (early post-main-sequence accretion case). The early stages of accretion are very similar to those described above for the late main sequence accretion scenario and so will not be repeated. In this case, the large luminosity of the hydrogen burning shell and the near uniform composition of the

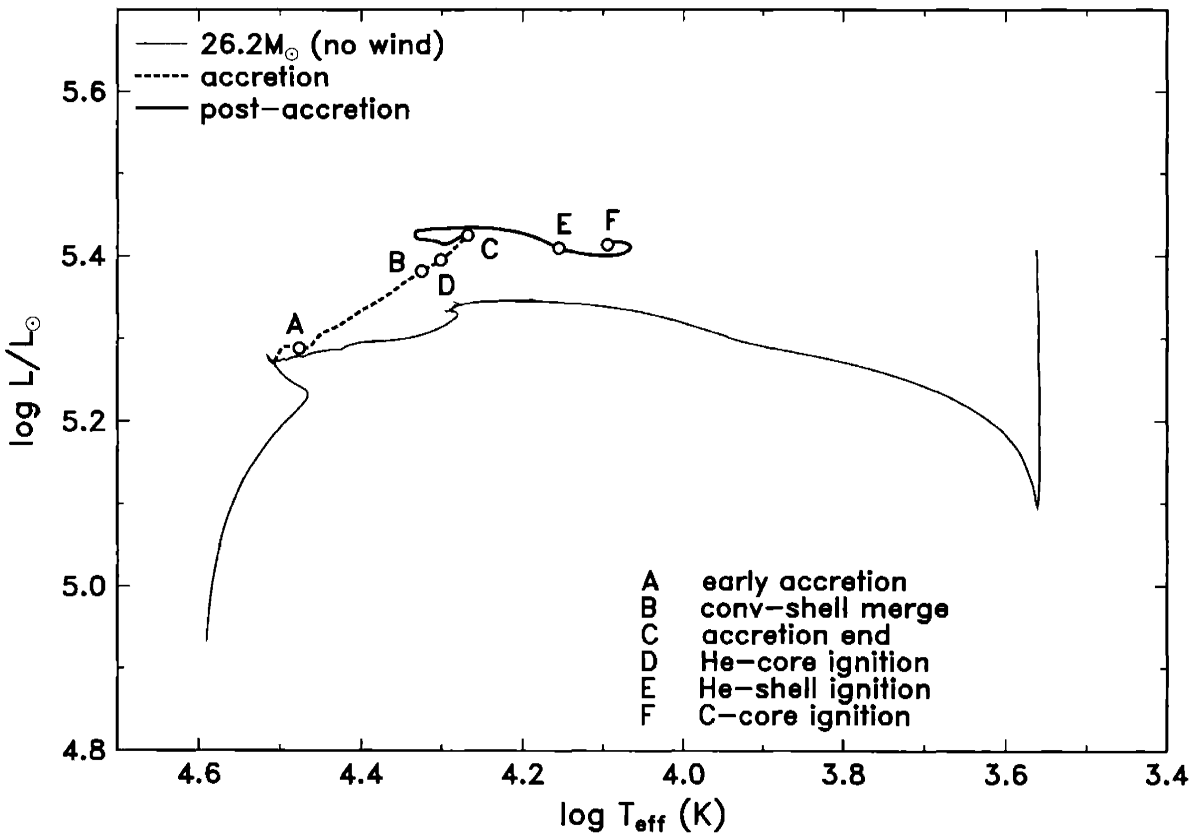

Figure 4-20: HR diagram for sequence $B31p10$; the caption of Fig. 4-3 applies.

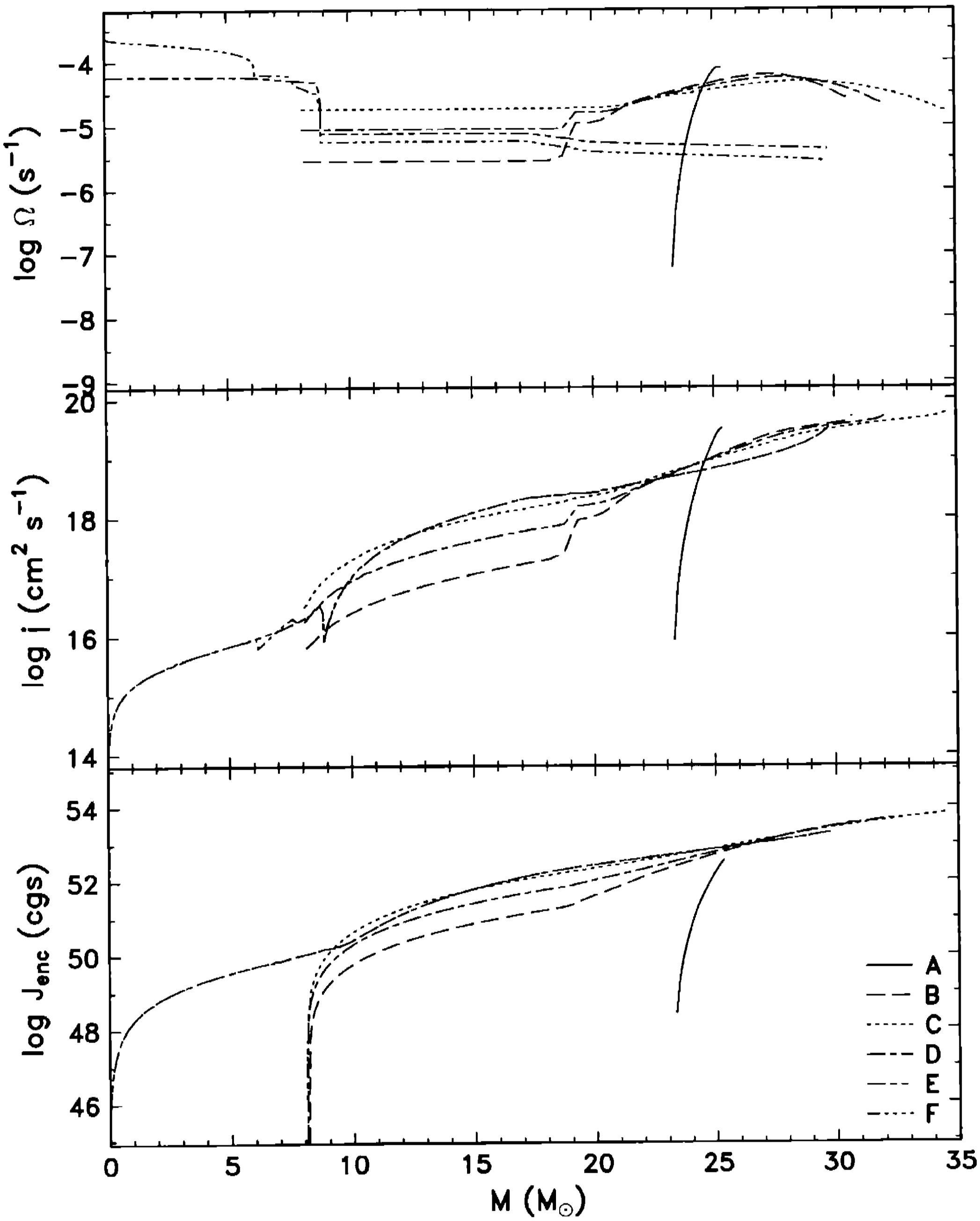

Figure 4-21: Same variables as shown in Fig. 4-4 for sequence $B31p10$

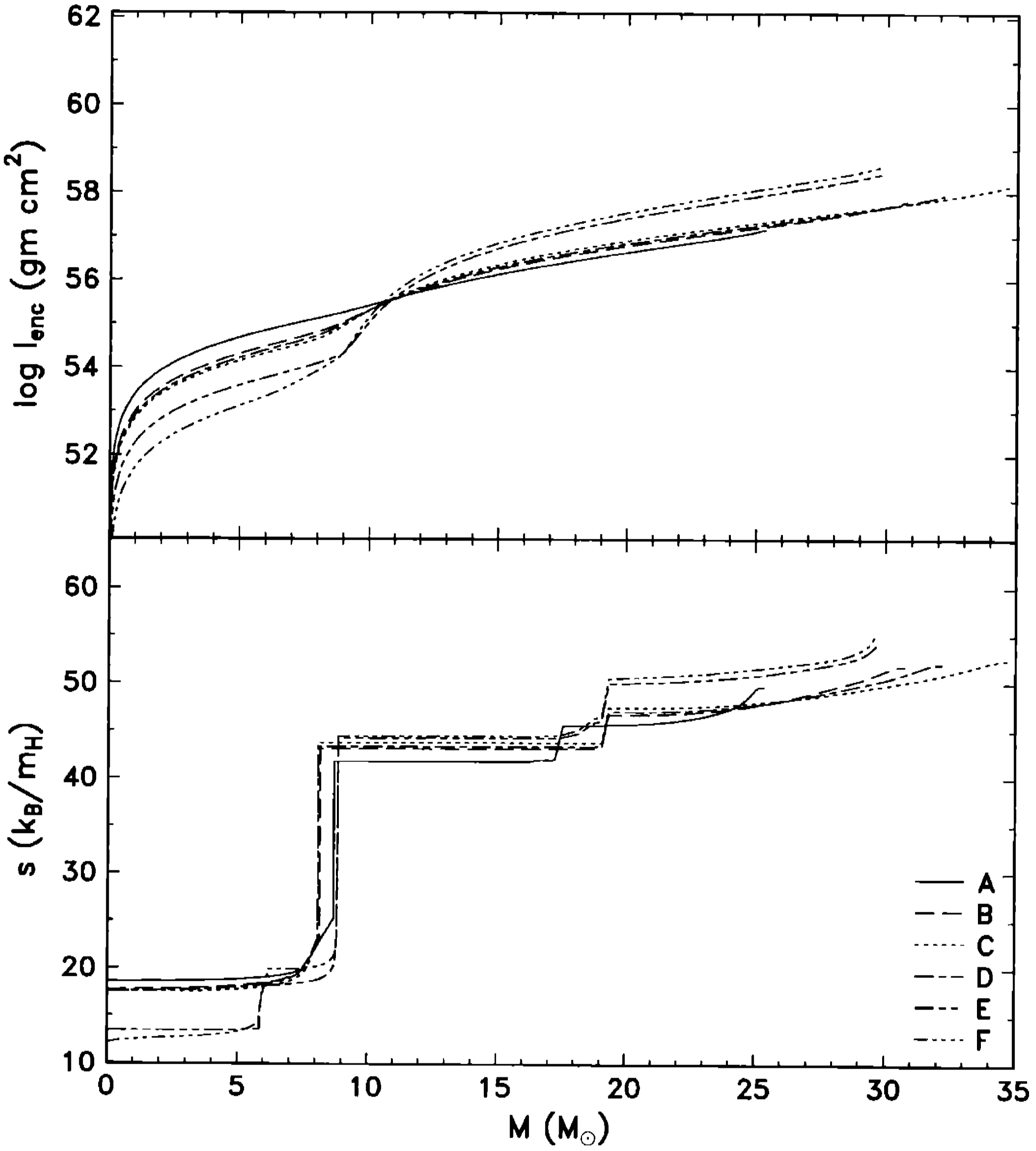

Figure 4-22: Same variables as shown in Fig. 4-5 for sequence *B*31*p*10

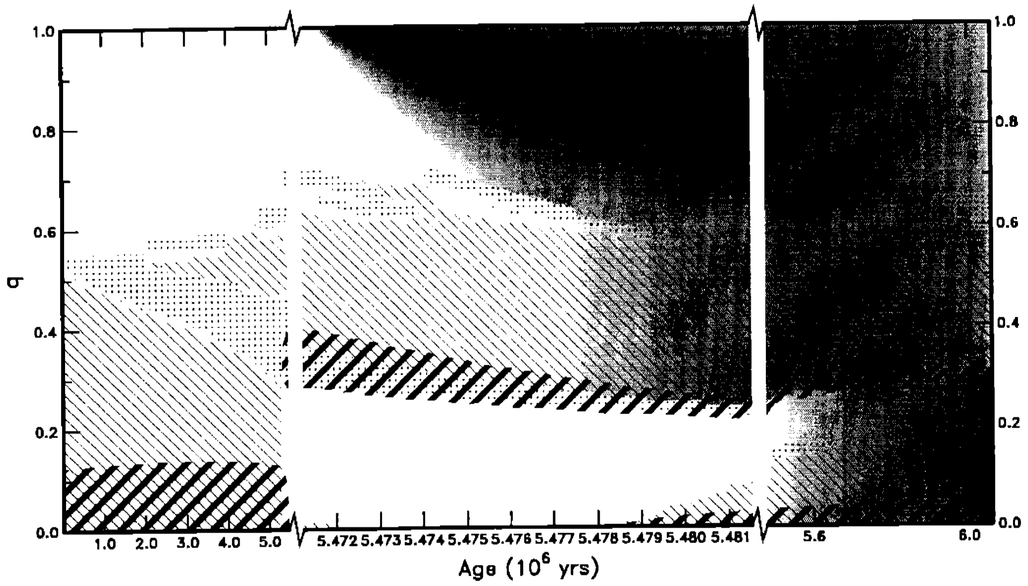

Figure 4-23: Kippenhahn diagram for sequence $B31p10$

region above it, result in the formation of an extensive convective region extending outward from the shell (Lamb et al. 1976); see curve B in Fig. 4-21. This convective region effectively transfers angular momentum from its outer to inner edge, leading to rapid shear buildup at the convective/stratified interface at the edge of the core. The density gradient at the edge of the core in this case is strong enough to stabilize the shear flow between the rotating shell and the core, and angular momentum penetrates no further (see Fig. 4-21, j curves A-C). Rather, gravity waves are generated on the interface and within the region of rising buoyancy frequency just inside the convective shell by the mechanisms discussed in Chapter 2.4. The nonlinear processes involved in the coupling of surface gravity waves to internal waves, internal wave-wave coupling, and wave breaking are rather poorly understood, even in terrestrial contexts such as the oceans. The waves are likely trapped in the radiatively stable core, where they will eventually dissipate. Through the action of convection and other mechanisms not followed in detail in these calculations, we assume the core is eventually brought into a state of solid body rotation, after which evolution proceeds as described in the previous case.

The strong stratification at the edge of the core in the secondary of sequence $B31p10$ also inhibits the processes leading to core rejuvenation, in contrast to the main-sequence accretion models considered above. This region effectively isolates the core from the envelope of the star, and hence from any convective regions with the potential to provide fresh hydrogen or helium fuel. The core to mass ratio q consequently remains small, and the star stays near in the blue supergiant region of the HR diagram (Fig. 4-20).

4.4.2 Other EPMS sequences

Sequence $B30p10$, Fig. 4-24 through Fig. 4-27, is identical to $B31p10$ except that IGW transport of angular momentum is assumed to be inoperative at the core-envelope interface. As the curves of Fig. 4-25 show, the core remains non-rotating in this case.

The secondary of sequence $B30p05$, Fig. 4-28 through Fig. 4-31 accretes $5\,M_\odot$ rather than $10\,M_\odot$ from its companion. Not enough angular momentum is gained by the secondary in this case to spin up the intermediate convective zone. The core therefore remains non-rotating.

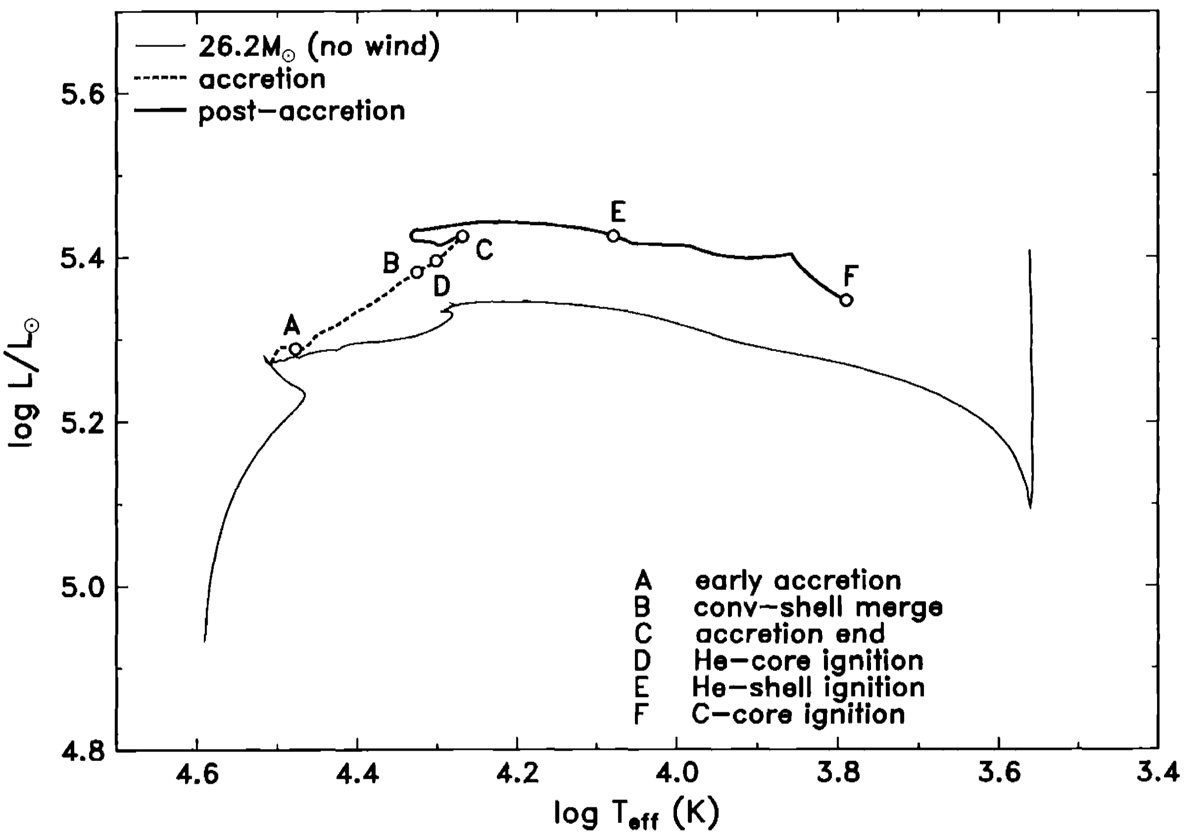

Figure 4-24: HR diagram for sequence $B30p10$; the caption of Fig. 4-3 applies.

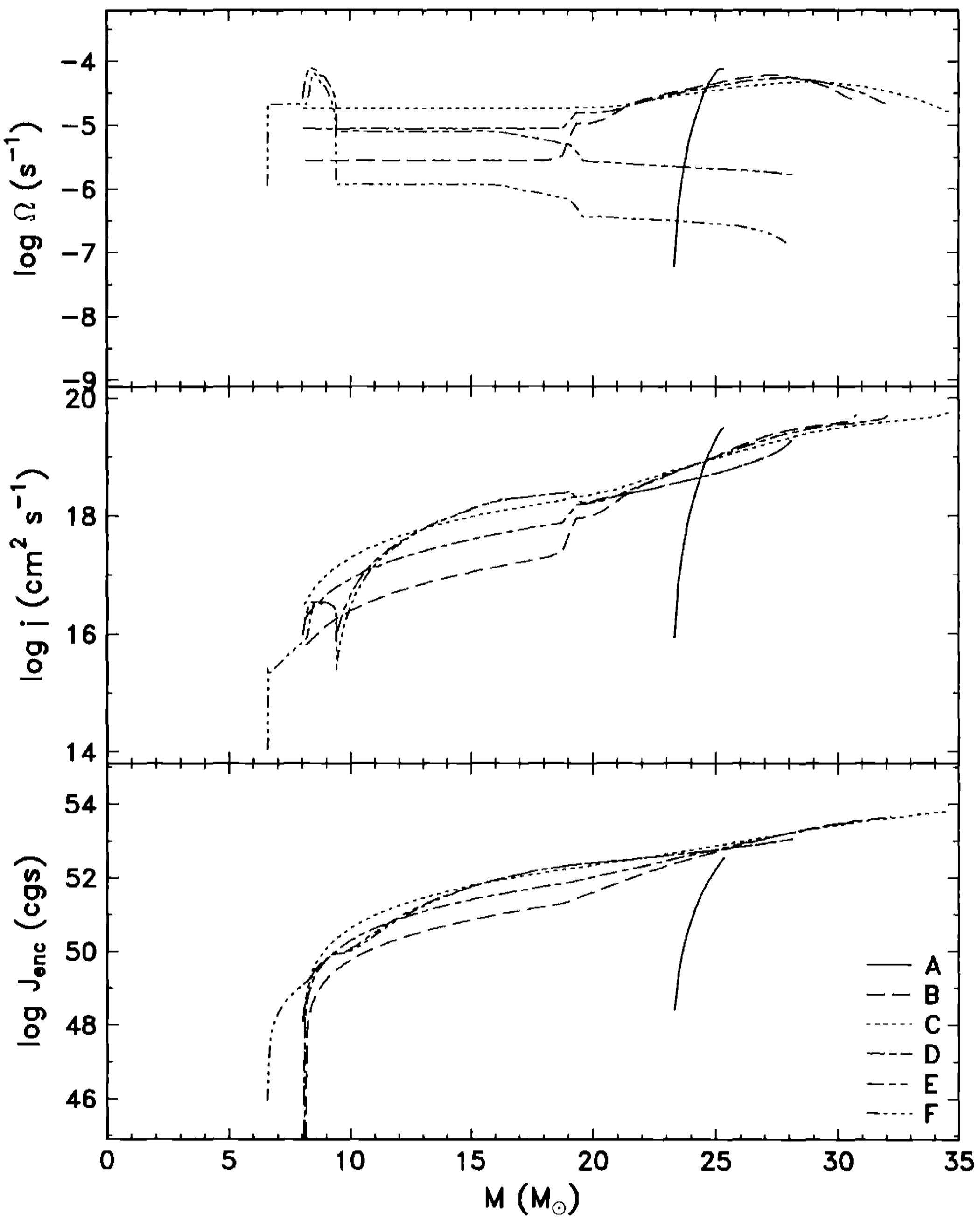

Figure 4-25: Same variables as shown in Fig. 4-4 for sequence $B30p10$

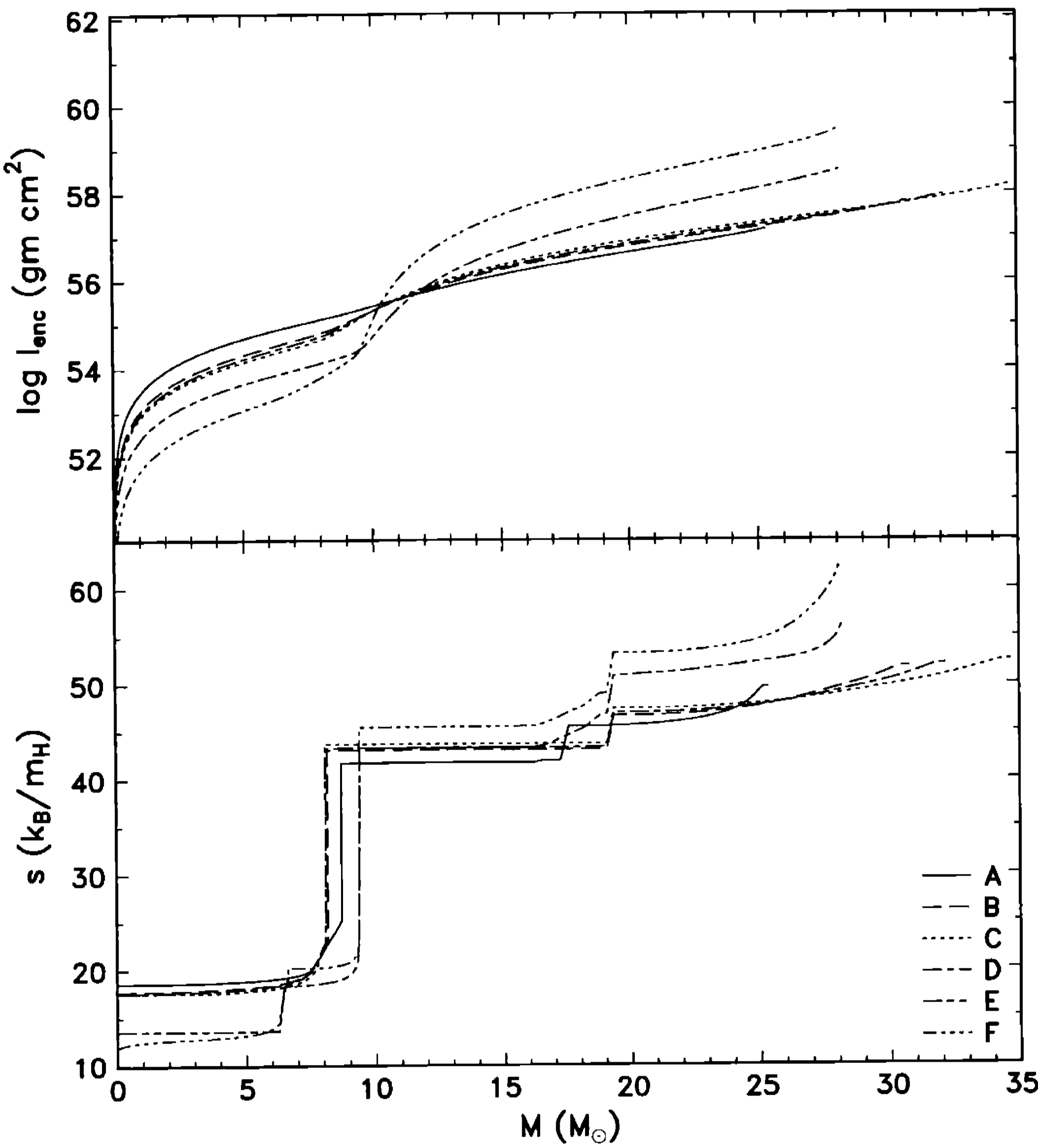

Figure 4-26: Same variables as shown in Fig. 4-5 for sequence *B*30*p*10

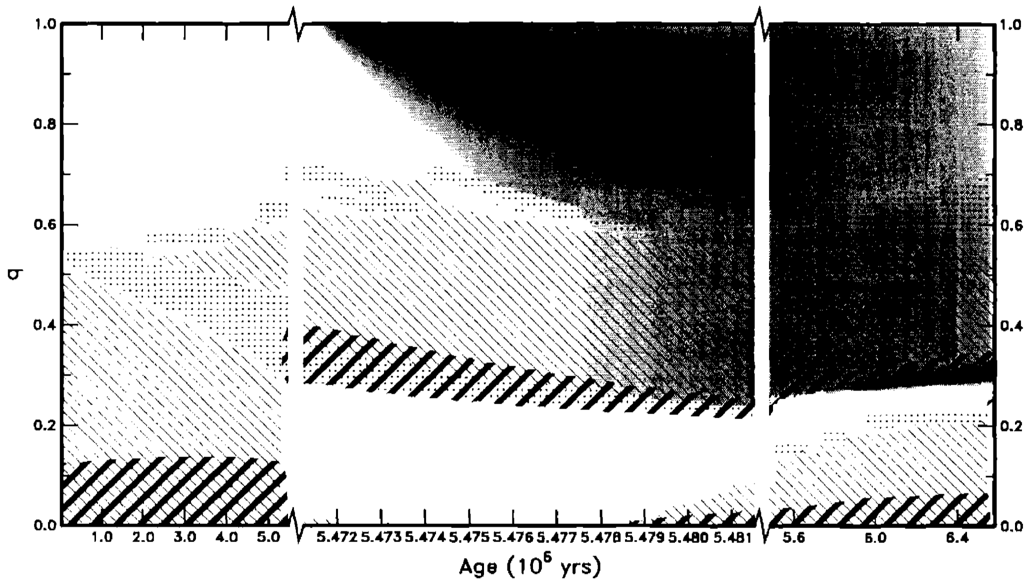

Figure 4-27: Kippenhahn diagram for sequence $B30p10$

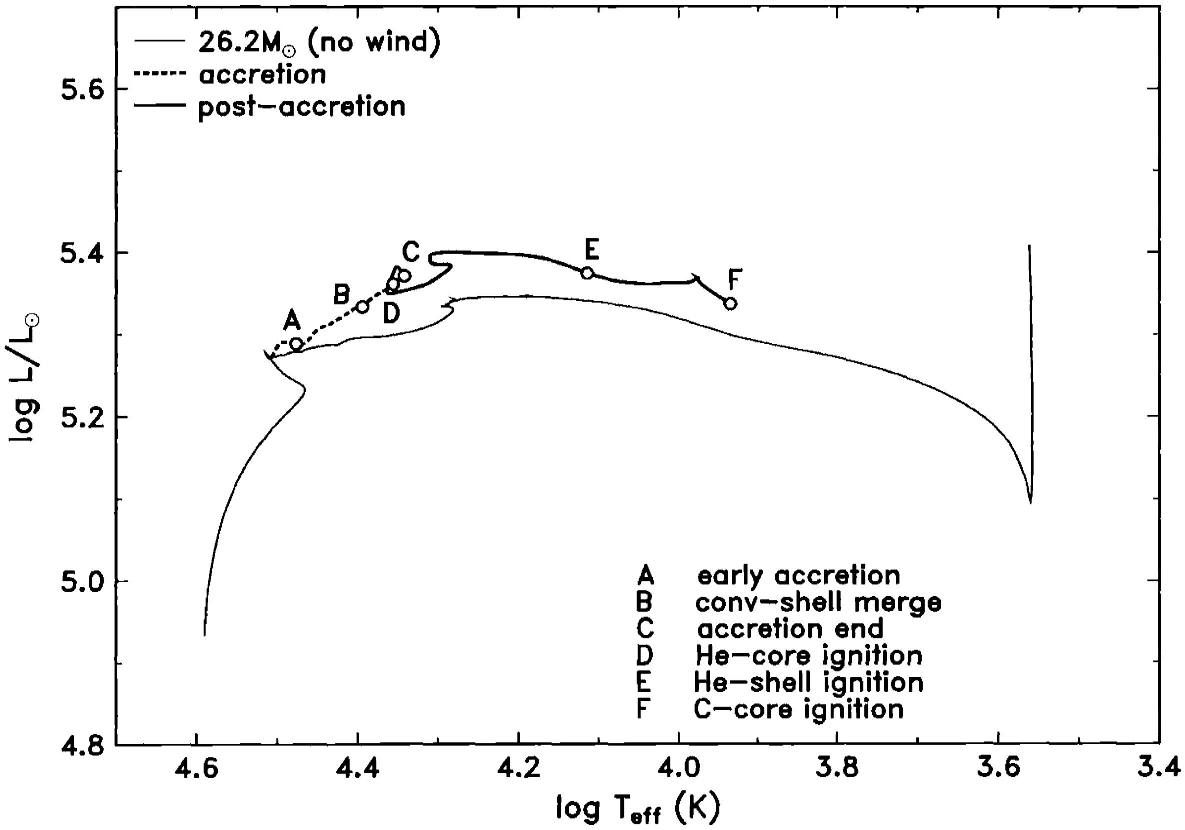

Figure 4-28: HR diagram for sequence $B30p05$; otherwise the caption of Fig. 4-3 applies.

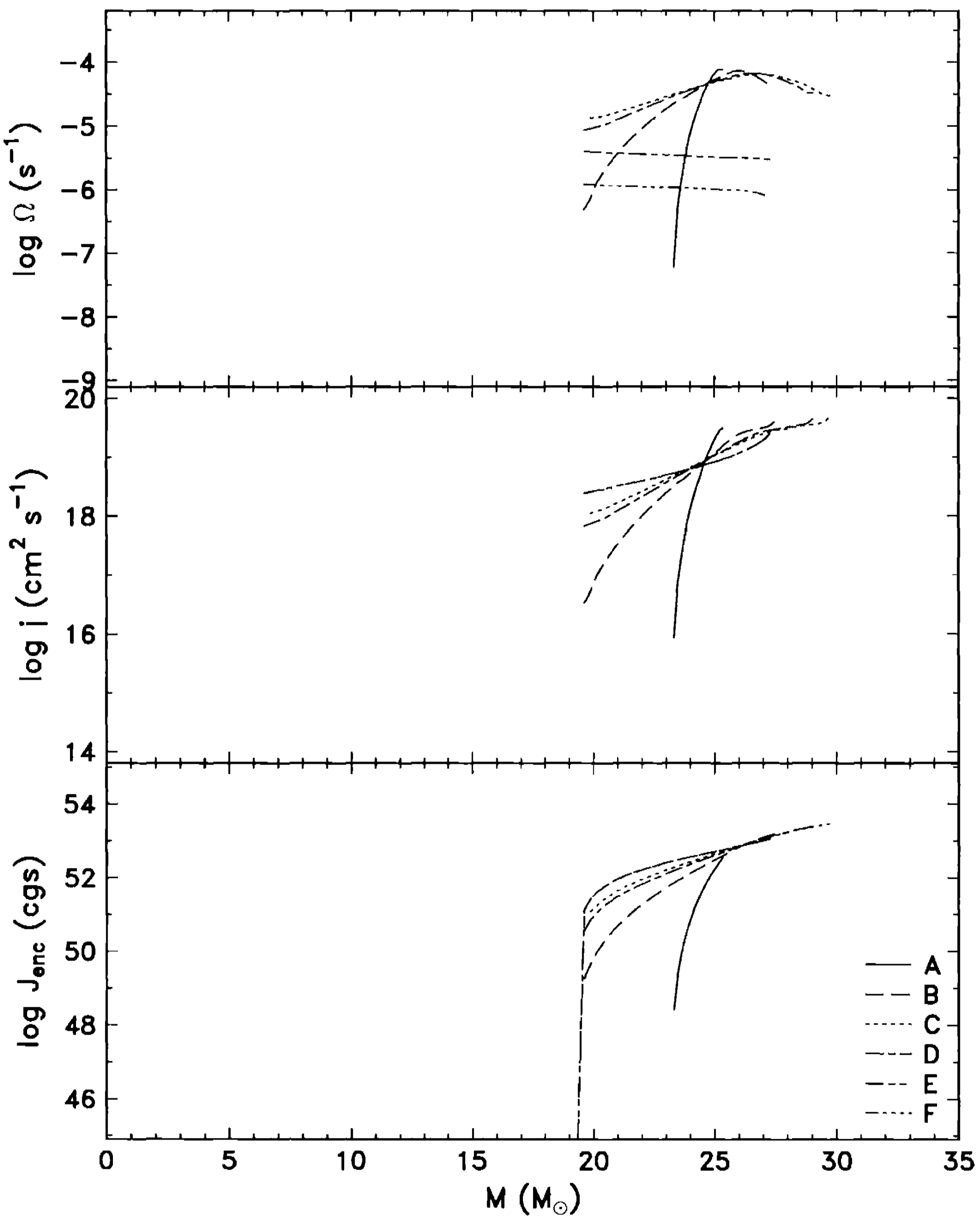

Figure 4-29: Same variables as shown in Fig. 4-4 for sequence $B30p05$

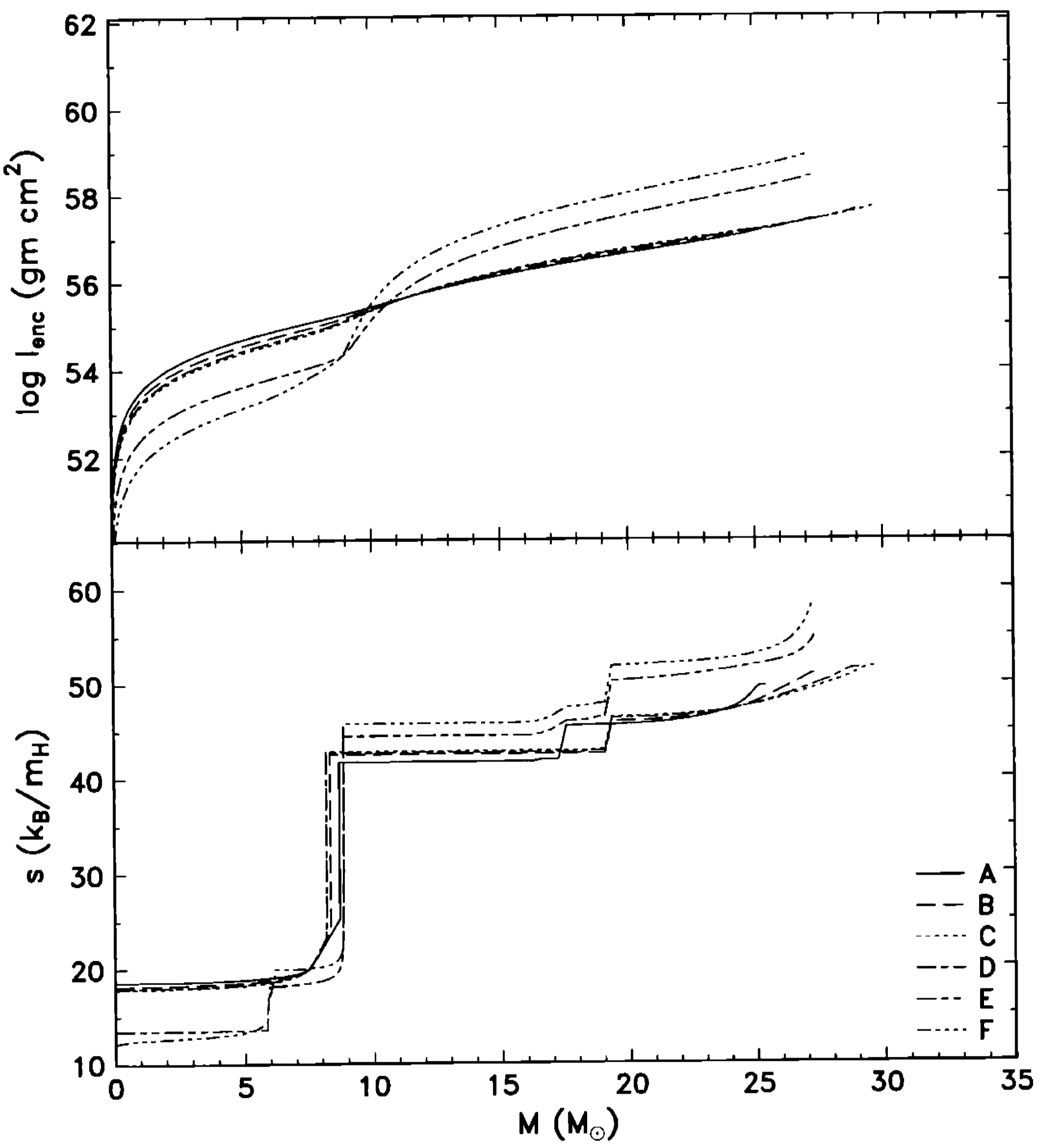

Figure 4-30: Same variables as shown in Fig. 4-5 for sequence $B30p05$

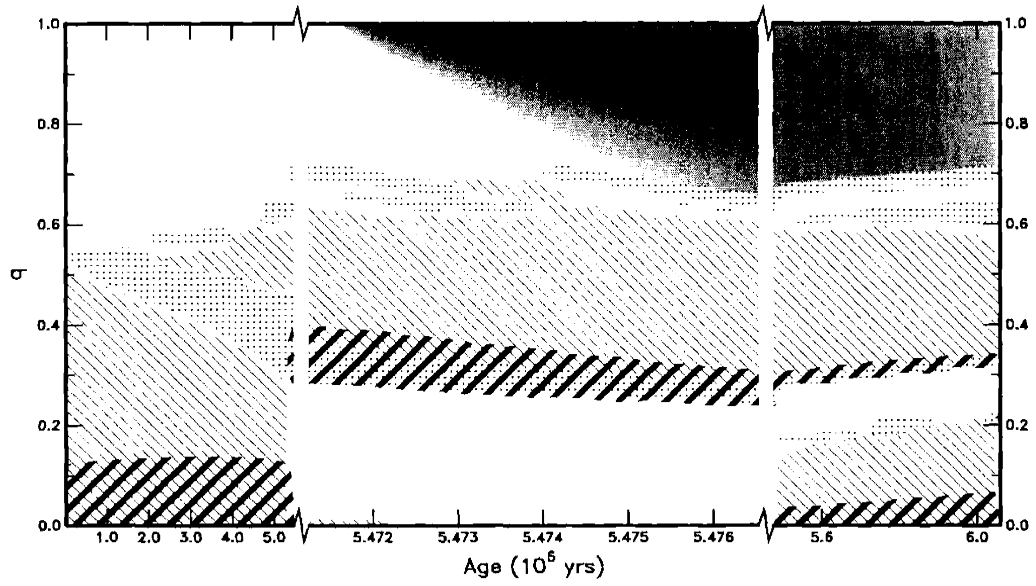

Figure 4-31: Kippenhahn diagram for sequence $B30p05$

Chapter 5

Common envelope evolution

One of the most profound interactions that can take place between two stars in a binary system occurs when the mass transfer process becomes dynamical and the two components end up engulfed by a shared envelope of overflowing gas, or a so-called common envelope (CE) (Paczyński 1976; Meyer & Meyer-Hofmeister 1979; Taam et al. 1978; Taam & Sandquist 2000). Such systems typically consist of an evolved red-giant (the primary component) which overflows its Roche lobe late in its evolution to initiate the CE phase, and a significantly less massive main-sequence companion (the secondary). The secondary cannot accept the mass proffered by the primary fast enough, and quickly becomes engulfed in the overflowing material. This material eventually forms the common envelope, within which the secondary and the red-giant core of the primary orbit about one another. If the mass ratio $q = M_1/M_2$ is extreme enough, the orbit of the embedded bodies is unable to provide sufficient angular momentum to the envelope to keep it in corotation. The consequent nonzero relative velocity between the secondary and the envelope gives rise to dynamical friction[1] which shrinks the orbit. Some fraction of the liberated energy and angular momentum is deposited into the CE, which may be ejected as a result.

In particular, if the amount of energy deposited into the envelope is a large fraction of its gravitational binding energy, the envelope may be partially or completely ejected. The surviving system in this case will be a much closer binary, consisting of the core of the giant and the essentially unaltered main-sequence secondary. Alterna-

---

[1] In the form of a detached bow shock in the direction of motion and a gravitational wake behind (Bondi & Hoyle 1944; Alexander et al. 1976).

tively, if the envelope is not ejected there follows a phase of slower spiral-in, in which the friction-generated luminosity and the drag viscosity self-consistently regulate each other to maintain a roughly constant total luminosity (Meyer & Meyer-Hofmeister 1979), which is transported to the surface and radiated away from the the envelope. This slow spiral-in phase continues until the orbital separation becomes small enough to bring the embedded secondary star into contact with its own shrinking Roche lobe, initiating a secondary, rapid mass transfer from the secondary, now deeply embedded within the CE close to the core of the primary. Such a direct transfer of mass and angular momentum to the core of the primary will result in, among other things, its rapid rotational angular acceleration. Since it is acquired by the core late in its evolutionary lifetime, very little of this angular momentum will be able to escape from the core via the usual instabilites prior to the collapse of the core. The resulting single star, consisting of a rapidly spinning core surrounded by an envelope possibly reduced in mass via CE evolutionary processes, in principle possesses all of the required attributes of a viable gamma-ray burst progenitor.

5.1 Slow merger of massive stars

Ivanova, Podsiadlowski, & Spruit (2002) (hereafter IPS) refer to dissolution of the secondary and the transfer of its mass to the core of the primary within the CE as a "slow merger" event. These authors have carried out a variety of hydrodynamic simulations of this process in order to investigate the physics of the interaction between the giant's core and the stream of material from the secondary, which both impinges upon, and penetrates it. They find that the mass transferred from the secondary is capable of penetrating the hydrogen burning shell surrounding the hydrogen-exhausted core and reaching a final penetration depth somewhat above the helium exhausted core[2] The depth reached by the stream is primarily a function of the core's rotation and the specific entropy of the stream material which can be altered as the stream propagates through the CE into the core. In cases where the core is initially slowly rotating, they find that it can acquire a significant amount of angular momentum from the impinging stream.

---

[2] They assume the primary is an asymptotic branch red-giant which has completed core helium burning at the onset of the slow merger phase.

In the present chapter we report on calculations we carried out of the slow merger of a 20 $M_\odot$ primary with a 6 $M_\odot$ secondary using the formalism developed by IPS. § 5.2 describes the modifications we made to our stellar evolution code, and § 5.3 summarizes the results.

5.2 Numerical implementation

We modified our stellar evolution code (see Chapter 2) to incorporate two distinct phases of a common envelope merger: (i) the spiral-in phase, in which the gravitational field and frictional and accretion luminosity of the embedded secondary is included in the calculation of the structure of the primary's envelope (the CE); (ii) the slow merger phase, in which the mass and associated angular momentum which is lost from the secondary is injected into the primary at a depth interior to the position of the secondary determined using the results of IPS.

We follow Podsiadlowski et al. (1992) and include the gravitational effect of the secondary on the primary's envelope by modifying the gravitational constant to $G'/G = [M(r)+M_2]/M(r)$ for $r > a(t)$, where $a(t)$ is the orbital separation and $M(r)$ is the mass of the primary interior to radius r. We determine the orbital decay rate by assuming constant frictional and accretion luminosity (Meyer & Meyer-Hofmeister 1979), which decreases the orbital energy and orbital separation $a(t)$ at the rate

$$\frac{dE_{\rm orb}}{dt} = L_{fric} = \frac{GM(a)M_2}{2a^2}\frac{da}{dt}\,. \tag{5.1}$$

Over a time step Δt we add the frictional luminosity $L_{fric}\Delta t$ and angular momentum lost from the orbit, $\dot{J}\Delta t$ to the mass shell in which the secondary is located at time t. The latter quantity is determined from the expression for the orbital angular momentum Eq. (4.2)

$$\frac{dJ}{dt} = \frac{1}{2}M_1M_2\sqrt{\frac{G}{(M_1+M_2)a}}\frac{da}{dt} \tag{5.2}$$

The merging phase begins when the orbital separation a has been reduced to the point where the secondary's radius equals that of its Roche lobe (Eq. (4.3)). At this point we assume mass is lost from the secondary at a fixed constant rate (which we take to be $0.1 M_\odot\,\mathrm{yr}^{-1}$ in the present calculations) and inject it into the common envelope, where it begins the ballistic phase of its decent to meet the core of the primary. Following IVP we assume the stream begins its second, hydrodynamic phase of decent into the core when it reaches a radius of $r = 7.5 \times 10^{10}$cm. The entropy generated in the stream by the weak shocks it suffers while traversing the envelope/core is characterized by the parameter K_S, the ratio of adiabatic constants of the shocked and unshocked stream material

$$\left(\frac{P}{\rho^\gamma}\right)\Bigg|_2 = K_\mathrm{S}\left(\frac{P}{\rho^\gamma}\right)\Bigg|_1 \tag{5.3}$$

where γ is the adiabatic index of the stream material and subscript 1 refers to the top of the stream and 2 to the bottom. We use the functional form for K_S derived in IPS, and which summarizes the results of their calculations of the penetration depth of the stream

$$K_\mathrm{S} = 1 + k\eta_\rho^{\gamma-1}\left(\frac{M_\mathrm{int}}{M_\mathrm{ext}}\right)^2 \tag{5.4}$$

with $k = 0.1$ (corresponding to the structure of a $20\,M_\odot$ star). Here η_ρ is the ratio of central stream density to the density of the ambient medium, and M_int and M_ext the internal and external Mach numbers of the stream (i.e. velocities relative to the sound speed in the stream and the sound speed in the ambient medium, respectively). From the Bernoulli integral for the stream material, IPS derive an implicit relation between K_S and the relative penetration depth δ, their Eq. (27), which we solve for δ at each time step of the merger calculation to determine where in the primary to inject the mass from the secondary. The stream is assumed to carry with it specific angular momentum corresponding to the orbit of the secondary when it is injected.

5.3 Results and discussion

We start the primary on the ZAMS with $X = 0.70$ and $Z = 0.02$; the secondary at the start of the CE phase is assumed to be a normal, ZAMS star of mass $6\,M_\odot$, with the same initial abundances. The spiral-in phase begins immediately after the primary finishes core helium burning; during this phase we hold the frictional luminosity constant at $L_\mathrm{fric} = 4.0 \times 10^4\,L_\odot$. The secondary begins to transfer mass at radius

$r = 3.7 \times 10^{11}$cm. This mass initially travels as a ballistic stream (the details of which we do not calculate) until it reaches $r = 7.5 \times 10^{10}$cm. At this point the edge of the hydrogen exhausted core is located at $r = 5.5 \times 10^{10}$cm, and the edge of the helium exhausted core is at $r = 6.7 \times 10^{9}$cm. To avoid explosive hydrogen burning in the injection region (which our nuclear reaction network is not able to follow), we assume the injected material has constant average composition $X = 0.02$, $Y = 0.96$ throughout the merger. Fig. 5-1 illustrates the evolution of the primary from the ZAMS to the ignition of carbon in its core, and Fig. 5-2 shows the rotational evolution of the core regions of the primary during its slow merger with the secondary. There are several strong density gradients in the core, as evidenced by the sharp cutoffs in the angular momentum distribution corresponding to the hydrogen and helium burning shells. The injection of additional hydrogen into the hot, previously hydrogen exhausted region of the primary's core results in additional rapid nuclear burning at the site where the stream dissipates. This increased energy output, along with the increased hydrogen content in the region above it (which increases the opacity there) induces a convective region which extends to the edge of the hydrogen exhausted core. Shear-invoked turbulence also transports angular momentum inward from the deposition region until it reaches the edge of the helium exhausted core, where it is stopped by the increasing stratification.

The entire $6\,M_\odot$ mass of the secondary, which is completely disrupted during the merger, streams into the primary's core prior to the ignition of carbon. The average specific angular momentum of the hydrogen exhausted core of the merged star is $\langle j \rangle = 5.0 \times 10^{17}\,\mathrm{cm}^2\,\mathrm{s}^{-1}$. Near the CO core, $j \approx 10^{16} - 10^{17}\mathrm{cm}^2\,\mathrm{s}^{-1}$, a range of specific angular momentum which would support an accretion torus around the iron core once it collapses (see Chapter 6).

The single merged star ends it evolution as a red supergiant (Fig. 5-1). This might have been anticipated based on the ratio of its core to envelope mass at the end of the merger. The addition of the secondary's mass to its core increases this ratio relative to an isolated $26\,M_\odot$ star of the same age and composition, favoring a red supergiant envelope configuration.

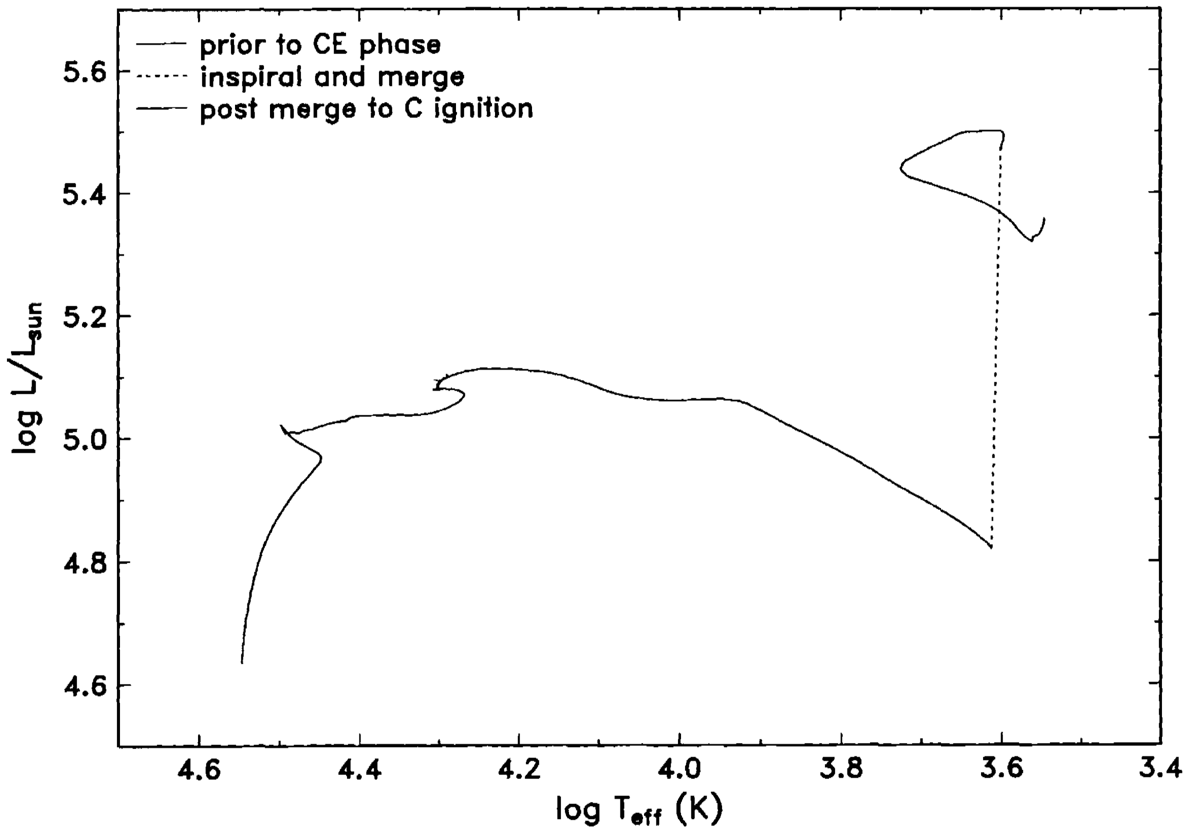

Figure 5-1: HR diagram showing the evolutionary track of a 20 $M_\odot$ star (the primary) undergoing merger with a 6 $M_\odot$ companion. The evolution from the ZAMS to just prior to the beginning of the common envelope phase is shown by the first solid line. The common envelope phase is assumed to commence after the primary has ended helium core-burning and ignited it in a surrounding shell, and is represented by the dotted line (spiral-in and merger details are not shown, for clarity). The post-common-envelope evolution until carbon burning is shown by the second solid line.

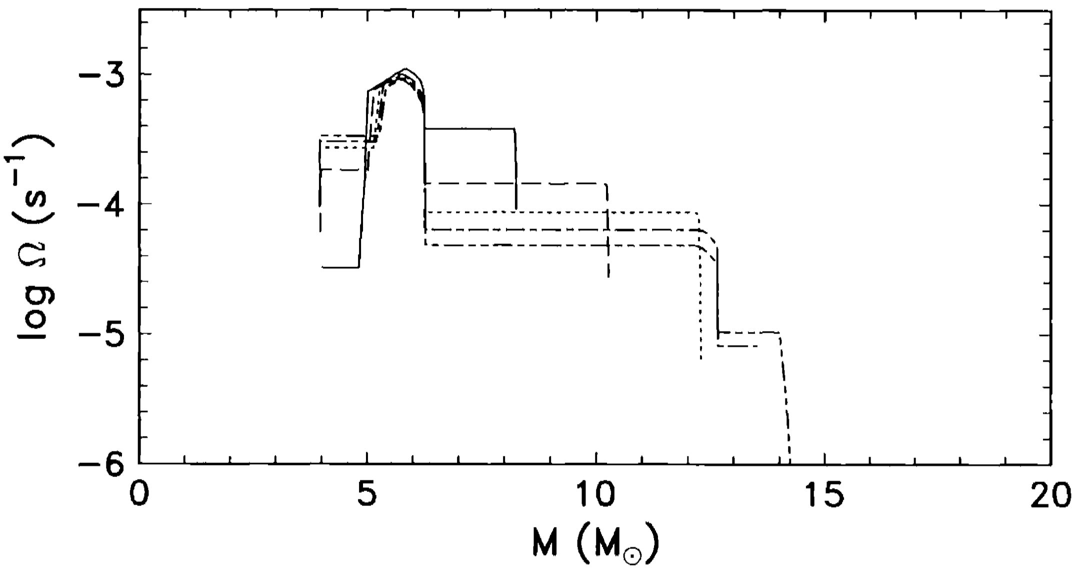

Figure 5-2: Angular velocity Ω as functions of enclosed mass for a selection of time points during the merge of a $20\,M_\odot$ star with its $6\,M_\odot$ companion. Note that the inward progress of the injected angular momentum is halted at the edge of the helium-exhausted core by the large molecular weight gradient there. A convective shell develops exterior to the radius to which the stream penetrates due to the concentrated nuclear burning there, which extends to the the edge of the hydrogen exhausted core.

Chapter 6

Stellar progenitors of gamma-ray bursts

Our understanding of so-called long ($t_{\mathrm{GRB}} > 2\,\mathrm{s}$)[1] gamma-ray bursts (GRBs)[2] has undergone a revolution in the past decade, driven primarily by new observational data which has been brought to bear on the problem. It is now widely accepted in the gamma-ray burst community that at least a subset of long gamma-ray bursts are likely generated within massive stars, either during their final evolutionary stages of core collapse or possibly as the result of their interactions with a compact companion (Fryer & Woosley 1998; Bethe & Brown 1998; Joss & Becker 2003). Several pieces of observational evidence support this contention, including the spatial association between GRBs and star-forming regions of faint galaxies undergoing star formation activity (Paczyński 1998; Bloom et al. 1998a), and the discovery of a standard gamma-ray burst energy which is very similar to the typical energy of a supernova (SN) explosion (Frail et al. 2001; Bloom et al. 2003).

The spatial and temporal association of the hyper-energetic supernova SN 1998bw (or hypernova, see Paczyński 1998; Mazzali et al. 2003) with the relatively weak

---

[1] t_{GRB} corresponds to the parameter t_{90} defined on the BATSE satellite GRB burst duration page (http://f64.nsstc.nasa.gov/batse/grb/duration) as the length of time over which a burst emits from 5% to 95% of its total measured counts; (see Fig. 1-4).

[2] See Chapter 1 for an overview of GRB phenomenology and theory. The progenitors of the population of so-called short GRBs (those with $t_{\mathrm{GRB}} < 1\,\mathrm{s}$) are currently still a mystery, primarily due to the lack of any observations to date of associated afterglows. In the present work we only consider the better-understood population of long gamma-ray bursts.

gamma-ray burst GRB 980425 is directly suggestive of a connection between the two events. Subsequent observations of several bursts with late-time, red "bumps" in their optical afterglows, similar to the light-curve of SN 1998bw – GRB 970228 (Reichart 1999; Galama et al. 2000), GRB 980326 (Bloom et al. 1999), GRB 011121 (Bloom et al. 2002), GRB 020405 (Price et al. 2003) – have served as additional evidence of a possible connection between the two phenomena. This connection has more recently been dramatically demonstrated by the unambiguous detection of a supernova light-curve bump and spectrum in the optical afterglow of GRB 030329 (Stanek et al. 2003).

Recent theoretical work on stellar central engines for gamma-ray bursts (MacFadyen & Woosley 1999; Aloy et al. 2000; Wheeler et al. 2000; Brown et al. 2000; van Putten 2001; Wang et al. 2001; van Putten & Levinson 2003; Zhang et al. 2003) suggests that to successfully launch a burst the stellar host must possess at least three ingredients:

- a large enough zero age main-sequence mass so that the eventual collapse of its core results in a central compact object which is a black hole and not a less massive neutron star (Brown & Lee 2004);
- sufficient angular momentum in its core to support a disk or torus around the collapsed central compact object (which is assumed to be a black hole for energetic reasons), but not so much angular momentum that the resulting disk/torus is too dispersed relative to the central object to allow efficient energy release on a sufficiently short time scale (MacFadyen & Woosley 1999; van Putten & Ostriker 2001);
- a hydrogen envelope which is not too massive and relatively compact (i.e., the star must be a blue supergiant rather than a red supergiant).

We will address these constraints in the context of our accretion and merger models in the remainder of this chapter. In § 6.1 we discuss theories of possible GRB central engines (all involving the formation of a rapidly rotating black hole and surrounding centrifugally supported torus) and, in light of these theories, examine the cores of our models, focusing particularly on the distribution of specific angular momentum and the implications for the formation of viable GRBs. In § 6.2 we consider the envelopes of our models and examine the possibility of a second interaction taking place in the binary system which may alleviate the problem of their massive envelopes.

6.1 Core angular momentum distribution

6.1.1 Central engine formation

The basic hypernova-microquasar model[3] (Paczyński 1998; MacFadyen & Woosley 1999; Wheeler et al. 2000; Brown et al. 2000) hypothesizes that the chain of events which leads ultimately to a GRB begins with the collapse of the central portion of a massive star's central iron core. If the surrounding layers of the core are sufficiently massive, the bounce of, and subsequent neutrino flux from, the hot protoneutron star newly created at the center of the star will be unable to reverse the infall of the overlying layers. The remainder of the star will remain gravitationally bound to the core and the nascent supernova explosion will fail. The accretion of the innermost, infalling layers of the core onto the central proto-neutron star will quickly increase its mass and promote its further collapse into a black hole.

If the star is non-rotating the remainder of its evolution might be relatively uninteresting from an observational point of view. In such a case the star's outer layers are expected to spherically accrete onto the black hole at its center on a time scale which depends on, among other things, the efficiency of photon or neutrino mediated energy transport in removing the energy of the infalling matter. The eventual outcome of this evolution for a single star is a silent, stellar-mass black hole. For a collapsed star with a companion, there is the possibility of an X-ray emission phase if the two stars are close enough to eventually interact and exchange mass.

The presence of angular momentum in the stellar core can, however, substantially alter this outcome. The central black hole which results from the collapse of a rapidly rotating core will be endowed with the angular momentum and rotational kinetic energy of the core material from which it forms. The rotational energy possessed by a stellar mass black hole formed in this fashion can be formidible if the black hole's angular momentum J is an appreciable fraction of the hole's "critical" angular momentum GM^2/c.

---

[3] Refer to Chapter 1 for definitions of these terms.

Material in the core's equatorial plane will, if also rotating sufficiently rapidly, encounter a centrifugal barrier barring its further inward progress during the collapse event. The resulting buildup of material forms a centrifugally supported disk or torus surrounding the central black hole. Preexisting magnetic fields in the collapsing core material will likely be magnified as this material is consolidated into the body of the torus; hence, the disk/torus system is likely to be strongly magnetized.

As the black hole/torus system forms at the center of the core, material near the rotation axis of the star with less angular momentum falls essentially unimpeded onto the poles of the black hole. This process clears the polar regions of the core (where the energy powering the jets is predominantly deposited) of material which could poison the incipient fireball with baryons were its density not so reduced. The torus and the core's essentially intact outer layers in the vicinity of the rotation axis can also provide a natural collimator for jets directed along this axis.

Both the torus and the Kerr black hole in this system possess large reserves of energy which can, in principle, be tapped by several mechanisms to power a gamma-ray burst.[4] A great deal of current research activity is focused on determining the details of some of these energy extraction/deposition processes. Some possibilities include neutrino annihilation, which occurs preferentially along the axis of symmetry (the rotation axis) of the accretion disk (Woosley 1993; MacFadyen & Woosley 1999) and which draws on the energy dissipated by the accretion disk (Popham et al. 1999), and various magnetohydrodynamic mechanisms, including a magnetic-field mediated extraction of rotational energy from the central black hole by the Blandford-Znajek (BZ) mechanism (Lee et al. 2000b), or others (see e.g. van Putten & Ostriker 2001; van Putten & Levinson 2003).

For illustrative purposes, we briefly consider the energetics and time scales associated with the BZ mechanism operating on a stellar mass black hole (see, e.g. Blandford & Znajek 1977; MacDonald & Thorne 1982; Lee et al. 2000b). The energy scale associated with the BZ mechanism is given by the rotational energy of the black hole; for a Kerr black hole of mass M, angular momentum J and dimensionless

---

[4] See Chapter 1 for an overview of several of these mechanisms.

rotation parameter $a = J/(GM^2/c)$ this energy is given by

$$\begin{aligned} E_{\rm rot} &= f(a)Mc^2 \, , \\ f(a) &= 1 - \sqrt{[1+(1-a^2)^{1/2}]/2} \, . \end{aligned}$$

A maximally rotating black hole with $a = 1$ thus has total rotational energy

$$E_{\rm rot,max} = 0.29Mc^2 = 5.2 \times 10^{53} \left(\frac{M}{M_\odot}\right) \, {\rm erg},$$

some fraction $\varepsilon \sim 0.5$ of which can be extracted by the BZ mechanism (where ε is the extraction efficiency). The time scale on which the BZ mechanism operates, and the associated maximum outgoing Poynting power it generates are given by

$$\begin{aligned} \tau_{\rm BZ} &= 2.7 \times 10^3 \left(\frac{B}{10^{15}{\rm G}}\right)^{-2} \left(\frac{M}{M_\odot}\right)^{-1} \, {\rm s} \\ P_{\rm BZ} &= 6.7 \times 10^{50} \left(\frac{B}{10^{15}{\rm G}}\right)^{2} \left(\frac{M}{M_\odot}\right)^{2} \, {\rm erg\,s^{-1}} \, , \end{aligned}$$

respectively. A stellar mass black hole threaded by a $\sim 10^{15}$ G external magnetic field anchored in a surrounding torus is therefore, in principle, able to provide via the BZ process a sufficient amount of energy over an appropriate interval of time to power a long GRB (see, however Livio et al. 1999). Note that the torus must survive its interactions with the black hole through this time interval in order to maintain the external magnetic field which enables the extraction of rotational energy from the hole (see Meszaros & Rees 1997; Lee et al. 2000a, for further discussion of these points).

6.1.2 Accretion and merger scenarios: final models

The amount and distribution of angular momentum in the core will have direct bearing on the success of such an accretion-driven explosion. The models presented in Chapters 4 and 5 have distributions of specific angular momentum at the onset of core carbon burning which reach a few 10^{16} cm^2 s^{-1} in the outermost portions of their helium cores. We assume that subsequent burning stages proceed so rapidly that angular momentum transport mechanisms across the core-envelope interface will be inefficient, and hence the total angular momentum content of the core will remain constant. The details of angular momentum distribution in the core are subject to change, however, due to, for example, the emergence of new convective burning shells during subsequent burning epochs. We therefore also investigate two possible limits of angular momentum redistribution in the core: (i) constant specific angular momentum, or (ii) constant angular frequency. Both limits assume the same total core angular momentum content: that contained by the core of the final model in each sequence.

Figures 6-1, 6-3, 6-5 and 6-7 show the final core angular momentum distributions for four of these sequences: those which contain the greatest amount of angular momentum in their cores at the onset of carbon burning. With pressure support removed, a ring of material with constant specific angular momentum j in the equatorial plane of the star becomes centrifugally supported against the (Newtonian) gravity of a central point mass m at a reduced radius,

$$r \sim \frac{j^2}{GM} \sim 2.5 \times 10^7 \left(\frac{j}{10^{17}\mathrm{cm}^2\,\mathrm{s}^{-1}} \right)^2 \left(\frac{M}{3\,M_\odot} \right)^{-1} \mathrm{cm}\,. \tag{6.1}$$

As long as an orbit of this radius is stable, a disk or torus would be expected to form nearby; however, if the new radius of the ring's orbit falls within the last stable orbit around the central black hole for material of this specific angular momentum, the material will be lost to the torus and will, instead, fall into the hole.

Assume that all the mass interior to the shell at interior mass coordinate m falls into the black hole, contributing both its mass and angular momentum to the hole. The upper and lower pair of thin, dotted lines in these graphs give the specific angular momentum of material in the marginally stable circular orbit for the two extreme states of black hole rotation: no rotation (Schwarzschild hole: $a = 0$), and maximum rotation (Kerr hole: $a = 1$), respectively.[5] Sandwiched between these limits is the curve (thick dashed-dotted line) giving the specific angular momentum of material in the last stable orbit about a rotating black hole with angular momentum J equal to that originally possessed by the material internal to mass shell m. The thick dotted

---

[5] Expressions for these quantities are given in, e.g. Bardeen et al. (1972)

line gives the corresponding value of the rotation parameter a for a black hole of mass m and angular momentum J.

As Fig. 6-1 indicates, the secondary star of sequence $A30p10$ ends it evolution with a distribution of angular momentum in its core ($m < 11.3\,M_{\odot}$) insufficient to support an accretion disk about a central black hole. The specific angular momentum of the surrounding envelope is sufficient to avoid direct collapse into the black hole; however these layers would be unlikely to form a disk sufficiently dense to drive an energetic release of disk binding energy (MacFadyen & Woosley 1999; Aloy et al. 2000) during accretion into the central black hole. A black hole formed out of the central $\sim 2\,M_{\odot}$ of the core would have $a \sim 0.2$, with correspondingly small rotational energy, also probably insufficient to power a burst (see § 6.1.1).

Fig. 6-2 presents the same set of curves for the final model of sequence $A30p10$, this time however corresponding to two alternative final specific angular momentum distributions: j constant (top panel), and Ω constant (bottom panel), both assuming that the total angular momentum content of the core, $J_{\rm core}$ is conserved during the redistribution. Presumably, unspecified mechanism(s) have operated in the core following carbon ignition but prior to the final stellar core collapse, resulting in these two limiting distributions.

The j constant limit enhances the spin of the centermost regions of the core, at the expense of those layers farther out. As a result, a maximally rotating Kerr black hole would form from the inner $\sim 3\,M_{\odot}$ of material, while core material outside of this region would not achieve stable orbits around the hole and would likely be drawn into it.

The Ω constant limit removes too much angular momentum from the central regions, resulting in a core which provides very little rotational support for its mass, and hence which is a less likely GRB progenitor.

The greater core angular momentum content of the final model of another LMS accretion case, sequence $A40p10$ (Fig. 6-3), allows it to easily meet the stability requirements for orbits surrounding the central black hole and form a rotationally supported torus within the core in contrast to the previous case. In fact, the specific angular momentum in this case may be too large to form the tight, dense disk necessary for effective accretion rates in central engines driven by the gravitational binding

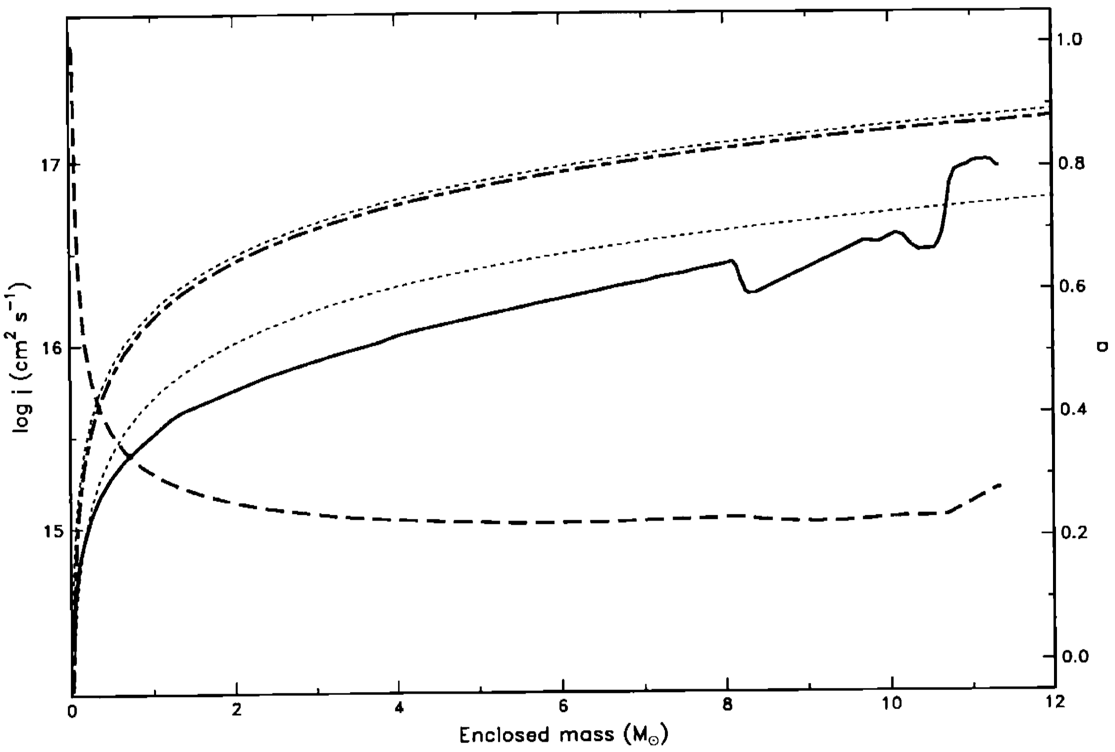

Figure 6-1: Angular momentum distribution in the core of the final model of sequence $A30p10$ (just prior to core carbon ignition), as a function of enclosed mass. The thick solid line shows the actual specific angular momentum distribution, j, in the equatorial plane of the model. The specific angular momenta of mass elements in marginally stable circular orbits around a central black hole of varying mass and angular momentum are also shown for reference: $j_{\mathrm{ms},0}$ is the specific angular momentum necessary for a mass element to settle into the last stable orbit about a non-rotating (Schwarzschild) black hole, with mass equal to the enclosed mass (upper thin dotted line); $j_{\mathrm{ms},1}$ is the corresponding quantity for a maximally rotating (Kerr) black hole, with rotation parameter $a = 1$ (lower thin dotted line); $j_{\mathrm{ms},a}$ corresponds to a rotating black hole with mass and angular momentum equal to that of the enclosed mass (thick dash-dotted line). The thick dashed line gives the rotation parameter a corresponding to $j_{\mathrm{ms},a}$ (scale on the right). The specific angular momentum of most of the core in this case never reaches the level of the lowest marginally stable orbit, therefore a centrifugally supported torus is not expected to form near the central black hole.

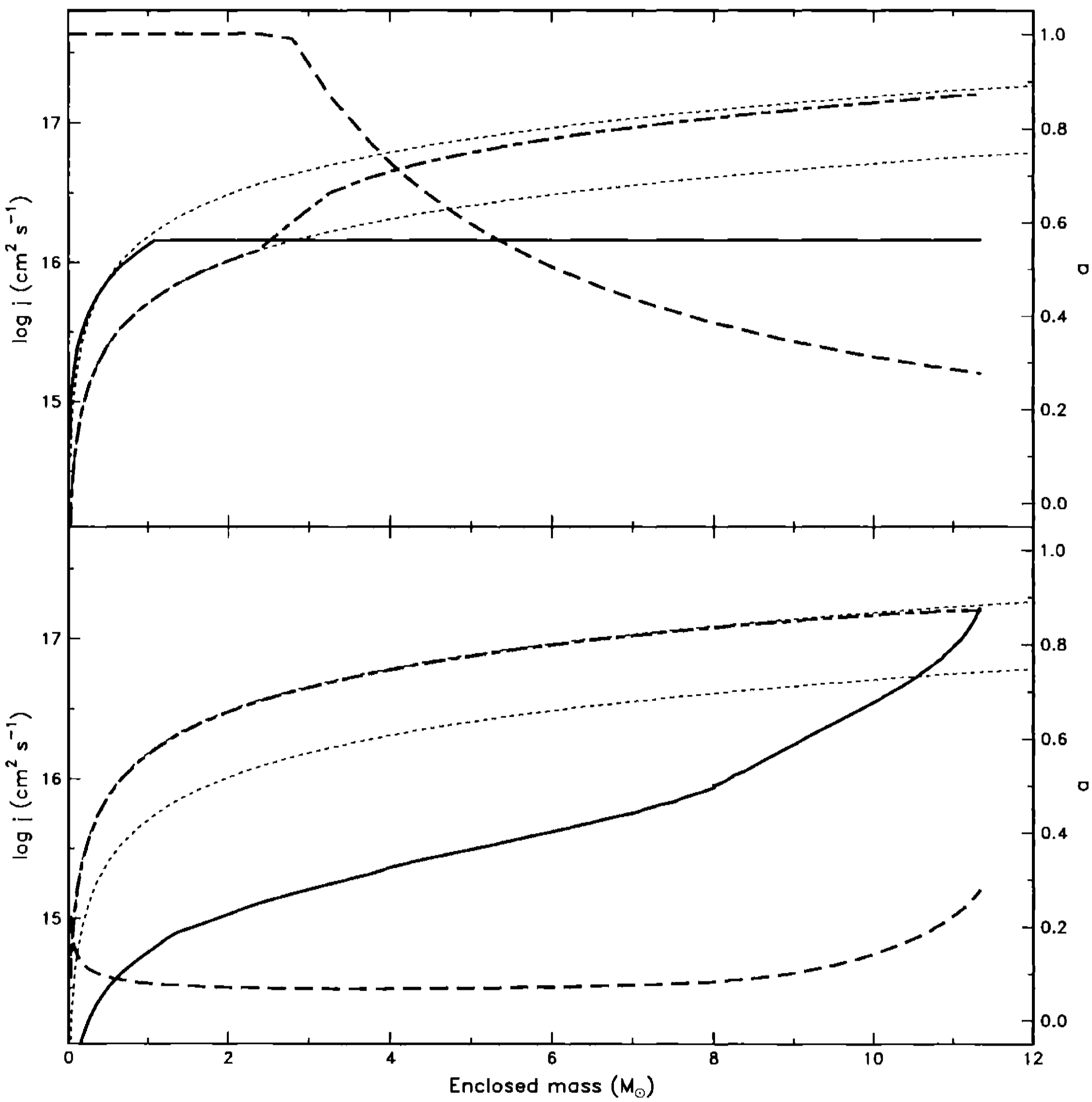

Figure 6-2: Redistributed core angular momentum distributions for the final model of sequence *A*30*p*10 versus enclosed mass. The top panel corresponds to the case of constant specific angular momentum (solid line) through most of the core ($m > 1\,M_\odot$), assuming that the total angular momentum content of the core is unchanged by the redistribution of j. The central region ($m < 1\,M_\odot$) is assumed to form a vortex core which rotates as a solid body. The other curves are defined in the caption to Fig. 6-1. The bottom panel shows the alternative case in which the entire core is assumed to rotate as a solid body, again keeping its total angular momentum content constant. A nearly maximally rotating Kerr black hole would result from the collapse of the innermost $\sim 3\,M_\odot$ of the constant j model (top panel).

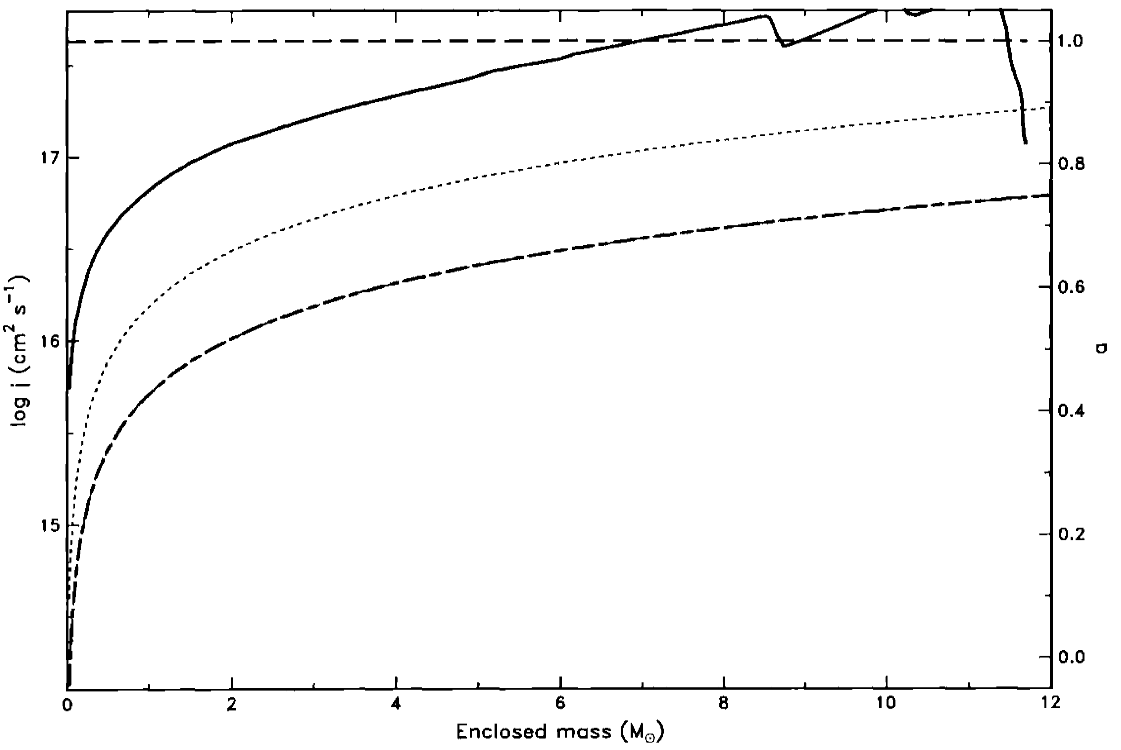

Figure 6-3: Core angular momentum distribution for the final model of *A*40*p*10 versus enclosed mass. See the caption of Fig. 6-1 for further description.

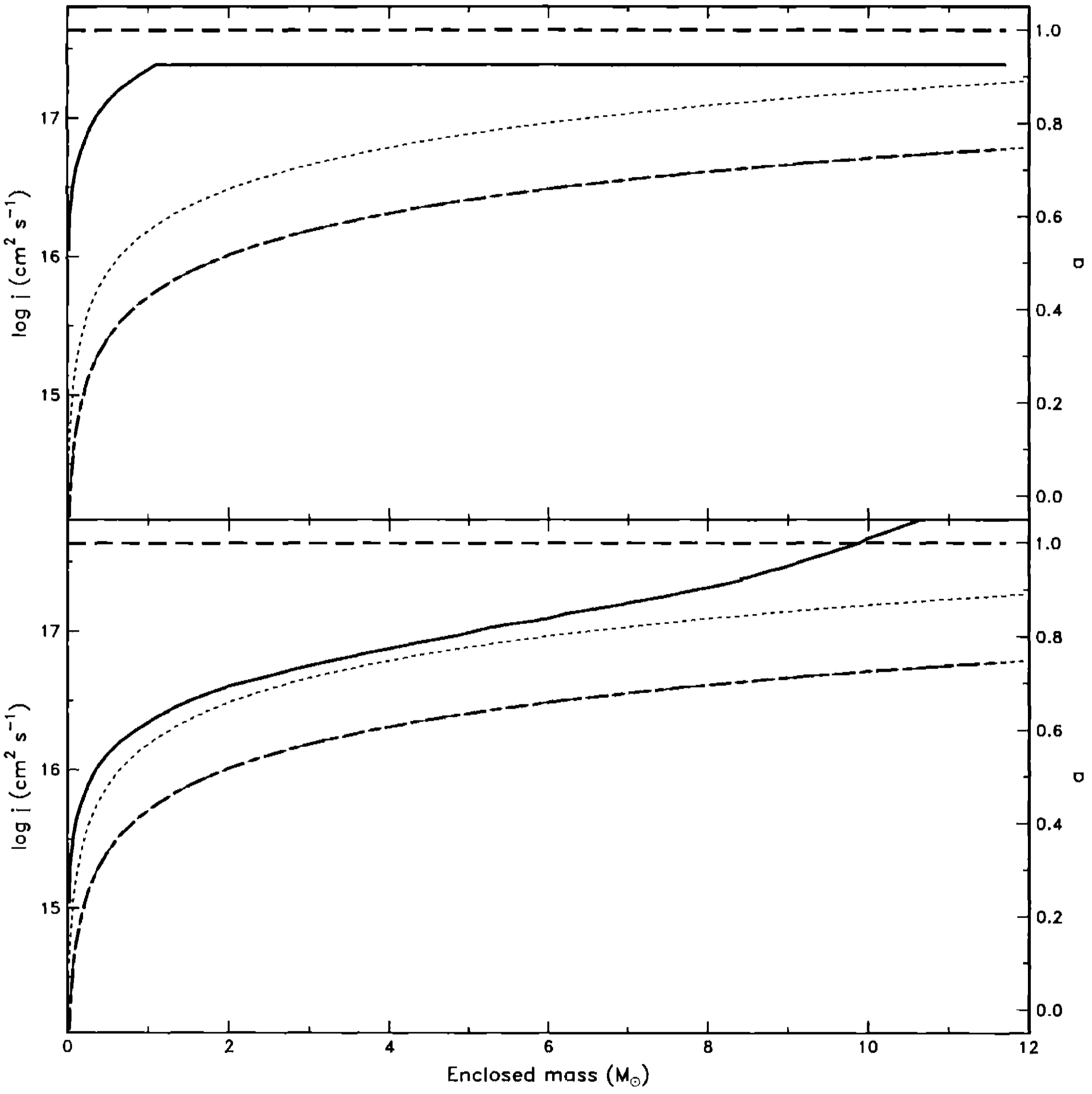

Figure 6-4: Angular momentum distributions corresponding to constant specific angular momentum (top) and angular velocity (bottom) in the core of the final model of sequence *A*40*p*10, versus enclosed mass. See the caption of Fig. 6-2 for more detailed description.

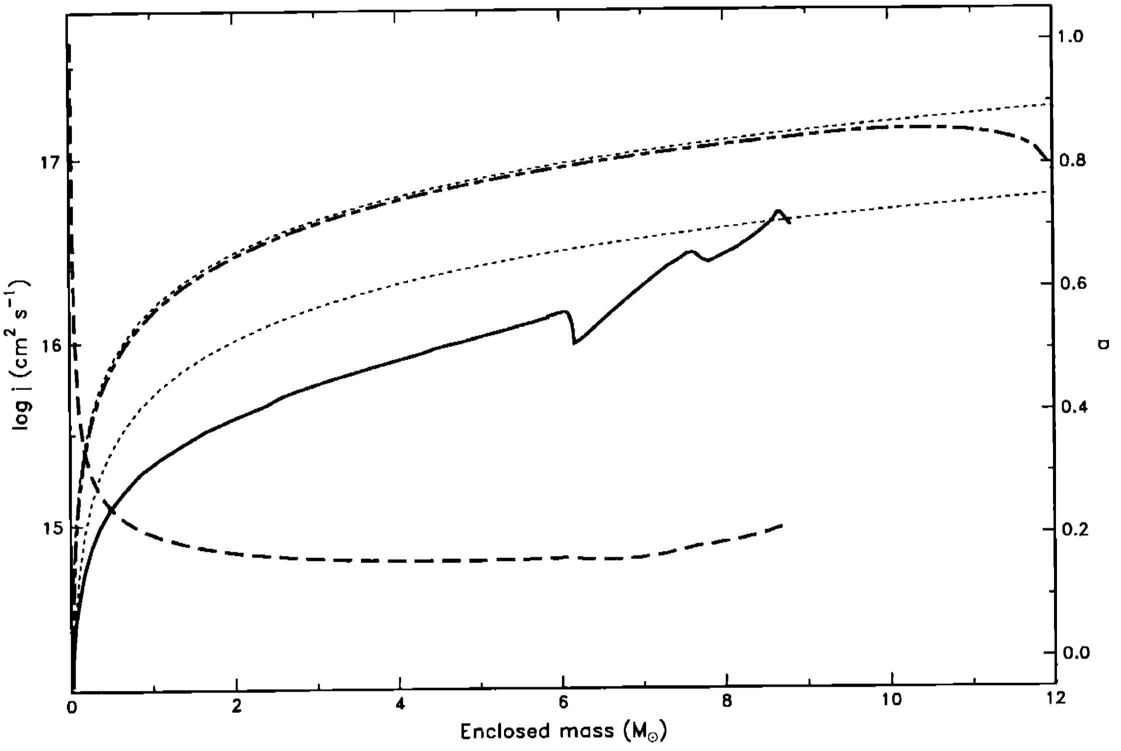

Figure 6-5: Core angular momentum distribution for the final model of $B31p10$ versus enclosed mass. See the caption of Fig. 6-1 for further description.

energy of the accretion disk. MacFadyen & Woosley (1999) argue that material with $j > 2 \times 10^{17}\,\mathrm{cm}^2\,\mathrm{s}^{-1}$ will be halted by centrifugal force outside of $\sim$ 1000 km (see Eq. (6.1)) in a region of inefficient neutrino cooling, resulting in a less tightly bound disk and lower accretion rate. As can be seen from this figure, a black hole formed from the collapse of any portion of the core will be in a state of near-maximal rotation ($a = 1$). The final model of $A40p10$ would consequently be expected to develop a rapidly rotating central black hole, which could power a GRB by MHD processes.

The core of the final model of sequence $B31p10$ (early post-main-sequence accretion with IGW angular momentum transport across the core-envelope interface), Fig. 6-5, would form a moderately rotating black hole, $a \sim 0.2 - 0.3$, lacking a surrounding torus.[6]

---

[6] And ignoring any material which might accrete inward from the surrounding envelop, if any remains by the time of core collapse.

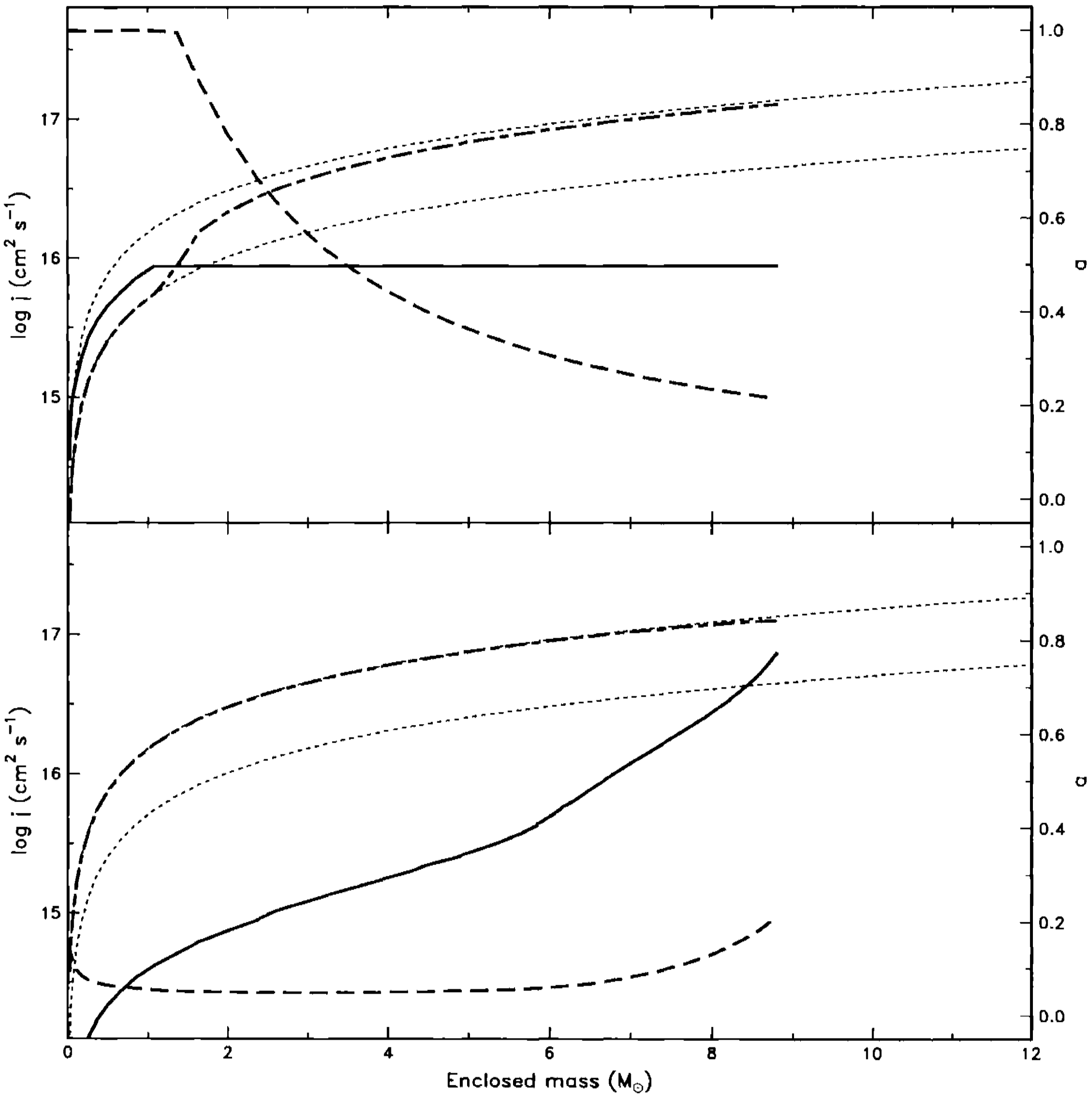

Figure 6-6: Angular momentum distributions corresponding to constant specific angular momentum (top) and angular velocity (bottom) in the core of the final model of sequence $B31p10$, versus enclosed mass. See the caption of Fig. 6-2 for a more detailed description.

The total angular momentum transferred to the core is reduced in this sequence by two factors: the contraction of the core at the end of hydrogen burning, and the evolutionary stage (helium core burning) during which angular momentum transfer across the core-envelope interface occurs. The contraction reduces the core's moment of inertia to $I_{core,He}$ from its larger value during core hydrogen burning, $I_{core,H} > I_{core,He}$. The helium core and its surrounding convective hydrogen burning shell are brought into corotation during core helium burning by the inward transport of angular momentum from the latter to the former. Roughly $\sim I_{core,He}\Omega_c$ in angular momentum is added to the core during this process, bringing the core into corotation with the burning shell at the common angular frequency Ω_c.

A transfer from envelope to core which occurs earlier, e.g. near the end of core hydrogen burning, and which brings both into corotation with the same angular frequency Ω_c would require a greater amount of angular momentum, in the ratio of the two cores' moments of inertia: $I_{core,H}/I_{core,He} \sim 10^{55.9}/10^{54.6}$. If this additional angular momentum were distributed uniformly in the core of the model, j would shift upward by ~ 1.3 in Fig. 6-5. The core in this case would form a rapidly rotating black hole and a viable surrounding torus. This scenario is similar to the late main sequence cases considered above, which differ, however, in having systematically larger core masses due to the rejuvenations they experience on the main sequence.

Fig. 6-7 show the same quantities for the merger sequence of Chapter 5. In this case the collapse of the central portion of the core would yield at least initially a non-rotating black hole, due to the absence of angular momentum within the inner $\sim 4\,M_\odot$ of the final model of this sequence. Material outside this mass shell (the edge of the helium-exhausted CO core) rapidly increases in specific angular momentum. The collapse or fallback of $\sim 1\,M_\odot$ of this mass into the black hole will quickly bring it into a state of maximal rotation (dotted curve where $a = 1$). Most of the material outside of the CO core has more than enough angular momentum to support an accretion disk outside of the $\sim 5\,M_\odot$ black hole.

We conclude that, of the models presented in Chapters 4 and 5, two of them – the late main sequence, slow accretor $A40p10$, and the merged star resulting from the common envelope evolution of a $20\,M_\odot$ primary and $6\,M_\odot$ secondary – have core angular momentum distributions which favor the formation of tightly bound accretion

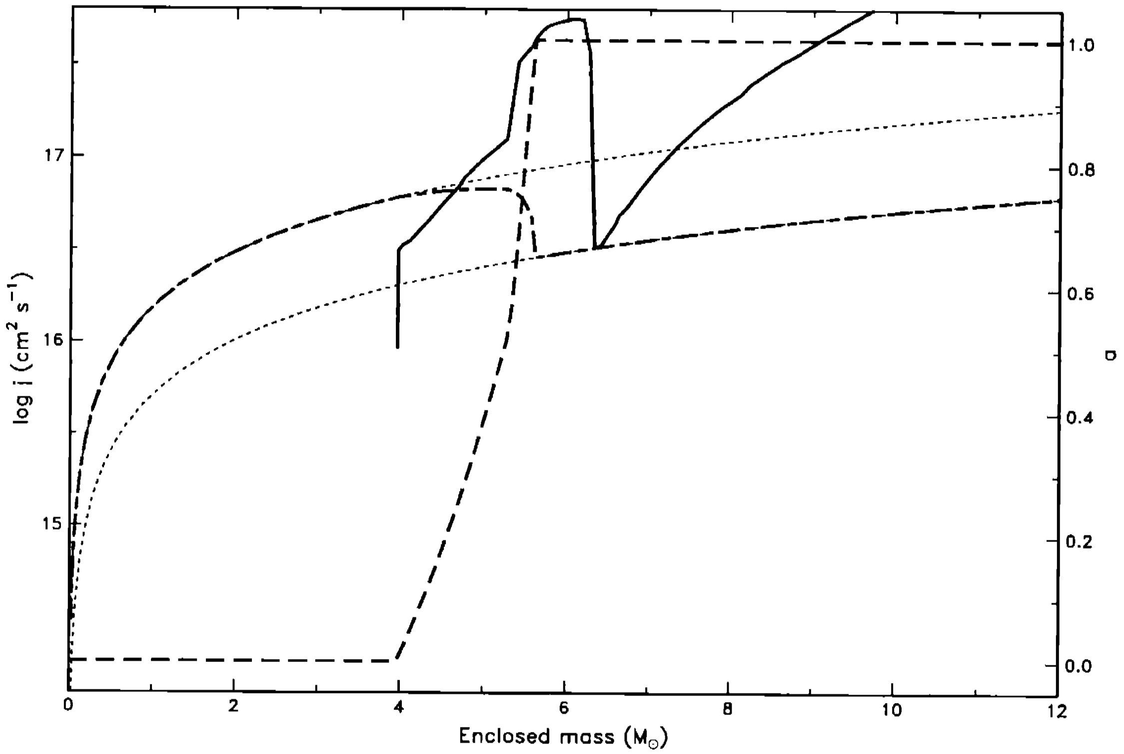

Figure 6-7: Core angular momentum distribution for the final model of the merger sequence of Chapter 5. See the caption of Fig. 6-1 for further description.

disks around their central compact objects. We would not expect such an accretion disk to form in the remainder of our models (although some sort of disk is likely to form, due to the large angular momentum content in the envelopes of all models), primarily due to lack of sufficient angular momentum in their cores at the end of their lives. Whether the two models with favorable core angular momentum distributions can succeed in generating a gamma-ray burst depends additionally on the state of their envelopes at the time of core collapse. We will address this issue in the following section.

6.2 Envelope properties

Current theories of gamma-ray burst production via the action of a relativistic fireball are relatively insensitive to the specific mechanisms of fireball initiation; all that

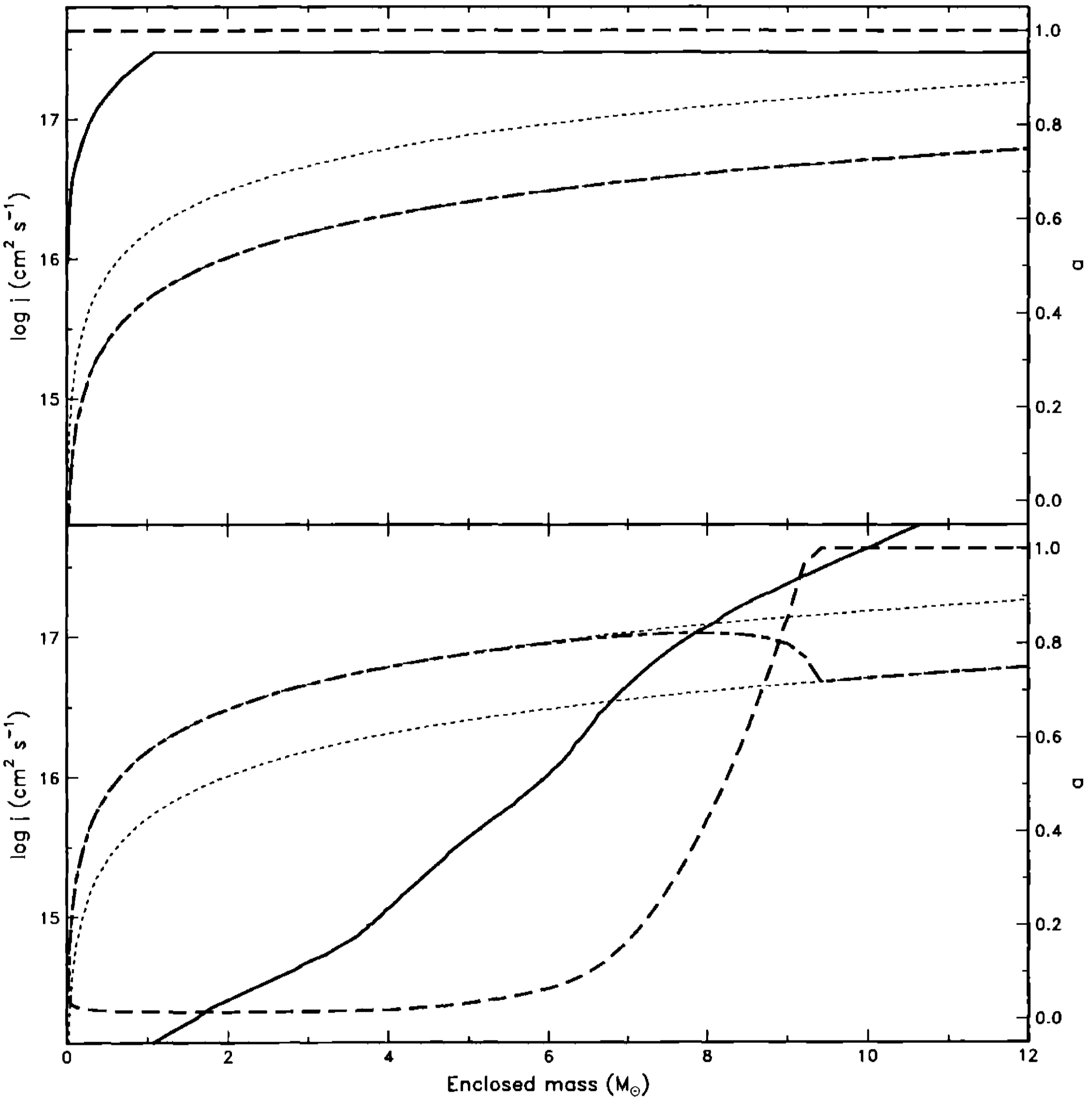

Figure 6-8: Angular momentum distributions corresponding to constant specific angular momentum (top) and angular velocity (bottom) in the core of the final model of the merger sequence, versus enclosed mass. See the caption of Fig. 6-2 for more detailed description.

matters is that a large amount of energy is deposited into a small spatial volume over an interval of time defining the duration of the burst. Given a region of space with such a high-energy density, theory predicts that a relativistic $e^{\pm}$ and γ fireball must inevitably arise. This fireball will rapidly expand, converting its internal energy into the kinetic energy of a (presumed small but necessarily nonzero) baryon component and reaching a bulk Lorentz factor $\Gamma \sim 100$[7] (see Mészáros 2002, for a general review of the theory of gamma-ray bursts). The kinetic energy of the expanding fireball/jet is eventually reconverted into the nonthermal photons of the gamma-ray burst by synchrotron radiation from internal shocks in the non-uniform outflow. The afterglow in X-ray, optical, and radio wavelengths is thought to be produced later, by external shocks created when the flow plows into, and is decelerated by, a significant amount of mass surrounding the site of the burst. For stellar progenitors of GRBs, the jetted output of the central engine will encounter the circumstellar mass ejected from the star in the form of a stellar wind during its prior evolution, and will there be decelerated to form the burst afterglow. The gamma-ray burst and afterglow both occur many stellar radii away from the progenitor.

Several conditions must be satisfied in order that the jet, which ultimately forms the gamma-ray burst and afterglow, can escape its place of birth in the core of the star. The jet must contain some baryons in order to convert its energy into the kinetic energy of relativistic expansion, but not be so laden with baryonic matter that it cannot achieve a sufficiently high bulk Lorentz factor Γ to produce a burst. A jet/fireball with energy E_j much larger than the rest mass energy of its baryon content M_b, $\eta = E_j/M_b c^2 \gg 1$, will convert most of this energy into kinetic energy of its bulk motion as it accelerates, acquiring a final Lorentz factor $\Gamma \sim \eta$. However, in order to overcome the compactness problem and produce a viable burst of gamma-ray photons, the jet must have $\Gamma > 100$ (see, e.g., Rees & Meszaros 1992). This places a stringent upper limit on the baryon content of the jet:

$$M_b \approx 10^{-5}\, M_{\odot} \left(\frac{E_j}{1.8 \times 10^{51}\,\mathrm{erg}} \right) \left(\frac{\eta}{100} \right)^{-1} .$$

The jet must be able to penetrate the envelope of the star without acquiring a large

---

[7] Collimation of the energy output doesn't alter the general outlines of this evolution in any significant way.

baryon load and within the lifetime of the central engine which is generating it. If the envelope is too massive, the jet will have to push aside a large amount of matter in traversing it in order to maintain its small baryon load, potentially dissipating most of its energy before it reaches the surface and can begin its hyper-relativistic expansion. If the envelope is too extended, the jet will lose its energy input from the central engine prior to breaking free at the surface, and again it will dissipate in the envelope.

6.2.1 Envelope mass

In order to break free from the star, two jets each with (half) opening angle θ_o must push aside an amount of mass $\sim M\theta_o^2/2$ where M is the total mass of the star outside the generation region for the jet. This material will acquire a velocity $\sim fc$ where f is 0.01 to 0.1 (MacFadyen & Woosley 1999) as it is being displaced from the path of the jets, corresponding to kinetic energy

$$E_p = \frac{f^2}{2}\left(\frac{\theta_o^2}{2}\right)Mc^2 = 3.6 \times 10^{51}\left(\frac{f}{0.1}\right)^2\left(\frac{\theta_o}{0.2}\right)^2\left(\frac{M}{20\,M_\odot}\right)\text{erg.} \tag{6.2}$$

Depending on the properties of the central engine (particularly the available energy reservoir) this energy could constitute a significant fraction of the total energy released during the explosion. In such a case, the energy remaining to the jet will be insufficient to power its relativistic expansion.

Our accretion-produced secondary models are characterized by relatively massive envelopes compared to single stars of similar masses. This is a direct consequence of the accretion event: the added mass, while building up and maintaining a large reservoir of angular momentum in the envelope, contributes to the substantial hydrogen rich envelope remaining after stellar wind loses. The three accretion models with maximum core angular momentum considered above have hydrogen envelopes ranging from $13.9\,M_\odot$ to $21.2\,M_\odot$ (see Table 4.1), which amount to a significant barrier which must be overcome by the jets to generate a successful gamma-ray burst.

E_p, however, is typically greater than the envelope binding energies of our stars, so the injection of this amount of energy along the rotation axis of the star might be expected to drive a supernova-like explosion once the displaced material reaches the equatorial plane and impacts material from the oppositely directed jet there (see Mészáros & Rees 2001; Aloy et al. 2000, for further discussion and for possible observational consequences of the jet's traversal of the stellar envelope).

6.2.2 Envelope extent

The hydrogen envelope surrounding the core must be relatively compact so that a hyper-relativistic jet can successfully burrow through it while the engine which generates it remains active ($\sim 10 - 100\,\mathrm{s}$). A jet leaving the helium core and entering the relatively low density environment of the hydrogen envelope is expected to rapidly accelerate to relativistic velocities (Mészáros & Rees 2001). The time required to cross the envelope is given by $t_H \approx r_H/c = 330 r_{H,13}\,\mathrm{s}$, where $r_{H,13} \times 10^{13}\,\mathrm{cm}$ is the radius of the envelope. The most compact envelope in our models has radius $r_{H,13} = 0.76$ with a corresponding crossing time of $\sim 230\,\mathrm{s}$. Only the most long-lived central engines will be able to power the jet for the required interval of time.

Interestingly, all cases to date in which a hypernova has been observed to follow a GRB (most prominently, GRB-980425/SN-1998bw and GRB-030329/SN-2003dh) the hypernova has been classified as Type Ic, indicating that no observational signatures of hydrogen or helium are present in its spectrum (Podsiadlowski et al. 2004; Nomoto et al. 2003; Kawabata et al. 2003). This implies that, in addition to lacking a hydrogen envelope of any significant mass, at least this class of GRB progenitors has also lost a large fraction of the helium rich shell surrounding the core; i.e. the progenitor is essentially a bare carbon-oxygen (CO) star. Recent calculations of the propagation of a hyper-relativistic jet through the envelope of a massive star (Zhang et al. 2003; Wang & Wheeler 1998) aren't so demanding of the structure of the progenitor; most assume the progenitor is a Wolf-Rayet star (i.e. a massive helium star) which has lost most of its hydrogen envelope prior to core collapse. Assuming that all long GRB are generated by progenitors like those which are responsible for the SN/GRBs that have been observed to date, the current observational results apply an additional constraint: a successful GRB progenitor might not be allowed to even possess a helium shell of any significance atop its CO core (Podsiadlowski et al. 2004). We consider some possible implications of these results in the following section.

6.2.3 Ejection via common envelope episode

As a result of the first mass transfer episode experienced by the systems considered in the present work, the secondary acquires a substantial hydrogen rich envelope by accretion from the primary. Only a portion of this envelope is lost by the secondary via a stellar wind as it continues its evolution to the point of core collapse. As discussed in § 6.2, such a massive, baryon rich envelope will effectively smother any energetic phenomena occuring in the core region which it surrounds, dissipating the input energy which might otherwise generate a relativistic outflow and GRB. This energy will eventually escape from the star over a longer time-scale via alternative routes, such as kinetic energy of envelope expansion and/or longer wavelength radiation. The resulting energetic display might appear to observers as a hypernova, X-ray flash, or even a Type-II supernova. As discussed by, e.g., MacFadyen & Woosley (1999); Mészáros & Rees (2001); Waxman & Mészáros (2003), a hydrogen envelope of mass greater than a few $M_{\odot}$ surrounding the hydrogen exhausted core, and more extended than a typical blue supergiant ($\sim 10^{11}\,\mathrm{cm}$) is expected to be sufficient to choke off any nascent GRB explosion generated in the core of the star. Our secondaries end their lives with much more massive hydrogen envelopes than this: from Table 4.1 the late main-sequence accretors typically have envelopes of more than $10\,M_{\odot}$, while secondaries which begin accreting mass after they leave the main sequence end up with even more massive envelopes, $\sim 18.6\,M_{\odot}$ and up.

In the present section we consider the possibility of a second interaction taking place between the components of the binaries considered in the present work. For appropriate orbital parameters, the expansion of the secondary as it nears the end of its evolution can result in the generation of a common envelope which subsequently will be ejected from the system by the spiral-in of the embedded primary. Such an event could be effective in removing both the secondary's massive hydrogen envelope, as well as the helium shell underlying it and enveloping the CO core. If these layers are lifted from the secondary star over a sufficiently short interval of time, angular momentum transport mechanisms will be too slow to operate, and the resulting bare C/O core will retain essentially all of its angular momentum. The resulting object might constitute a viable GRB progenitor of the observed type, that is, of Type Ic, by definition exhibiting no evidence of hydrogen or helium in its spectrum.

A common envelope phase has been implicated in the the evolution of a variety of binary systems (Iben & Livio 1993), including cataclysmic variables (Paczyński 1976; Meyer & Meyer-Hofmeister 1979; Taam et al. 1978), systems containing a compact stellar remnant (a neutron star or black hole) in close orbit with a nondegenerate star (Podsiadlowski et al. 2003; Brown et al. 1999; van den Heuvel 2001), and double neutron star systems (Ivanova et al. 2003). A common envelope is formed when the mass-losing star (the mass donor, which in our case is the secondary star of the system) overflows its critical lobe and begins transferring matter to its companion (the primary in the systems we consider) too rapidly for the companion to assimilate. The proferred matter piles up around the overwhelmed companion, quickly filling its own critical lobe and consequently expanding to engulf both stars (see also Chapter 5). Within the common envelope, the core of the donor is orbited by the companion star, which experience dynamical friction with the non-corotating envelope, thus losing angular momentum and spiralling into a tighter orbit. Some fraction of the orbital energy so liberated is absorbed by the common envelope, which can be unbound from the system in the process. Two outcomes are possible: either the envelope is lost before the inspiralling companion overflows its own critical lobe, in which case the (essentially unaltered) companion ends up in a tightened orbit about the core of the donor; or at some point the companion begins contributing its own mass to the envelope, in which case a merger of the two star is expected (see, e.g. Ivanova et al. 2002, and Chapter 5).

The formation of a common envelope is favored when the mass of the donor exceeds that of the companion by more than approximately a factor of two.[8] By definition, our systems begin their lives with $M_1 > M_2$. During the first mass transfer episode the primary overflows its critical lobe and transfers mass to the secondary, which accretes some fraction and quickly becomes the more massive of the two stars. $q = M_2/M_1 > 1$ after this phase, and becomes larger as the evolution proceeds. Consider, for example, sequence $A30p10$ (see Table 4.1). From Fig. 4-1, assuming conservative mass transfer ($\beta = 1$), the primary and secondary end the accretion phase with masses $M_1 = 16\,M_\odot$ and $M_2 = 35\,M_\odot$, respectively.[9] The secondary goes on to lose an additional $9.8\,M_\odot$

---

[8] This ratio is highly dependent on the evolutionary states of the envelopes of both the donor and the companion; see Podsiadlowski et al. (1992); Pfahl et al. (2002) for further discussion.

[9] For $\beta < 1$ the primary will end up with even less mass; see Fig. 4-1.

to a rotationally enhanced stellar wind and end its evolution with a final mass of $M_2 = 25.2\,M_\odot$. In contrast to the secondary, we do not follow the detailed evolution of the primary in our calculations; however, it will also suffer wind mass loss, and thus will approach its own core collapse with a mass significantly less than the $16\,M_\odot$ it retained at the close of the first transfer phase. Making the crude approximation that the wind mass loss rate scales as the star's mass (and ignoring any rotational enhancement of the wind mass loss rate), the primary would be expected to lose roughly $\sim 4\,M_\odot$ during the remainder of its evolution. If the primary undergoes core collapse prior to the secondary, the primary's compact remnant, likely a neutron star (see Brown & Lee 2004, for a discussion of the effects of mass loss on production of neutron stars and black holes in core collapse supernovae), will have a mass of $\sim 1.4\,M_\odot$ (or somewhat larger if the remnant is a black hole). In this case, the mass ratio $q \gg 2$. Conversely, if the primary is still evolving at the time of the secondary's core collapse we expect $q \sim 2$ at a minimum. Similar arguments hold for the other sequences considered in Chapter 4.

Thus, if the secondary overflows its own critical lobe at some point in its evolution following the first mass transfer phase but preceeding its final core collapse, a second interaction between the stars is expected, in the form of a common envelope phase. The complex, hydrodynamic details of common envelope evolution are currently poorly understood, although some pioneering calculations of the processes involved have been performed (Rasio & Livio 1996). Consequently, we utilize the commonly used energy argument of, e.g., Dewi & Tauris (2000) in order to roughly estimate the outcome of this phase. We compare the energy lost to the orbit as it tightens during the primary's in-spiral to the binding energy of the secondary's envelope. Some fraction of the orbital energy so liberated is dissipated in the envelope; we assume the envelope becomes unbound when the two energies are comparable. From the models derived in Chapter 4, we compute the binding energy of the secondary's envelope (either hydrogen or helium), which can be expressed in terms of the dimensionless parameter λ:

$$E_{2,bind} = -\int_{M_{2,core}}^{M_2} \frac{Gm\,dm}{r(m)} = -\frac{GM_2 M_{2,\mathrm{env}}}{\lambda r_{2\mathrm{L}} a_i} \;,$$

where $M_{2,core} + M_{2,\mathrm{env}} = M_2$, and the Roche lobe radius of the secondary is given in terms of the primary-secondary orbital separation a_i by $R_{L2} = r_{2\mathrm{L}} a_i$. The energy lost from the orbit as the primary spirals from radius a_i (external to the envelope of the primary) to radius a_f (after the envelope has been lifted away) is given by

$$\Delta E_{orb} = -\frac{G M_{2,\mathrm{core}} M_1}{2a_f} + \frac{G M_2 M_1}{2a_i} .$$

Setting $E_{2,bind} = \eta_{\mathrm{CE}} \Delta E_{orb}$, where η_{CE} is the fraction of the orbital energy which is effective in unbinding the envelope, yields

$$\frac{a_f}{a_i} = \frac{M_{2,\mathrm{core}} M_1}{M_2} \left[M_1 + \frac{2 M_{2,\mathrm{env}}}{\eta_{\mathrm{CE}} \lambda r_{2\mathrm{L}}} \right]^{-1} . \tag{6.3}$$

This gives the final orbital separation as a fraction of the initial separation assuming that a fraction η_{CE} of the dissipated orbital energy is just sufficient to unbind the envelope of the secondary.

Fig. 6-9 shows the envelope binding energy as a function of enclosed mass for two representative secondaries, a late main sequence (LMS) and an early post main sequence (EPMS) accretor, respectively. As these graphs show, the binding energy of the envelope increases rapidly as one passes from the hydrogen rich envelope through the helium shell and into the carbon-oxygen core of the star. Fig. 6-9 also shows that the envelope of the EPMS secondary is more tightly bound overall than that of the LMS secondary. This is a consequence both of the former's greater mass as well as of its smaller radius relative to the latter. It is also reflected in the relative positions of the two stars in the HR diagram (see, e.g. Fig. 4-3 and Fig. 4-20).

We assume the secondary just fills its critical lobe (which we approximate by the Roche lobe) at the end of the evolutionary sequences computed in Chapter 4. The radius R_2 of the secondary therefore imposes a size scale on the system: $R_{2L} = R_2$, and thus $a_i = R_2/r_{2\mathrm{L}}$. For initial separations smaller than this, the secondary will overflow its Roche lobe earlier in its evolution; however, the results presented below will still apply, only at the earlier time. We take the common envelope efficiency parameter $\eta_{\mathrm{CE}} = 1$ in all cases.

Fig. 6-10 shows the result of a common envelope phase for the terminating secondary of sequence $A30p10$, and for a range of possible primary masses (the x co-

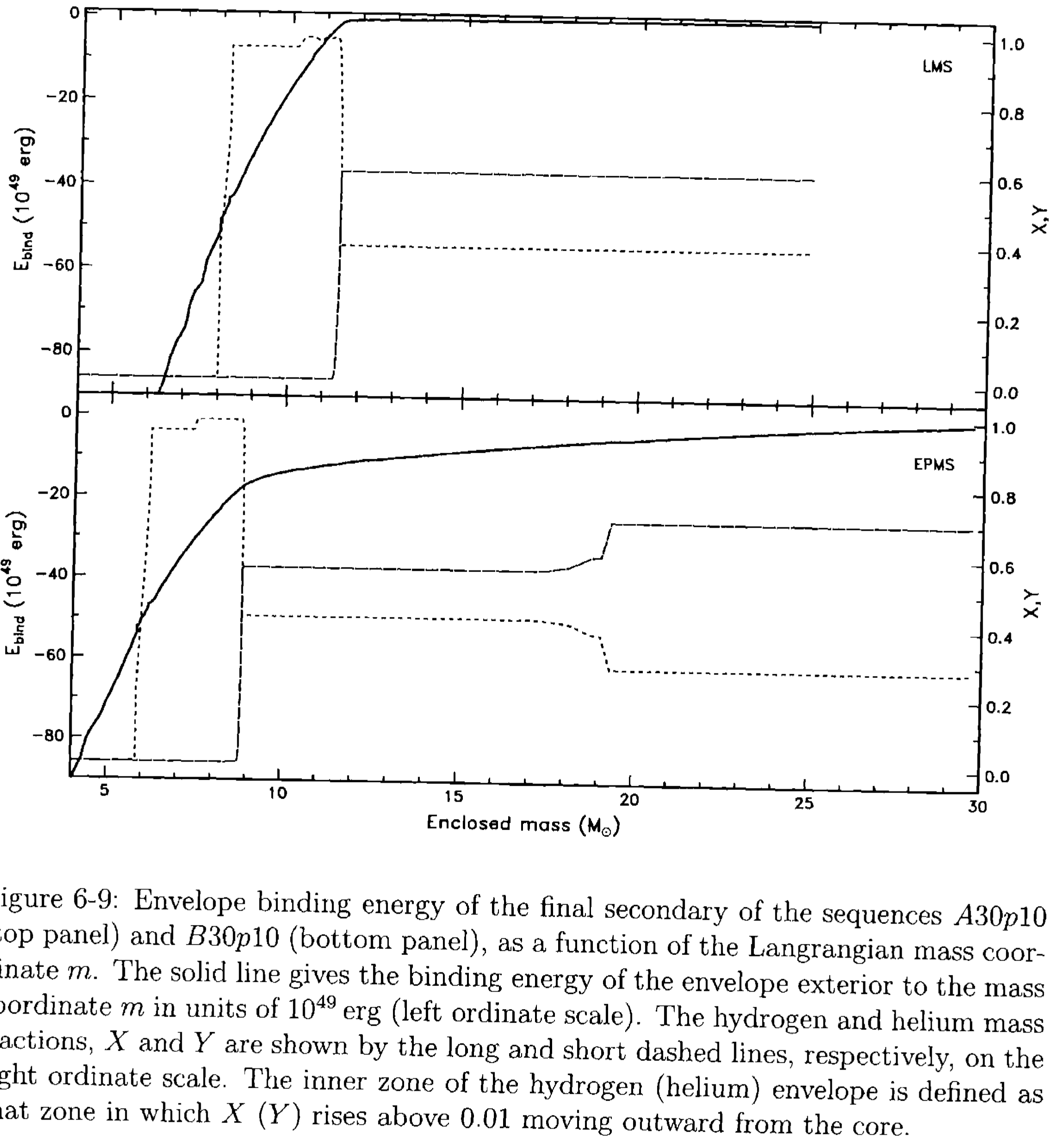

Figure 6-9: Envelope binding energy of the final secondary of the sequences *A*30*p*10 (top panel) and *B*30*p*10 (bottom panel), as a function of the Langrangian mass coordinate m. The solid line gives the binding energy of the envelope exterior to the mass coordinate m in units of 10^{49} erg (left ordinate scale). The hydrogen and helium mass fractions, X and Y are shown by the long and short dashed lines, respectively, on the right ordinate scale. The inner zone of the hydrogen (helium) envelope is defined as that zone in which X (Y) rises above 0.01 moving outward from the core.

ordinate). For instance, a primary of mass $1.5\,M_\odot$ which orbits the secondary at an initial separation $a_i \sim 2000 R_\odot$ (orbital period $P_i \sim 150\,\mathrm{yr}$) will begin to interact with the envelope of the secondary at the end of the latter's evolution, when its radius is $R_2 \sim 1200\,R_\odot$. As a result of the ensuing common envelope phase, the primary will unbind the secondary's hydrogen envelope in the process of spiralling into its final orbit of $a_f \sim 1.9 R_\odot$ (period $P_f \sim 1.1\,\mathrm{days}$). The relatively loosely bound hydrogen envelope of the LMS secondary is unbound from the star by all primaries in the mass range considered.

After its hydrogen envelope is removed in the first common envelope phase, the secondary becomes a helium, or Wolf-Rayet, star. If, in the course of its evolution towards core collapse, the secondary expands again to meet the smaller critical surface imposed on it by the now much closer primary (approximated by the Roche lobe radius, and represented in Fig. 6-10 by the short dashed line), a second common envelope phase may be induced.[10] Whether the mass transfer which ensues becomes unstable depends in part on the reduced mass ratio $q = M_{2,\mathrm{He}}/M_1$. This second common envelope phase can result in either the ejection of the helium rich envelope (in the case illustrated in Fig. 6-10 for primary masses $M_1 >\sim 2.2\,M_\odot$) or the merger of the compact primary with the He core of the secondary for a less massive primary.

As Fig. 6-11 illustrates, the more tightly bound envelopes of secondaries from EPMS evolutionary sequences require larger injections of energy, and hence higher primary masses, for their successful ejection. The primary mass required to eject the hydrogen envelope in this case is a substantial fraction of the core mass, $M_1 \sim 5.7\,M_\odot$ compared to a core mass of $8.8\,M_\odot$, and hence the mass transfer may remain stable in this case, with no common envelope developing. A complete merger of the primary with the core of the secondary is a more likely outcome in this case.

6.3 Discussion

We conclude that the massive secondaries resulting from the various accretion scenarios presented in Chapter 4 constitute a viable class of progenitors of long gamma-ray bursts. They naturally increase and protect their store of rotational angular mo-

---

[10] My thanks to Philipp Podsiadlowski for suggesting the possibility of a second common envelope phase involving the helium rich shell of the secondary's core.

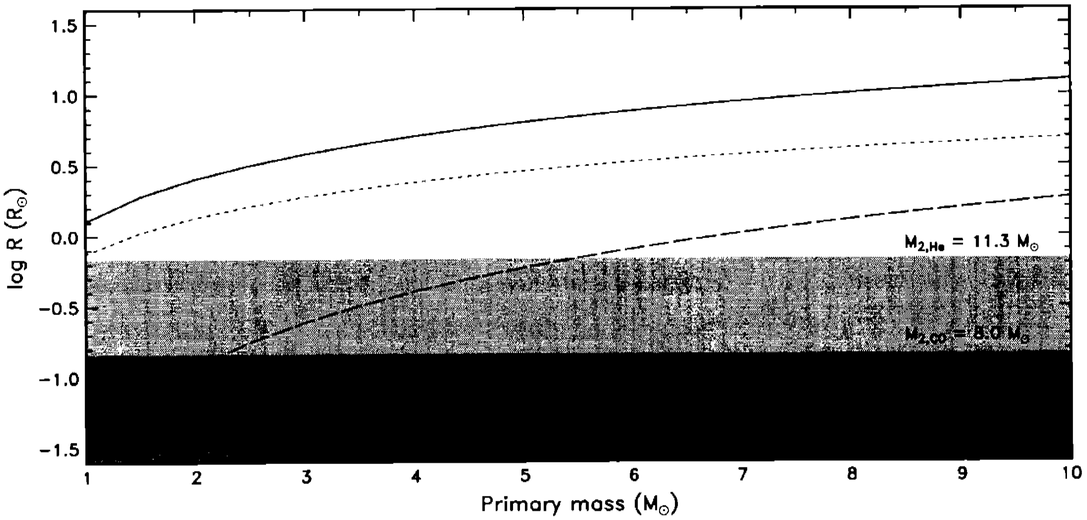

Figure 6-10: Various orbital radii characterizing the end states of two possible common envelope phases between the inspiralling compact primary and the massive secondary near the end of its evolution for sequence $A30p10$, as a function of the primary's mass. The secondary's helium shell and carbon-oxygen core are indicated by the light-grey and dark-grey shaded regions, respectively, while $M_{2,\mathrm{He}}$ and $M_{2,\mathrm{CO}}$ are the corresponding core masses. The secondary is assumed to just fill its critical lobe at the end of its evolution, initiating a common envelope phase and setting the initial orbital radius a_i of the primary (see text). The solid line gives the final orbital radius $a_{f,1}$ of the primary after a common envelope phase in which the secondary's H-rich envelope is lost, while the short dotted line just below it indicates the Roche lobe radius of the secondary's He core immediately following the first common envelope phase. If the secondary's core expands to equal or exceed this radius, another unstable mass transfer event and common envelope phase between the primary and the He core of the secondary is expected to ensue. The long-dashed line is the final orbital radius of the primary after this second common envelope phase drives off the He shell of the secondary. In this case a primary of any mass greater than $1\,M_\odot$ is sufficient to eject the H envelope of the secondary. However, only primaries with $M_1 \gtrsim 2.2\,M_\odot$ will survive a second common envelope phase with the He core of the secondary; less massive primaries will spiral into and merge with the carbon-oxygen core of the secondary.

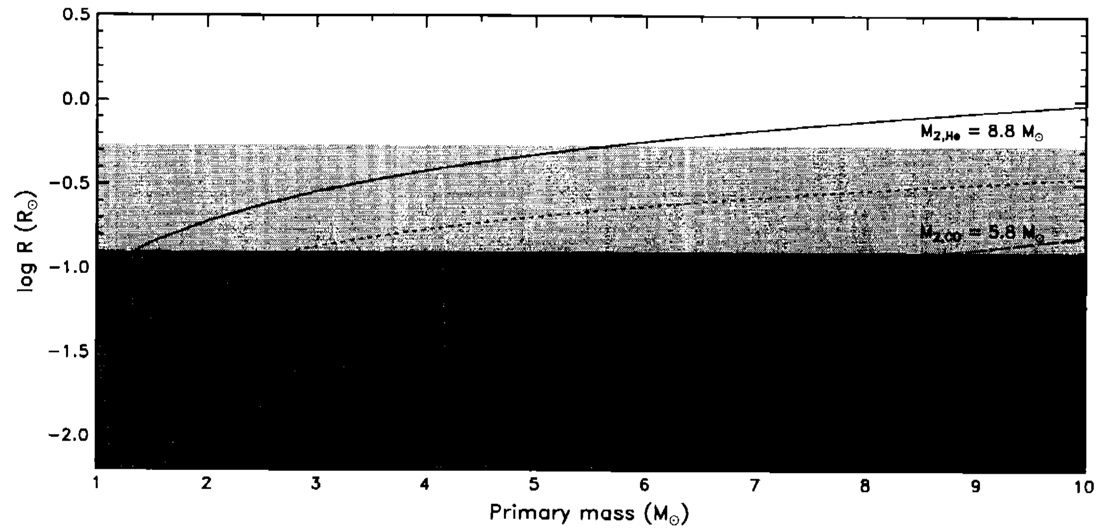

Figure 6-11: Same as Fig. 6-10 for sequence $B31p10$. Primaries with $M_1 >\sim 5.7\,M_\odot$ will survive the initial common envelope phase, while only those with $M_1 >\sim 8.9\,M_\odot$ will avoid a merger with the carbon-oxygen core of the secondary if a second common envelope phase ensues.

mentum by tapping the reservoir of orbital angular momentum associated with the binary star systems of which they are a part. They furthermore remain clothed in a massive layer of hydrogen and helium throughout their lives, and hence are expected to possess massive iron cores at the time of core collapse. A more massive core favors the formation of a correspondingly more massive central black hole, and hence a potentially more efficient generator of the energetic outflow which is thought to drive the production of gamma-ray bursts (Brown et al. 2001).

All stellar models considered in the present study were assumed to begin their lives on the main sequence with essentially no angular momentum, due to tidal locking with their companion in the binary. The orbital frequency of the binary orbit is given by

$$\Omega_o = \sqrt{\frac{G(M_1 + M_2)}{a_o^3}} = 1.4 \times 10^{-7} \left(\frac{M_1 + M_2}{50\,M_\odot} \right)^{1/2} \left(\frac{1000 R_\odot}{a_o} \right)^{3/2} \mathrm{s}^{-1},$$

where a_o is the orbital separation of the components (which are assumed to be in a circular orbit). The ZAMS moment of inertia of the inner 10 $M_\odot$ of sequence $B30p10$ is $I_{core} \approx 10^{56.1}\mathrm{g\,cm}^2$, and assuming an orbit with $\Omega_o \sim 10^{-6.3}\,\mathrm{s}^{-1}$ its angular momentum content is $J_{core,i} \approx 10^{49.8}\mathrm{g\,cm}^2\,\mathrm{s}^{-1}$ in solid body rotation. A fraction of this angular momentum will be lost from the core during the star's main sequence evolution, prior to the accretion of mass. At the onset of core carbon burning this model has total core angular momentum $J_{core,f} \approx 10^{50.4}\mathrm{g\,cm^2\,s^{-1}}$ (again for $M < 10\,M_\odot$), as a result of angular momentum transport into the core from accreted mass during its prior evolution. Hence we expect that the (small) initial angular momentum content of the core will not play a major role in forming a viable core accretion disk in our models.

From the range of models presented in Chapter 4, those that start to accrete matter from their companions prior to leaving the main sequence (LMS cases) possess the most favorable core distributions of angular momentum for the formation of a rapidly rotating, central Kerr black hole and surrounding torus (see § 6.1). We analyzed both the original distributions of specific angular momentum j existing at the end of each accretion sequence as well as two limiting distributions, constant specific angular momentum and constant angular frequency Ω, derived assuming the total angular momentum content of the core is kept constant. We find that the secondary of sequence $A30p10$ with Ω constant, that of sequence $A40p10$ (original j distribution), and that of sequence $B30p10$ with Ω constant, are all likely to form rapidly rotating ($a \sim 1$) black holes in their cores. The core of the merger model (Chapter 5) ends its evolution with a a large amount of angular momentum (see Fig. 6-7) contained entirely in its outer $\sim 50\%$ by mass.[11] If this angular momentum is redistributed prior to core collapse (Fig. 6-8), this model, too, possesses a core favorable for the formation of a central, rapidly rotating black hole.

We additionally find that the material surrounding the collapsed central core in each of these models possesses sufficient specific angular momentum to form a centrifugally supported torus within the core. This is an essential ingredient which allows for the operation of several energy extraction mechanisms involving the central black hole.

The massive envelopes which characterize our accretion secondaries will effectively smother any high luminosity, ultrarelativistic outflow generated by the core. Rotationally enhanced stellar winds do not sufficiently reduce the mass of the envelope to cure this problem. However, we find that the compact remnant of the primary[12]

---

[11] This distribution is due to the strong density gradient at the edge of the carbon-oxygen core, which suppresses the hydrodynamic instabilities which give rise to angular momentum transport.

[12] Or the original primary itself, if the secondary is the first component of the system to explode

of the system provides a reservoir of orbital energy which can be effective in driving off the hydrogen (and perhaps helium) envelope of the expanding secondary, when liberated in the course of a common envelope interaction.

Such an interaction is expected to ensue near the end of the secondary's evolution, as its radius increases and it begins to transfer mass to the much less massive primary. We find that the loosely bound envelopes of the LMS accretion secondaries are the most easily ejected by even the least massive primary ($\sim 1\,M_{\odot}$), although this requires a rather large initial orbit and consequently a case C (relative to the secondary) mass transfer. We rather artificially divide the envelope ejection process into two stages and find that in the case of the LMS secondaries a primary of moderate mass possesses enough orbital energy after its first common envelope inspiral to eject the helium shell from the core of the secondary in the second phase. The bare helium or carbon-oxygen core which results constitutes the most likely progenitor of hypernova explosions (supernovae of Type Ic), which in several cases to date have been observed to accompany long GRBs.

---

in a supernova

Chapter 7

Summary

We have described in this dissertation the development of a new computer code for the calculation of the structure and evolution of rotating, mass losing/gaining massive stars in interacting binary systems. This code implements the effects of rapid differential rotation on the stellar equilibrium structures, and calculates the transport of angular momentum due to convection, dynamical and secular shear instabilities, and internal gravity waves. The implicit, second order numerical method used to solve the coupled nonlinear diffusion equations of momentum transport and element mixing can easily be extended to include a simultaneous solution for burning in a nuclear reaction network with characteristic time scales of the same order as the mixing time scale. For the present calculations, however, we only calculate angular momentum transport, setting all mixing diffusivities to zero. The inclusion of simultaneous element mixing in the calculations would be unlikely to change our results significantly; the dilution of molecular weight gradients by such mixing may, in fact, make the hydrodynamic instabilities considered herein more effective in transporting angular momentum to the stellar core.

We have calculated a variety of evolutionary sequences with this code, the majority of which involve the transfer of mass from one component of the binary system to the other at various stages of evolution of the system. In addition, we have calculated the evolution of a system undergoing a common envelope phase followed by the slow merger of one star with the core of the other.

We have also investigated several hydrodynamic interfacial instabilities which we expect to be active at the core-envelope interface (of nearly discontinuous mean molecular weight) of our post-main sequence accretion secondaries. We find that an additional transport mechanism, Reynolds stresses in propagating internal gravity waves, is necessary in order that the angular momentum accreted at the surfaces of our stars can be successfully transmitted into their cores on an evolutionary (helium core-burning) time scale.

We have particularly focused on the evolution of the angular momentum distributions in the cores of our models, and the implications for the progenitors of GRB events. The components of binary systems in principle have access to a large reserve of angular momentum: that which is stored in the orbit of the stars.

7.1 Single vs. binary stars: core angular momentum

Recent calculations examining the angular momentum evolution of isolated rotating stars have shown that they tend to lose too much angular momentum from their cores to form viable GRB progenitors (Heger & Woosley 2003). Magnetic fields only exacerbate the problem when they are included, extracting even greater amounts of angular momentum from the core of the star. Rapid mass and angular momentum loss by rotationally enhanced stellar winds aid in this process.

As the core of a star contracts and its envelope expands during the course of its evolution (resulting in a spin-up of the core and spin-down of the envelope), the gradient of angular velocity across the core-envelope interface inevitably increases. Angular momentum transport, which is sensitive to the magnitude and direction of the angular velocity gradient, thus acts to transfer angular momentum from the core into the envelope, in the direction of the gradient. Through the operation of such processes, the angular momentum content of the core of an isolated star will slowly bleed away. New or more effective modes of angular momentum transport which are similarly sensitive to angular velocity gradients only exacerbate the problem of core momentum loss in single stars.

The models presented in this work avoid many of these pitfalls.

Since they accrete their reservoir of angular momentum relatively late in their main sequence lifetimes (or even after leaving the main sequence), processes which could drain angular momentum away have much less time to act. The no-slip zone in the angular velocity distribution of the envelope which arises as a consequence of the accretion process also acts to shield the angular momentum of regions interior to it. The large quantity of angular momentum which is stored in the envelopes of our stars is thus well positioned to affect the rotational states of their cores.

As shown in Chapter 4, in binary stars which acquire angular momentum at their surfaces, the inverse of the core-envelope angular velocity distribution described above develops: after angular momentum is accreted and transported to the edge of the core, a gradient in Ω is produced which acts in a sense favorable to angular momentum transfer inward, from the envelope to the core. Angular momentum transport mechanisms which we neglect in the present work (such as magnetic fields) can only aid in this process, due to the predominant direction of the angular velocity gradient (inward) in stars bearing angular momentum acquired at their surfaces.

7.2 Implications for GRB progenitors

Considering only the core angular momentum distribution, we have found several viable gamma-ray burst progenitors among the final models of the sequences we have computed. In three cases, the late main-sequence accretion case with an accretion rate $10^{-4}\,M_{\odot}\,\mathrm{yr}^{-1}$, early post main-sequence accretion case with accretion rate $10^{-3}\,M_{\odot}\,\mathrm{yr}^{-1}$, and the merger case, we find that conditions in the core just prior to carbon ignition are favorable for the formation of a tightly bound, centrifugally supported torus surrounding a rapidly rotating, central black hole. Such a configuration constitutes our best current theoretical guess for a viable hypernova/GRB progenitor.

Our models are more problematic from the perspective of possible burst progenitors, however, when their massive envelopes are taken into considered. We have presented several arguments which show that envelopes this massive may smother the incipient jet before it reaches the surface of the star.

Even if the energetic outflow from the central engine in the core fails to reach the surface of the star, a potentially interesting astronomical event might ensue. The energy of collimated jets which do not escape is instead dissipated in the envelope of the star; it is of magnitude $\sim 10^{51}$ erg, which is in principle sufficient to initiate a "jet-driven" supernova explosion in these objects (Khokhlov et al. 1999).

Nonetheless, significantly enhanced stellar winds or additional interactions during a common-envelope phase might well eject a large fraction of the hydrogen envelopes of our stars, and even in some cases the helium shell underlying it. We find that, due to their relatively loosely bound envelopes, the secondaries which result from sequences in which accretion begins during the late main sequence can lose their hydrogen and perhaps even helium envelopes to a low mass companion (the remnant of the original primary of the system). The resulting bare helium or carbon-oxygen core fits well the latest observations results regarding hypernovae explosions in conjunction with GRBs, which appear to be uniformly of Type Ic (Mazzali et al. 2003).

Conversely, we find that the envelopes of secondaries which begin to accrete after they have left the main sequence are more tightly bound, and thus harder to remove via a common envelope phase. Their less rapidly rotating cores and larger final envelope masses make these stars less likely to be viable GRB progenitors.

Appendix A

Iteration matrix solution method

It is crucial that the numerical procedure used to solve matrix equation illustrated in Fig. 2-1 be very efficient. This sparse matrix can be quite large: for a typical stellar model of 300 grid points and 15 nuclear species, the full matrix is square and of dimension $\sim (300)(16) = 4800$. A typical Newton-Raphson calculation as described in § 2.4 can require 30 or more iterations to converge, each involving a solution of the full matrix equation. For a complete evolutionary calculation consisting of several thousand such time steps, it becomes clear that a straightforward inversion of the full matrix is not a computationally viable approach.

Instead, we take advantage of the special block diagonal structure of the matrix to first reduce it to the intermediate form shown in Fig. A-1 (for the particular case of five grid points). This reduced form is then inverted to obtain the desired solution.

The reduction procedure starts with the topmost 3×6 block, which corresponds to the equations expressing the outer boundary conditions. The leftmost 3×3 segment of this block is reduced to the identity matrix by Gaussian elimination, with the remaining elements of the block (and of the associated RHS vector) denoted by an 'S', stored for the inversion which follows (see below). The three columns of the identity matrix corresponding to the first half of the top block are then used to zero the matrix elements of the 3×3 block immediately below it. The middle 3×3 segment of this 3 block is then reduced to an identity matrix by Gaussian elimination, and the values in the third 3×3 segment retained in memory.

This procedure continues until the final 3×6 block of the matrix (which cor-

$$
\begin{array}{|c|c|c|c|c|c|c|c|c|c|c|c|c|c|c|}
1 & 0 & 0 & S & S & S & & & & & & & & & \\
0 & 1 & 0 & S & S & S & & & & & & & & & \\
0 & 0 & 1 & S & S & S & & & & & & & & & \\
0 & 0 & 0 & 1 & 0 & 0 & S & S & S & & & & & & \\
0 & 0 & 0 & 0 & 1 & 0 & S & S & S & & & & & & \\
0 & 0 & 0 & 0 & 0 & 1 & S & S & S & & & & & & \\
 & & & 0 & 0 & 0 & 1 & 0 & 0 & S & S & S & & & \\
 & & & 0 & 0 & 0 & 0 & 1 & 0 & S & S & S & & & \\
 & & & 0 & 0 & 0 & 0 & 0 & 1 & S & S & S & & & \\
 & & & & & & 0 & 0 & 0 & 1 & 0 & 0 & S & S & S \\
 & & & & & & 0 & 0 & 0 & 0 & 1 & 0 & S & S & S \\
 & & & & & & 0 & 0 & 0 & 0 & 0 & 1 & S & S & S \\
 & & & & & & & & & 0 & 0 & 0 & 1 & 0 & 0 \\
 & & & & & & & & & 0 & 0 & 0 & 0 & 1 & 0 \\
 & & & & & & & & & 0 & 0 & 0 & 0 & 0 & 1
\end{array}
\quad
\begin{array}{|c|}
\delta_1 \\ \delta_2 \\ \delta_3 \\ \delta_4 \\ \delta_5 \\ \delta_6 \\ \delta_7 \\ \delta_8 \\ \delta_9 \\ \delta_{10} \\ \delta_{11} \\ \delta_{12} \\ \delta_{13} \\ \delta_{14} \\ \delta_{15}
\end{array}
\quad
\begin{array}{|c|}
S \\ S \\ S \\ S \\ S \\ S \\ S \\ S \\ S \\ S \\ S \\ S \\ S \\ S \\ S
\end{array}
$$

Figure A-1: The array to be inverted as part of the Newton-Raphson iterative solution of the finite difference equations Eqs. (2.19-2.20). All matrix elements not explicitly shown are 0. Entries marked with an 'S' are elements which are stored by the program during the reduction phase.

responds to the inner boundary conditions) is reduced to the form illustrated in Fig. A-1. Inversion begins with this block, which can immediately be solved for the final three unknowns (δ_{13}, δ_{14}, δ_{15}). These are backsubstituted into the preceding block, which can then be solved explicity for δ_{10}, δ_{11}, δ_{12}. This process is continued until the solution is completely determined.

Bibliography

Abt, H. A., & Levy, S. G. 1976, ApJS, 30, 273

—. 1978, ApJS, 36, 241

Akerlof, C., Balsano, R., Barthelemy, S., Bloch, J., Butterworth, P., Casperson, D., Cline, T., Fletcher, S., Frontera, F., Gisler, G., Heise, J., Hills, J., Kehoe, R., Lee, B., Marshall, S., McKay, T., Miller, R., Piro, L., Priedhorsky, W., Szymanski, J., & Wren, J. 1999, Nature, 398, 400

Alexakis, A., Young, Y., & Rosner, R. 2002, Phys. Rev. E, 65, 026313

Alexander, D. R. 1975, ApJS, 29, 363

Alexander, M. E., Chau, W. Y., & Henriksen, R. N. 1976, ApJ, 204, 879

Aloy, M. A., Müller, E., Ibáñez, J. M., Martí, J. M., & MacFadyen, A. 2000, ApJ, 531, L119

Bardeen, J. M., Press, W. H., & Teukolsky, S. A. 1972, ApJ, 178, 347

Bazán, G., Dearborn, D. S. P., Dossa, D. D., Eggleton, P. P., Taylor, A., Castor, J. I., Murray, S., Cook, K. H., Eltgroth, P. G., Cavallo, R. M., Turcotte, S., Keller, S. C., & Pudliner, B. S. 2003, in 3D Stellar Evolution, ed. S. Turcotte, S. C. Keller, & R. M. Cavallo, ASP Conference Series No. 293 (San Francisco: Astronomical Society of the Pacific), 1

Bethe, H. A., & Brown, G. E. 1998, ApJ, 506, 780

Blandford, R. D., & Znajek, R. L. 1977, MNRAS, 179, 433

Bloom, J. S., Djorgovski, S. G., Kulkarni, S. R., & Frail, D. A. 1998a, ApJ, 507, L25

Bloom, J. S., Frail, D. A., & Kulkarni, S. R. 2003, ApJ, 594, 674

Bloom, J. S., Kulkarni, S. R., Djorgovski, S. G., Eichelberger, A. C., Cote, P., Blakeslee, J. P., Odewahn, S. C., Harrison, F. A., Frail, D. A., Filippenko, A. V., Leonard, D. C., Riess, A. G., Spinrad, H., Stern, D., Bunker, A., Dey, A., Grossan, B., Perlmutter, S., Knop, R. A., Hook, I. M., & Feroci, M. 1999, Nature, 401, 453

Bloom, J. S., Kulkarni, S. R., Harrison, F., Prince, T., Phinney, E. S., & Frail, D. A. 1998b, ApJ, 506, L105

Bloom, J. S., Kulkarni, S. R., Price, P. A., Reichart, D., Galama, T. J., Schmidt, B. P., Frail, D. A., Berger, E., McCarthy, P. J., Chevalier, R. A., Wheeler, J. C., Halpern, J. P., Fox, D. W., Djorgovski, S. G., Harrison, F. A., Sari, R., Axelrod, T. S., Kimble, R. A., Holtzman, J., Hurley, K., Frontera, F., Piro, L., & Costa, E. 2002, ApJ, 572, L45

Bondi, H., & Hoyle, F. 1944, MNRAS, 104, 273

Braun, H., & Langer, N. 1995, A&A, 297, 483

Brown, G. E., Heger, A., Langer, N., Lee, C.-H., Wellstein, S., & Bethe, H. A. 2001, New Astronomy, 6, 457

Brown, G. E., & Lee, C. 2004, New Astronomy, 9, 225

Brown, G. E., Lee, C.-H., & Bethe, H. A. 1999, New Astronomy, 4, 313

Brown, G. E., Lee, C.-H., Wijers, R. A. M. J., Lee, H. K., Israelian, G., & Bethe, H. A. 2000, New Astronomy, 5, 191

Caughlan, G. R., & Fowler, W. A. 1988, Atomic Data and Nuclear Data Tables, 40, 283

Cen, R. 1999, ApJ, 524, L51

Chandrasekhar, S. 1933, MNRAS, 93, 390

—. 1961, Hydrodynamic and Hydromagnetic Stability, International Series of Monographs on Physics (Oxford: Oxford University Press)

Clement, M. J. 1974, ApJ, 194, 709

—. 1978, ApJ, 222, 967

—. 1979, ApJ, 230, 230

—. 1994, ApJ, 420, 797

Collatz, L. 1960, The Numerical Treatment of Differential Equations, 3rd edn. (Berlin: Springer-Verlag)

Cowling, T. G. 1951, ApJ, 114, 272

Cox, A. N., & Stewart, J. N. 1970, ApJS, 19, 261

Cox, J. P., & Giuli, R. T. 1968, Principles of Stellar Structure (New York: Gordon and Breach)

Deupree, R. G. 1990, ApJ, 357, 175

—. 1995, ApJ, 439, 357

—. 1998, ApJ, 499, 340

—. 2001, ApJ, 552, 268

Dewi, J. D. M., & Tauris, T. M. 2000, A&A, 360, 1043

Duquennoy, A., & Mayor, M. 1991, A&A, 248, 485

Eggleton, P. P. 1972, MNRAS, 156, 361

—. 1983, ApJ, 268, 368

Endal, A. S., & Sofia, S. 1976, ApJ, 210, 184

—. 1978, ApJ, 220, 279

Faulkner, J., Roxburgh, I. W., & Strittmatter, P. A. 1968, ApJ, 151, 203

Fishman, G. J., & Meegan, C. A. 1995, ARA&A, 33, 415

Frail, D. A., Kulkarni, S. R., Sari, R., Djorgovski, S. G., Bloom, J. S., Galama, T. J., Reichart, D. E., Berger, E., Harrison, F. A., Price, P. A., Yost, S. A., Diercks, A., Goodrich, R. W., & Chaffee, F. 2001, ApJ, 562, L55

Friend, D. B., & Abbott, D. C. 1986, ApJ, 311, 701

Fritts, D. C., Vadas, S. L., & Andreassen, O. 1998, A&A, 333, 343

Fryer, C. L., & Woosley, S. E. 1998, ApJ, 502, L9

Galama, T. J., Tanvir, N., Vreeswijk, P. M., Wijers, R. A. M. J., Groot, P. J., Rol, E., van Paradijs, J., Kouveliotou, C., Fruchter, A. S., Masetti, N., Pedersen, H., Margon, B., Deutsch, E. W., Metzger, M., Armus, L., Klose, S., & Stecklum, B. 2000, ApJ, 536, 185

Goldreich, P., & Nicholson, P. D. 1989, ApJ, 342, 1079

Gough, D. 1997, Nature, 388, 324

Heger, A., Fryer, C. L., Woosley, S. E., Langer, N., & Hartmann, D. H. 2003, ApJ, 591, 288

Heger, A., Langer, N., & Woosley, S. E. 2000, ApJ, 528, 368

Heger, A., & Woosley, S. E. 2003, in Gamma-Ray Burst and Afterglow Astronomy 2001: A Workshop Celebrating the First Year of the HETE Mission, ed. G. Ricker & R. Vanderspek, AIP Conf. Proc. No. 662 (Melville, N.Y.: American Institute of Physics), 214–216

Hellings, P. 1983, Ap&SS, 96, 37

Henyey, L. G., Wilets, L., Böhm, K. H., Lelevier, R., & Levee, R. D. 1959, ApJ, 129, 628

Hildebrand, F. B. 1956, Introduction to Numerical Analysis (New York: McGraw-Hill)

Howard, L. N. 1961, J. Fluid Mech., 10, 509

Huebner, W. F., Merts, A. L., Magee, N. H., & Argo, M. F. 1977, Los Alamos Sci. Lab. Rept. LA-6760-M

Iben, I. 1986, ApJ, 304, 201

Iben, I. J., & Livio, M. 1993, PASP, 105, 1373

Ivanova, N., Belczynski, K., Kalogera, V., Rasio, F. A., & Taam, R. E. 2003, ApJ, 592, 475

Ivanova, N., Podsiadlowski, P., & Spruit, H. 2002, MNRAS, 334, 819

Jackson, S. 1970a, ApJ, 160, 685

—. 1970b, ApJ, 161, 579

James, R. A. 1964, ApJ, 140, 552

Janka, H.-T., Eberl, T., Ruffert, M., & Fryer, C. L. 1999, ApJ, 527, L39

Joss, P. C., & Becker, J. A. 2003, in From Twilight to Highlight: The Physics of Supernovae, ed. W. Hillebrandt & B. Leibundgut, ESO Astrophysics Symposia (Berlin: Springer-Verlag), 104–112

Kawabata, K. S., Deng, J., Wang, L., Mazzali, P., Nomoto, K., Maeda, K., Tominaga, N., Umeda, H., Iye, M., Kosugi, G., Ohyama, Y., Sasaki, T., Höflich, P., Wheeler, J. C., Jeffery, D. J., Aoki, K., Kashikawa, N., Takata, T., Kawai, N., Sakamoto, T., Urata, Y., Yoshida, A., Tamagawa, T., Torii, K., Aoki, W., Kobayashi, N., Komiyama, Y., Mizumoto, Y., Noumaru, J., Ogasawara, R., Sekiguchi, K., Shirasaki, Y., Totani, T., Watanabe, J., & Yamada, T. 2003, ApJ, 593, L19

Khokhlov, A. M., Höflich, P. A., Oran, E. S., Wheeler, J. C., Wang, L., & Chtchelkanova, A. Y. 1999, ApJ, 524, L107

Kippenhahn, R., & Meyer-Hofmeister, E. 1977, A&A, 54, 539

Kippenhahn, R., & Thomas, H.-C. 1970, in Stellar Rotation, ed. A. Slettebak, IAU Colloq. No. 4 (New York: Gordon and Breach Science Publishers), 20

Kippenhahn, R., & Thomas, H.-C. 1978, A&A, 63, 265

Kippenhahn, R., & Thomas, H.-C. 1981, in Fundamental Problems in the Theory of Stellar Evolution, ed. D. Sugimoto, D. Lamb, & D. Schramm, IAU Symp. No. 93 (Dordrecht: D. Reidel Publishing Co.), 237–254

Kippenhahn, R., & Weigert, A. 1967, Zeitschrift fur Astrophysics, 65, 251

—. 1990, Stellar Structure and Evolution, Astronomy and Astrophysics Library (Berlin: Springer-Verlag)

Kippenhahn, R., Weigert, A., & Hofmeister, E. 1967, in Methods in Computational Physics, ed. B. Alder, S. Fernbach, & M. Rothenberg, Vol. 7 (New York: Academic Press), 129–190

Klebesadel, R. W., Strong, I. B., & Olson, R. A. 1973, ApJ, 182, L85

Kopal, Z. 1959, Close Binary Systems, The International Astrophysics Series (London: Chapman & Hall)

Kouveliotou, C., Meegan, C. A., Fishman, G. J., Bhat, N. P., Briggs, M. S., Koshut, T. M., Paciesas, W. S., & Pendleton, G. N. 1993, ApJ, 413, L101

Krishnamurthi, A., Pinsonneault, M. H., Barnes, S., & Sofia, S. 1997, ApJ, 480, 303

Kulkarni, S. R., Djorgovski, S. G., Odewahn, S. C., Bloom, J. S., Gal, R. R., Koresko, C. D., Harrison, F. A., Lubin, L. M., Armus, L., Sari, R., Illingworth, G. D., Kelson, D. D., Magee, D. K., van Dokkum, P. G., Frail, D. A., Mulchaey, J. S., Malkan, M. A., McClean, I. S., Teplitz, H. I., Koerner, D., Kirkpatrick, D., Kobayashi, N., Yadigaroglu, I.-A., Halpern, J., Piran, T., Goodrich, R. W., Chaffee, F. H., Feroci, M., & Costa, E. 1999a, Nature, 398, 389

Kulkarni, S. R., Frail, D. A., Sari, R., Moriarty-Schieven, G. H., Shepherd, D. S., Udomprasert, P., Readhead, A. C. S., Bloom, J. S., Feroci, M., & Costa, E. 1999b, ApJ, 522, L97

Kumar, P., Talon, S., & Zahn, J. 1999, ApJ, 520, 859

Lamb, D. Q. 1995, PASP, 107, 1152

Lamb, S. A., Iben, I., & Howard, W. M. 1976, ApJ, 207, 209

Langer, N. 1998, A&A, 329, 551

Lattimer, J. M., & Schramm, D. N. 1974, ApJ, 192, L145

Lauterborn, D. 1970, A&A, 7, 150

Lee, H. K., Brown, G. E., & Wijers, R. A. M. J. 2000a, ApJ, 536, 416

Lee, H. K., Wijers, R. A. M. J., & Brown, G. E. 2000b, Phys. Rep., 325, 83

Liang, E. P. 1989, in Proc. of Gamma Ray Observatory Science Workshop, ed. W. N. Johnson, 10–12

Lighthill, M. J. 1962, J. Fluid Mech., 14, 385

Livio, M., Ogilvie, G. I., & Pringle, J. E. 1999, ApJ, 512, 100

Mészáros, P. 2002, ARA&A, 40, 137

Mészáros, P., & Rees, M. J. 2001, ApJ, 556, L37

MacDonald, D., & Thorne, K. S. 1982, MNRAS, 198, 345

MacFadyen, A. I., & Woosley, S. E. 1999, ApJ, 524, 262

Maeder, A. 1997, A&A, 321, 134

Maeder, A., & Meynet, G. 1996, A&A, 313, 140

—. 2000, ARA&A, 38, 143

Mazets, M. P., Golenetskii, S. V., & Ilinskii, V. N. 1974, JETP Lett., 19, 77

Mazzali, P. A., Deng, J., Tominaga, N., Maeda, K., Nomoto, K., Matheson, T., Kawabata, K. S., Stanek, K. Z., & Garnavich, P. M. 2003, ApJ, 599, L95

Meszaros, P., & Rees, M. J. 1997, ApJ, 482, L29

Metzger, M. R., Djorgovski, S. G., Kulkarni, S. R., Steidel, C. C., Adelberger, K. L., Frail, D. A., Costa, E., & Frontera, F. 1997, Nature, 387, 878

Meyer, F., & Meyer-Hofmeister, E. 1979, A&A, 78, 167

Meynet, G., & Maeder, A. 1997, A&A, 321, 465

Miles, J. W. 1957, J. Fluid Mech., 3, 185

—. 1959a, J. Fluid Mech., 6, 568

—. 1959b, J. Fluid Mech., 6, 583

Narayan, R., Paczyński, B., & Piran, T. 1992, ApJ, 395, L83

Nemiroff, R. J. 1994, Comm. Astrophy., 17, 189

—. 1995, PASP, 107, 1131

Nieuwenhuijzen, H., & de Jager, C. 1990, A&A, 231, 134

Nisenson, P., & Papaliolios, C. 1999, ApJ, 518, L29

Nisenson, P., Papaliolios, C., Karovska, M., & Noyes, R. 1987, ApJ, 320, L15

Nomoto, K., Maeda, K., Mazzali, P. A., Umeda, H., Deng, J., & Iwamoto, K. 2003, ArXiv Astrophysics e-prints, astro-ph/0308136

Ostriker, J. P., & Mark, J. W.-K. 1968, ApJ, 151, 1075

Paciesas, W. S., Meegan, C. A., Pendleton, G. N., Briggs, M. S., Kouveliotou, C., Koshut, T. M., Lestrade, J. P., McCollough, M. L., Brainerd, J. J., Hakkila, J., Henze, W., Preece, R. D., Connaughton, V., Kippen, R. M., Mallozzi, R. S., Fishman, G. J., Richardson, G. A., & Sahi, M. 1999, ApJS, 122, 465

Packet, W. 1981, A&A, 102, 17

Paczyński, B. 1976, in Structure and Evolution of Close Binary Systems, ed. P. Eggleton, S. Mitton, & J. Whelan, IAU Symp. No. 73 (Dordrecht: D. Reidel), 75

Paczýnski, B. 1986, ApJ, 308, L43

Paczyński, B. 1991, Acta Astronomica, 41, 257

—. 1995, PASP, 107, 1167

—. 1998, ApJ, 494, L45

Paczyński, B., & Sienkiwicz, R. 1972, Acta. Astr., 22, 73

Papaloizou, J. C. B., & Whelan, J. A. J. 1973, MNRAS, 164, 1

Pfahl, E., Rappaport, S., Podsiadlowski, P., & Spruit, H. 2002, ApJ, 574, 364

Pinsonneault, M. H., Kawaler, S. D., Sofia, S., & Demarque, P. 1989, ApJ, 338, 424

Podsiadlowski, P. 1989, PhD thesis, Massachusetts Institute of Technology

Podsiadlowski, P. 1992, PASP, 104, 717

Podsiadlowski, P., Joss, P. C., & Hsu, J. J. L. 1992, ApJ, 391, 246

Podsiadlowski, P., Mazzali, P. A., Nomoto, K., Lazzati, D., & Cappellaro, E. 2004, ApJ, 607, L17

Podsiadlowski, P., Rappaport, S., & Han, Z. 2003, MNRAS, 341, 385

Popham, R., Woosley, S. E., & Fryer, C. 1999, ApJ, 518, 356

Press, W. H., Teukolsky, S., Vetterling, W., & Flannery, B. 1992, Numerical Recipes in Fortran, 2nd edn. (Cambridge: Cambridge University Press)

Price, P. A., Kulkarni, S. R., Berger, E., Fox, D. W., Bloom, J. S., Djorgovski, S. G., Frail, D. A., Galama, T. J., Harrison, F. A., McCarthy, P., Reichart, D. E., Sari, R., Yost, S. A., Jerjen, H., Flint, K., Phillips, A., Warren, B. E., Axelrod, T. S., Chevalier, R. A., Holtzman, J., Kimble, R. A., Schmidt, B. P., Wheeler, J. C., Frontera, F., Costa, E., Piro, L., Hurley, K., Cline, T., Guidorzi, C., Montanari, E., Mazets, E., Golenetskii, S., Mitrofanov, I., Anfimov, D., Kozyrev, A., Litvak, M., Sanin, A., Boynton, W., Fellows, C., Harshman, K., Shinohara, C., Gal-Yam, A., Ofek, E., & Lipkin, Y. 2003, ApJ, 589, 838

Randers, G. 1942, ApJ, 95, 454

Rappaport, S., Joss, P. C., & Webbink, R. F. 1982, ApJ, 254, 616

Rasio, F. A., & Livio, M. 1996, ApJ, 471, 366

Rees, M. J. 1987, Nature, 328, 207

Rees, M. J., & Meszaros, P. 1992, MNRAS, 258, 41P

Reichart, D. E. 1999, ApJ, 521, L111

Rhoads, J. E. 1997, ApJ, 487, L1

Ringot, O. 1998, A&A, 335, L89

Roberts, I. P. H. 1963, ApJ, 137, 1129

Rosner, R., Pinsonneault, M. H., Barnes, S., & Sofia, S. 1997, ApJ, 480, 303

Roxburgh, I. W., Griffith, J. S., & Sweet, P. A. 1965, Z. Astr., 61, 203

Ruderman, M. 1975, New York Academy Sciences Annals, 262, 164

Sackmann, I.-J., & Anand, S. P. S. 1970, ApJ, 162, 105

Schwarzschild, M. 1958, Structure and Evolution of the Stars (Princeton: Princeton University Press)

Smith, G. D. 1985, Numerical Solution of Partial Differential Equations: Finite Difference Methods, 3rd edn. (Oxford: Oxford University Press)

Spitzer, L. 1965, Physics of Fully Ionized Gases, 2nd edn., Interscience Tracts on Physics and Astronomy (New York: Interscience Publication)

Stanek, K. Z., Matheson, T., Garnavich, P. M., Martini, P., Berlind, P., Caldwell, N., Challis, P., Brown, W. R., Schild, R., Krisciunas, K., Calkins, M. L., Lee, J. C., Hathi, N., Jansen, R. A., Windhorst, R., Echevarria, L., Eisenstein, D. J., Pindor, B., Olszewski, E. W., Harding, P., Holland, S. T., & Bersier, D. 2003, ApJ, 591, L17

Stein, R. F. 1966, in Stellar Evolution, ed. R. F. Stein & A. G. W. Cameron (New York: Plenum Press)

Taam, R. E., Bodenheimer, P., & Ostriker, J. P. 1978, ApJ, 222, 269

Taam, R. E., & Sandquist, E. L. 2000, ARA&A, 38, 113

Tassoul, J. 1978, Theory of Rotating Stars, Princeton Series in Astrophysics (Princeton: Princeton University Press)

—. 2000, Stellar Rotation, Cambridge Astrophysics Series (New York: Cambridge University Press)

Thompson, C. 1994, MNRAS, 270, 480

Usov, V. V. 1994, MNRAS, 267, 1035

van den Heuvel, E. P. J. 2001, in The Neutron Star - Black Hole Connection, ed. C. Kouveliotou, J. Ventura, & E. van den Heuvel, NATO Science Series: Mathematical and Physical Sciences No. 567 (Dordrecht: Kluwer Academic Publishers), 173

van Putten, M. H. P. M. 2001, Phys. Rep., 345, 1

van Putten, M. H. P. M., & Levinson, A. 2003, ApJ, 584, 937

van Putten, M. H. P. M., & Ostriker, E. C. 2001, ApJ, 552, L31

Wang, L., Howell, D. A., Höflich, P., & Wheeler, J. C. 2001, ApJ, 550, 1030

Wang, L., & Wheeler, J. C. 1998, ApJ, 504, L87

Waxman, E., & Mészáros, P. 2003, ApJ, 584, 390

Weiss, A., Hillebrandt, W., & Truran, J. W. 1988, A&A, 197, L11

Wheeler, J. C., Yi, I., Höflich, P., & Wang, L. 2000, ApJ, 537, 810

Woosley, S. E. 1993, ApJ, 405, 273

Woosley, S. E., Heger, A., & Weaver, T. A. 2002, Reviews of Modern Physics, 74, 1015

Zahn, J.-P. 1974, in Stellar Instability and Evolution, ed. P. Ledoux, A. Noels, & A. Rodgers, IAU Symp. No. 59, 185-194

Zahn, J.-P. 1975, A&A, 41, 329

—. 1977, A&A, 57, 383

—. 1992, A&A, 265, 115

Zahn, J.-P., Talon, S., & Matias, J. 1997, A&A, 322, 320

Zhang, W., & Fryer, C. L. 2001, ApJ, 550, 357

Zhang, W., Woosley, S. E., & MacFadyen, A. I. 2003, ApJ, 586, 356